UNI... OF MICHIGAN
NOV 1 1 195...
ENGINEERING LIBRARY

JOURNAL OF THE AERONAUTICAL SCIENCES

VOLUME 19 NOVEMBER, 1952 NUMBER 11

CONTENTS

A Free-Flight Investigation of the Possibility of High Reynolds Number Supersonic Laminar Boundary Layers ..... JOSEPH STERNBERG 721

On the Flow Behind an Attached Curved Shock ..... S. I. PAI 734

An Impulse-Momentum Method for Calculating Landing-Gear Impact Conditions in Unsymmetrical Landings ..... ROBERT T. YNTEMA 743

The Subsonic Calculation of Circulatory Spanwise Loadings for Oscillating Airfoils by Lifting-Line Techniques ..... M. A. DENGLER AND MARTIN GOLAND 751

On the Temperature Distribution Along a Semi-Infinite Sweat-Cooled Plate ..... NATHAN NESS 760

The Aerodynamic Forces on Low Aspect Ratio Wings Oscillating in an Incompressible Flow ..... H. R. LAWRENCE AND E. H. GERBER 769

Readers' Forum: "The Study of Compressible Flow Through Cascades Using a Linear Pressure-Volume Relationship," by David C. Prince, Jr.; "A New Mechanical Analogy for the Flow of Compressible Fluid," by Nobuo Inoue; "Reciprocity Relations in Wing-Body Systems," by W. M. Bleakney and G. K. Morikawa; "On the Kirchhoff Solution for an Oscillating Wing in Subsonic Compressible Flow," by John W. Miles; "Experiments with Large Pitot Tubes in a Narrow Supersonic Wake," by N. H. Johannesen and W. A. Mair; "Computing Critical Loads by Splitting the Rigidity of Composite Systems," by F. Buckens; "On Heat Transfer, Recovery Factors, and Spin for Laminar Flows," by Arthur N. Tifford and Sheng To Chu; "Remarks on 'On the Flight Dynamics of Slender Special-Purpose Aircraft,'" by F. Niedenfuhr, with "Authors' Reply" by R. M. Rosenberg and George Stoner; "Reply to Fettis' Comments on 'Aerodynamic Coefficients of an Oscillating Airfoil in Two-Dimensional Subsonic Flow,'" by R. Timman, A. I. van de Vooren, and J. H. Greidanus; "Gas-Turbine Power Plant for Aircraft," by Ali Bülent, Çambel 782–792

Published by the

INSTITUTE OF THE AERONAUTICAL SCIENCES, INC.

JOURNAL OF THE AERONAUTICAL SCIENCES

Editor: HUGH L. DRYDEN, *Director, N.A.C.A.*

Associate Editor: ROBERT R. DEXTER *Managing Editor:* BERNEICE H. JARCK

Editorial Committee

Aerodynamics

Francis Clauser
Howard Emmons
Alexander Flax
R. Paul Harrington
R. T Jones
Carl Kaplan
H W. Liepmann
C. C. Lin
H. F. Ludloff
Harold Luskin
John R. Markham
Clark B. Millikan
Shatswell Ober
W Bailey Oswald
Allen E. Puckett
Elliott G. Reid
H. J. E. Reid
Russell Robinson
G. B. Schubauer
W R. Sears
John Stack
Theodore von Kármán
Richard von Mises

Air Transport

Charles Froesch
J. A. Herlihy
R. D. Kelly
Otto E. Kirchner
Jerome Lederer
John C. Leslie
R. Dixon Speas

Flight Testing

W. K. Ebel
R. R. Gilruth
Melvin N. Gough
E. G. Stout

Structures and Materials

W. B. Bleakney
E. W. Conlon
L. H. Donnell
E. C. Hartmann
N. J. Hoff
Samuel Levy
E. E. Lundquist
Alfred S. Niles
W. Ramberg
E. Reissner
F. R. Shanley
H. W. Sibert
C. R. Strang
S. Timoshenko
H. S. Tsien
Chi-Teh Wang

Rotating Wing Aircraft

F. B. Gustafson
K. H. Hohenemser
Bartram Kelley
R. B. Maloy
Ralph McClarren
R. H. Miller
R. H. Prewitt
Igor I. Sikorsky

Vibration and Flutter

Lee Arnold
M. A. Biot
R. L. Bisplinghoff
William Bollay
Chieh-Chien Chang
I. E. Garrick
Martin Goland
J. P. Den Hartog

Aircraft Design

W. E. Beall
W. K. Ebel
Hall L. Hibbard
Richard Hutton
C. L. Johnson
A. A. Kartveli
C. J. McCarthy
Fred E. Weick
Robert J. Woods

Electronics in Aviation

K. C. Black
E. F. Herzog
David S. Little
D. K. Martin
George Rappaport
Paul Rosenberg
L. M. Sherer

Physiologic Problems

H. G. Armstrong
Louis H. Bauer
Robert J. Benford
Eugene Du Bois
W. Randolph Lovelace, II
Ross A. MacFarland

Fuels and Oils

D. P. Barnard
J. H. Doolittle
Graham Edgar
R. T. Goodwin
S. D. Heron
A. M. Rothrock

Flight Propulsion

George W. Brady
Frank W. Caldwell
L. S. Hobbs
E. E Johnson
Joseph Keenan
R. P. Kroon
Hans Reissner
Abe Silverstein
C. Fayette Taylor
E. S. Taylor
P. Taylor
E S. Thompson
H. S. Tsien

Instruments

Allan G. Binnie
J. R Bradburn
Charles H. Colvin
C. S. Draper
S. G. Eskin
O. E. Esval
H. W. Holzapfel
W. L. Howland
George H. Purcell
C. F. Savage
O. Hugo Schuck
C. L. Seward, Jr.
L. D. Statham
R. C. Sylvander
D. K. Warner

Meteorology

C. F. Brooks
D. M. Little
E. J. Minser
F. W. Reichelderfer
H. C. Willett

SUBSCRIPTION RATES

JOURNAL OF THE AERONAUTICAL SCIENCES, Published Monthly.—United States and Possessions: 1 Year, $12.00; Single Copies, $1.50. Foreign Countries Including Canada (American Currency Rates): 1 Year, $13.00; Single Copies, $1.50.

AERONAUTICAL ENGINEERING REVIEW, Published Monthly.—United States and Possessions: 1 Year, $3.00; Single Copies, $0.50. Foreign Countries Including Canada (American Currency Rates): 1 Year, $3.50; Single Copies, $0.50.

Notices of change of address should be sent to the Institute at least 30 days prior to actual change of address.

Manuscripts for publication, proofs, and all correspondence should be addressed to the Editorial Office of the JOURNAL.

Correspondence regarding subscriptions may be addressed to Publication Office, 20th and Northampton Sts., Easton, Pa., or to the Editorial Office of the JOURNAL OF THE AERONAUTICAL SCIENCES, 2 East 64th Street, New York 21, New York.

Copyright, 1952, by the Institute of the Aeronautical Sciences, Inc.

Entered as Second Class Matter at the Post Office, Easton, Pa., May 1, 1937. Acceptance for mailing at a special rate of Postage provided for in the Act of August 24, 1912. Authorized April 29, 1937.

JOURNAL OF THE AERONAUTICAL SCIENCES

VOLUME 19 NOVEMBER, 1952 NUMBER 11

A Free-Flight Investigation of the Possibility of High Reynolds Number Supersonic Laminar Boundary Layers*

JOSEPH STERNBERG†

Ballistic Research Laboratories, Aberdeen Proving Ground

SUMMARY

A modified V-2 was fired October 26, 1950, at White Sands Proving Ground to determine whether, under favorable conditions, laminar flow at high Reynolds Numbers at supersonic speeds was possible. The test area was the surface of a special polished 20° included angle conical nose more than 8 ft. long, which replaced the standard V-2 warhead. The rocket reached $M = 3$ at 25,000 ft. in approximately horizontal flight before it exploded from unknown causes. With the large thermal inertia of the 0.18-in. thick skin, the skin temperature lagged well behind the boundary-layer recovery temperature. Consequently, during most of the supersonic portion of the flight, the heat transfer from the air to the surface was greater than that required to damp small boundary-layer oscillations according to Lees' theory. Measurements of the nose skin temperature and of total pressures in the boundary layer were telemetered in order to establish the laminar or turbulent state of the boundary layer. The pressure and temperature data indicate that the cone boundary layer was laminar at an equivalent flat plate Reynolds Number of 5×10^7, which was the largest Reynolds Number obtained on the cone.

Presented at the Aerodynamics Session, Twentieth Annual Meeting, I.A.S., New York, January 28–February 1, 1952.

* The author wishes to acknowledge the assistance of a number of people on various phases of this experiment. The study to determine the feasibility of a low trajectory for the V-2 was made jointly with Dr. A. S. Galbraith, of the Ballistic Research Laboratories. F. C. Fay and W. R. Norman, of the General Electric Company, performed the trajectory calculations required to establish the program cam data. The telemetering system and trajectory data were provided by the White Sands Annex of the Ballistic Research Laboratories. Dr. T. L. Smith, of the Ballistic Research Laboratories, proposed the use of resistance elements for measuring the skin temperatures and supervised the installation of the temperature and pressure instrumentation. Miss M. J. Cox carried out many of the numerical calculations required. The author also wishes to acknowledge the cooperation of the General Electric personnel at White Sands under the direction of L. D. White and the White Sands Proving Ground Technical Division under the direction of H. L. Karsch.

† Chief, Supersonic Wind Tunnels Branch.

NOTATION

μ	= viscosity
λ	= heat conduction coefficient
C_P	= air specific heat at constant pressure
Pr	= Prandtl Number = $C_P\mu/\lambda$
T	= temperature, °C.
ρ	= air density
x	= distance from leading edge or nose of body
y	= normal distance from cone surface
U	= velocity, ft. per sec.
P_T	= total pressure, lbs. per sq. in.
P_{TS}	= total pressure just outside of the boundary layer
M	= Mach Number of rocket
M_s	= Mach Number just outside boundary layer
δ	= boundary-layer thickness
θ	= boundary-layer momentum thickness
R_θ, R_x	= Reynolds Number based on lengths θ, x
$R_{cr.\ min.}$	= stability limit
T_0	= stagnation temperature for flow, M_s
$T_{ins.}$	= wall temperature for insulated surface
r	= recovery factor = $(T_{ins.} - T_s)/(T_0 - T_s)$
q	= heat-transfer rate = cal./cm.² sec.
h	= heat-transfer coefficient = $q/(T_{ins.} - T_w)$ = cal./cm.² sec. °K.
τ	= local shearing stress
C_f	= local friction coefficient = $\tau/(1/2)\rho_s U_s^2$
Subscripts	
w	= wall conditions
s	= conditions just outside boundary layer

INTRODUCTION

IN HIS PAPER, LEES[1] PREDICTS that, under certain conditions, very large extents of laminar boundary-layer flow may be attainable at supersonic speeds. According to his calculations, the stabilizing effect of heat transfer from the boundary layer to the surface should be great enough to damp small oscillation in the boundary layer for flow over a flat plate with zero

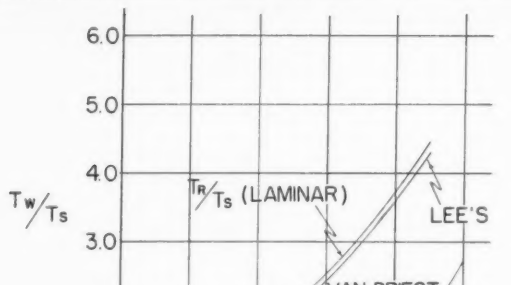

FIG. 1. Critical wall temperature ratios.

longitudinal pressure gradient and constant surface temperature. In the light of subsonic work, it would be expected that pressure gradients would also have important effects on boundary-layer stability at supersonic speeds. However, the analyses of Weil[2] and Lees[3] indicate that pressure gradients only have a significant influence at low supersonic speeds. Above $M = 3$, a favorable pressure gradient seems to have little effect, and heat stabilization should be the more important.

The required wall to free-stream temperature ratios for damping small disturbances are shown in Fig. 1. Lees applied his stability criterion to velocity and temperature profiles obtained by assuming μ proportional to T and $Pr = 1$. More recently, Van Driest has applied the Lees stability criterion to boundary-layer profiles, which should be more accurate for air (viscosity varying with temperature according to Sutherland's law and $Pr = 0.75$). Also included in Fig. 1 is a stability limit curve obtained by J. V. Lewis and the author using boundary-layer profiles for which $Pr = 1$ and μ is proportional to $T^{0.76}$. Assuming that Van Driest's curve is more nearly correct,* it is clear that a large amount of cooling is required to keep below the stability limit curve, though presumably any amount of cooling will have some stabilizing effect. The $R_{\theta_{cr.\ min.}}$ at which amplification of boundary-layer oscillations can begin will be increased and the amplification rate will be decreased for $R_\theta > R_{\theta_{cr.\ min.}}$, since, according to the theory, the amplification rate is proportional to $\sqrt{1/R_{\theta_{cr.\ min.}}}$. However, it appears that the variation of $R_{\theta_{cr.\ min.}}$ with decreasing wall temperature is fairly gradual and that $R_{\theta_{cr.\ min.}}$ rises rapidly as the wall temperature approaches the stability limit. Fig. 2 shows a typical curve obtained by J. V. Lewis and the author (also see reference 4). Therefore, it may be necessary to cool fairly close to the stability limit curve in order to obtain spectacular results.

An experimental check of Lees' theory would require measurements of boundary-layer oscillations similar to the work of Schubauer and Skramstad. Presumably, instrumentation developments now under way will make possible such measurements in supersonic boundary layers. However, as an alternative, it is of interest to investigate the effects of heat stabilization on the location of the boundary-layer transition. If large boundary-layer disturbances can be eliminated when the heat transfer is large enough, the theory predicts the continuance of laminar flow.

Surface roughness or surface discontinuities may constitute large disturbances. Also, it is well known that the fluctuations in a turbulent boundary layer are large disturbances and result in the phenomenon known as transverse contamination and that the "contamination" can upset laminar boundary layers at very low Reynolds Numbers. Some information is available on the effect of shock waves on laminar boundary layers.[5] Even weak shock waves produce large changes in the boundary-layer profiles, apparently always causing boundary-layer separation at the wall if not immediate transition. It is unlikely then that laminar flow on the body of a missile could be expected to persist downstream of a wing or control surface. Even if the wing shock proved inadequate, the turbulent wing wake, if contiguous with the body boundary layer,

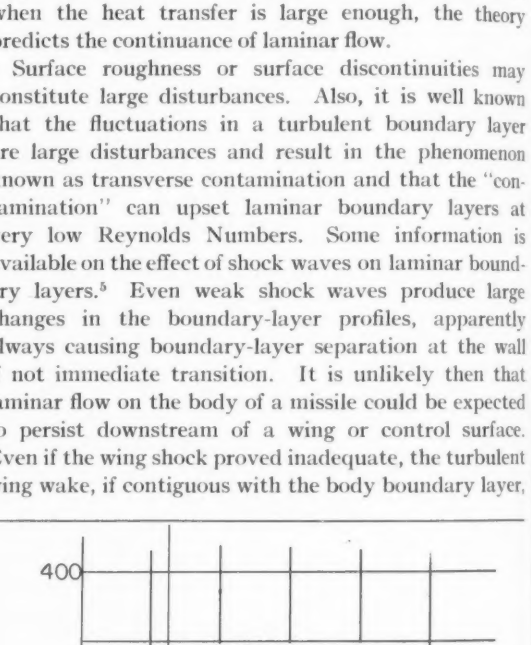

FIG. 2. Variation of $R_{\theta_{cr.\ min.}}$ with wall temperature ratio

* In the Readers' Forum, JOURNAL OF THE AERONAUTICAL SCIENCES, February, 1952, C. C. Lin points out certain restrictions in the stability theory which may invalidate these computations at high Mach Numbers.

should serve as a source of contamination. The production of lift on bodies or wings may have a large if not dominating effect on the state of the boundary layer. For instance, on a body of revolution at incidence, transition on the windward side is delayed and on the leeward side is promoted. Wind-tunnel tests at the Ballistic Research Laboratories on a 20° included angle cone at $M = 3.2$ show strong effects even at small incidence. At zero angle of attack, transition occurred at R_x of about 3×10^6 at about the same axial position for the top and bottom elements of the cone. At 3° angle of attack, transition on the top element occurred at $R_x = 1 \times 10^6$, while on the bottom element it did not occur on the cone and so was at least greater than $R_x = 3 \times 10^6$. The photographic evidence available suggests that the boundary layer on the bottom surface is thinned while the boundary layer on the top is thickened, probably due to the cross flow of low momentum boundary-layer air under the action of the transverse pressure gradient. If the laminar boundary-layer profile is also significantly altered when the body is at an angle of attack, early transition may occur even when the heat transfer is favorable.

Wind-tunnel experiments designed to investigate the effect of heat transfer on boundary-layer transition have been reported by various investigators.[6–8] However, all of these experiments were limited in that the maximum R_x was about 5×10^6. Free-flight Reynolds Numbers that are likely to be of interest may be 10 to 100 times greater. Also, in some of these experiments,[7] disturbances of uncertain magnitude were introduced in order to have transition occur at a convenient place on the model. In the case of Eber's experiment,[6] the disturbance of the corner of the cone cylinder on the boundary layer is probably significant. Wind-tunnel experiments have other uncertainties that may or may not be important. Little is known about the nature or effect of the air turbulence in the test section. Also, it is necessary to test in a region free of shock waves originating at surface imperfections of the nozzle or test section.

Free-flight experiments where the heat transfer and other factors favor the maintenance of laminar boundary layers at high R_x appear to be limited in number. In an experiment designed to obtain heat-transfer data, using a modified V-2 rocket, reported by Norris and Fischer,[9] the wall temperatures on a 45° polished cone were below the recovery temperature; however, they did not approach the stability limit until the R_x had decreased to about 3×10^6.

Present Experiment

(a) Test Surface

In this paper, a free-flight experiment is described in which a V-2 rocket was used to determine whether, under favorable conditions, laminar flow was possible up to high R_x. The test area was the surface of a 20° included angle conical nose more than 8 ft. long, which replaced the standard V-2 warhead. A conical nose was chosen because it is believed that the transition results on a cone can be related to the theoretical calculations on a flat plate. Hantzsche and Wendt[10] have shown that the axial velocity and temperature distribution for the laminary boundary layer on a cone and flat plate should be similar but that the velocity normal to the surface in the boundary layer would be different. However, the normal velocity is neglected in the stability analysis, so that, assuming that disturbances equivalent to the two-dimensional disturbances for the flat plate exist, the flat plate stability results may be applicable.

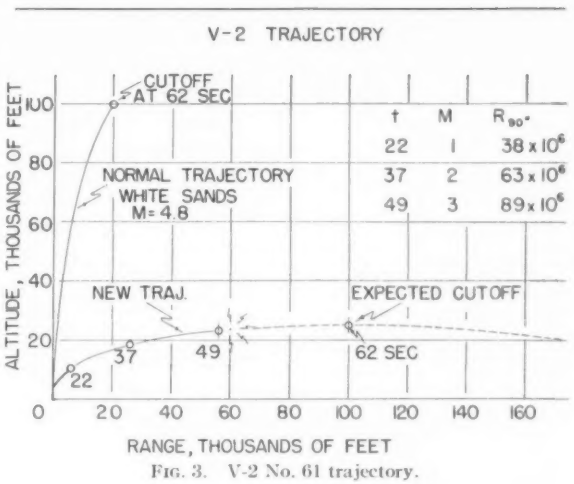

FIG. 3. V-2 No. 61 trajectory.

(b) Trajectory

In the normal trajectory used at White Sands for V-2 firings, the rocket is launched vertically and gradually turns toward the horizontal, so that at the end of the propulsion stage it is traveling at about $M = 5$ at 100,000 ft. Because of the rapid decrease of air density with altitude, the Reynolds Number for an 8-ft. length would reach a maximum of 4×10^7 at $M = 1.4$ and then decrease to 2.6×10^6 at $M = 5$. On the final leg of the trajectory large Reynolds Numbers are attained, but the flight conditions are changing rapidly as the rocket falls to the ground so that the interpretation of measurements would be relatively difficult. Also, as previously mentioned, it is desirable to keep the angle of attack of the nose small, preferably less than 1°. Oscillations of the rocket necessarily occur when it re-enters the atmosphere, and the oscillations might still be unacceptably large in the lower atmosphere where the measurements would be of interest.

For these reasons, the program control was altered to produce the trajectory shown in Fig. 3. For safety reasons, the turn toward horizontal could only be started after 4 sec. Also the rocket was limited, for

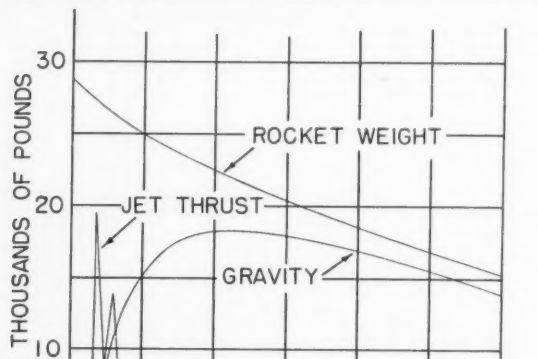

FIG. 4. Force normal to trajectory.

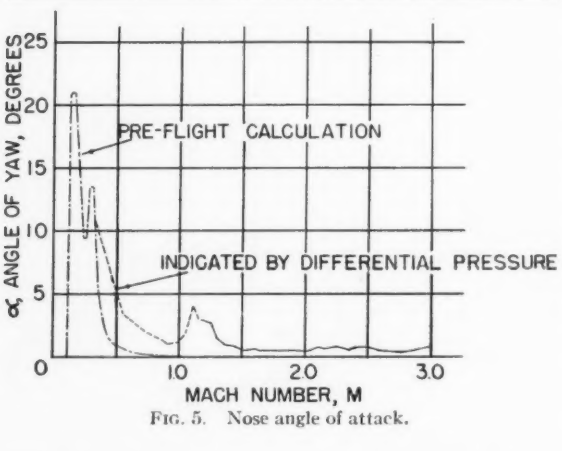

FIG. 5. Nose angle of attack.

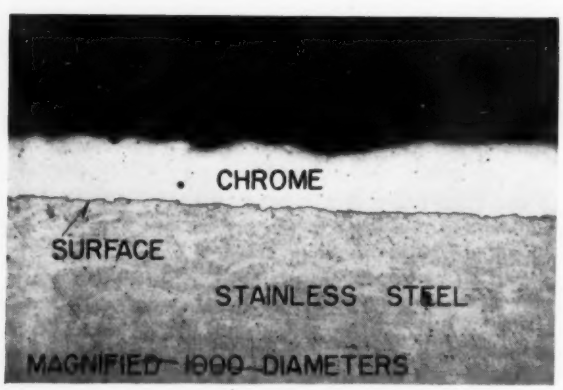

FIG. 6. Photomicrograph showing cross section of surface.

structural reasons, to 1*g* normal acceleration, so that the aerodynamic normal force was not a significant factor in turning the rocket. Rather, Fig. 4 shows that jet thrust in the early flight stages and gravity over most of the trajectory were the important factors in turning the rocket. $M = 1$ was to be reached at a 22-sec. flight time with the rocket about 30° from the horizontal, and the rest of the turn to horizontal flight was to be produced by gravity with the angle of attack programmed to be zero. After burnout, the rocket was expected to follow a ballistic trajectory for an additional 30 sec. with roll control continued to impact. As will be indicated later, after the jet cutoff, the rapid deceleration of the rocket with the correspondingly rapid decrease in the boundary-layer recovery temperature would have caused the heat-transfer conditions to become unfavorable for the maintenance of laminar flow so that the location of the boundary layer transition for a sizable range of heat-transfer conditions would have been obtained. Unfortunately, the rocket exploded after approximately 50 sec. of flight; therefore, data were obtained only during the propulsion stage.

The rocket position and velocity throughout flight were measured with the Ballistic Research Laboratories' Dovap system. These measurements showed that the predicted course was being followed up to the time of the explosion. Four static pressure holes were placed 90° apart around the cone circumference. Differential pressures in the pitch and yaw plane were then measured, and for $M > 1.2$ the cone angle of attack was computed using Kopal's values for cones at small yaw. Fig. 5 shows that for the last 20 sec. of the flight, where $M_s > 1.25$, the cone angle of attack was less than 1°, which should be small enough not to affect the boundary-layer transition. There was no indication from the rocket motion or the telemetered data that anything was amiss, and it has not been possible to establish the cause of the explosion.

(c) Nose Details

The first 12 in. of the nose was solid. The rest of the cone was made in four segments that were formed with a forming brake to the desired shape, then held in a rig, welded together, and finally welded to the solid nose. The cone received a final polish with emory paper and a fine-steel-wool polishing along the cone elements. Photomicrographs were taken of small specimens prepared this way to show the depth and distribution of the polishing scratches. The specimens were electroplated with a hard chromium plate to preserve the condition of the edge and then were cut perpendicular to the polishing direction. Fig. 6, which is a typical photomicrograph (magnification 1,000 diameters), shows that the amplitude of the short wave-length surface irregularities is about 60 microin. (see Fig. 6). Except at the welds, where bead was left on the inside, the skin was fairly uniform in thickness with a tolerance

of ±5 per cent. Fig. 7 shows the important dimensions of the conical nose, which was made for us by The Glenn L. Martin Company.

In order to keep the c.g. of the V-2 rocket within acceptable limits, it was necessary to put lead ballast in the nose. Also, instruments, circuitry, and auxiliary apparatus required for the pressure and temperature measurements that were made at various positions on the nose had to be located within the nose volume. Accordingly, an internal structure was fabricated which was tied to the base ring supporting the conical nose (see Fig. 8). The top of the structure shown contained the lead ballast and the bottom held batteries and other instrumentation. In order to have access to this internal structure, it was necessary to cut a door in the conical nose (Fig. 9). It was felt that, even if the door were carefully fitted to minimize the surface break, there would always be an uncertainty about the importance of the disturbance there. No attempt was made to minimize the surface discontinuity, which was about one hundredth of an inch, and a few hundredths gap was left between the door and the rest of the nose to facilitate door removal. It was expected that, whatever happened near the nose, the boundary layer would be turbulent on the door.

However, there were two ways the door could affect the boundary layer elsewhere on the cone. Any shock wave generated at the door would propagate around the cone surface and, depending on the Mach Number, could affect more or less of the cone surface boundary layer. (The curve representing the propagation of a disturbance that maintains a fixed angle with respect to the cone element at any point is a logarithmic spiral on the developed cone.) As will be described later, a number of measurements were made near the base of the cone directly opposite the door. Assuming that a significant disturbance might originate at the front corner of the door, we would have some interference with the boundary layer for $M_s < 1.7$. For boundary-

FIG. 8. Internal structure.

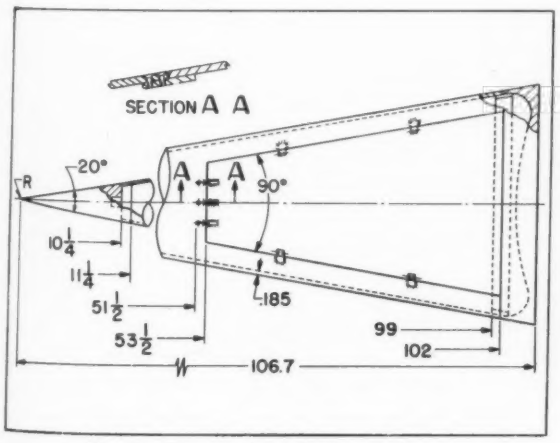

FIG. 7. Structural details of conical nose.

Fig. 9. Conical nose.

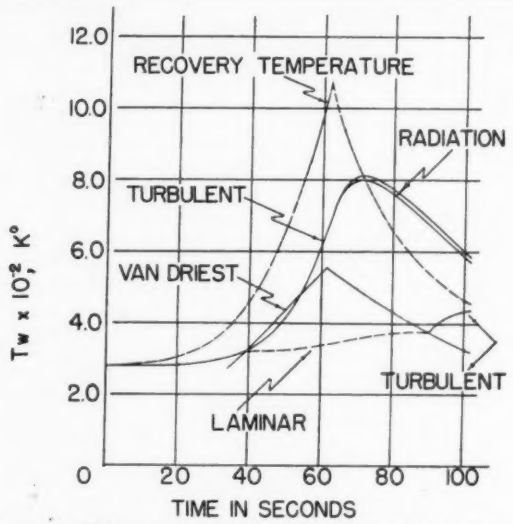

FIG. 10. Skin temperatures for the programmed trajectory.

layer measurements, a rake of tubes was mounted on the surface ahead of the door and the shock wave from the rake would interfere for $M_s < 1.9$. Also, transverse contamination from a turbulent boundary layer on the door would spread along the cone surface. However, available information indicates this angle might be about 10°, whereas it would have to be approximately 25° to influence any of the measuring stations. In summary then, no known disturbances were present for the first 48 in. of the cone; for the measuring stations between 48 and 90 in. from the nose, disturbances created at the door or by boundary-layer tubes just ahead of the door could affect the flow on the smooth side, at least for the most rearward stations, for $M_s < 1.9$. It should be noted that the cone surface Mach Number was greater than 1.9 for the last 13 sec. of the flight.

Choice of Skin Thickness

The wall temperatures representing the stability limit for the programmed trajectory for the V-2, as well as the boundary-layer recovery temperature and some calculated skin temperatures, are shown in Fig. 10. At the time the skin thickness for this experiment had to be chosen (about 2 years ago), only Lees' stability curve was available. Since the stability results were obviously sensitive to the details of the velocity and temperature distributions, it seemed possible that the simplifying assumptions of $\mu \propto T$ and $Pr = 1$ might be important. It was a relatively simple matter to obtain velocity and temperature profiles using the method of Kármán-Tsien and profiles so obtained were used to obtain the curve labeled $\mu \propto T^{0.76}$, $Pr = 1$. It was not obvious that this curve was closer to the truth than Lees' curve, since there was still the $Pr = 1$ assumption; however, since the curve was more conservative than Lees, it was used as a basis for choosing the appropriate skin thickness.

With the programmed flight conditions, the rocket was expected to heat up rapidly, though lagging well behind the boundary-layer recovery temperature. The skin temperatures in Fig. 10 showed that, with the heat capacity of 0.185-in. thick skin, the skin temperature would fall below the limit curves during the acceleration phase.

Determination of the State of the Boundary Layer on the Cone

The identification of the state of the boundary layer in this experiment is based on telemetered measurements of the time rate of heating of the nose and of the total pressure distribution close to the cone surface. At large flight Reynolds Numbers, the turbulent heat-transfer rate is many times larger than the laminar heat-transfer rate. By comparing the measured and predicted surface temperature rise, the two boundary-layer régimes can be differentiated. Also, because of the large R_x's, the turbulent boundary layer should be much thicker than the laminar boundary layer. Total pressure rakes were positioned close to the surface so that, based on estimates for the boundary-layer thickness at the rake, the total pressure tubes would either be within the boundary layer if it was turbulent or outside of the boundary layer if it was laminar. The total pressure value outside the boundary layer can be calculated using the tracking and meteorological data for the flight. Also as an experimental check, an additional total pressure tube was placed 1 in. from the surface, well outside of the predicted turbulent boundary-layer thicknesses. For laminar flow, the rake pressures should be the same as, and equal to, the total pressure referred to above. For turbulent flow, the pressures should decrease going toward the surface, and the actual pressures can be compared with approximate calculations for the total pressure distribution in a turbulent boundary layer at the flight conditions.

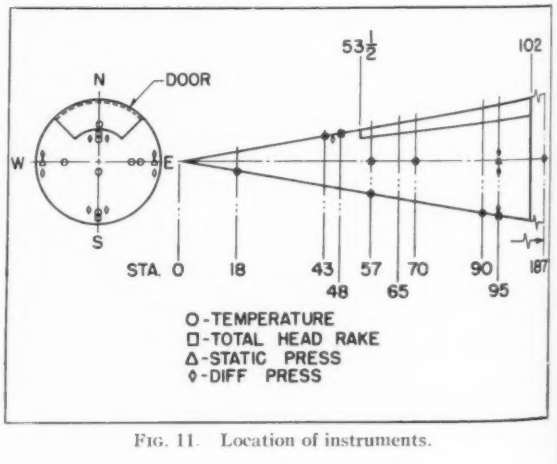

FIG. 11. Location of instruments.

The use of boundary-layer rakes was necessarily restricted because of the resulting flow disturbance. Only two stations were used, one 5 in. ahead of the door and the other on the opposite side of the cone almost at the cone base, 95 in. from the cone tip. Temperature measurements were also made at these two stations, as well as at a number of other locations on the cone surface (see Fig. 11).

Temperature Measurements

The temperature elements were resistance grids about 1 by 2 cm. in size, made of 0.001-diameter Balco wire which has a high temperature coefficient of resistivity (see Fig. 12). By balancing each grid against a fixed Manganin resistor in a battery supplied bridge, temperature changes of the grid wire were converted to voltages from 0 to 5 volts as required by the Hermes telemetering system. There were actually three grids or temperature elements arranged side by side at most of the stations shown on Fig. 11. In order to have sufficient accuracy over the wide range of expected temperatures, the resistances of the grids, the bridge voltages, and reference resistances were chosen so that each of the gages at a given station covered a different temperature range as follows:

A gage 20° to 100° C. for 0–5 volts
B gage 20° to 270° C. for 0–5 volts
C gage 20° to 700° C. for 0–5 volts

Using Sauereisen Cement, the gages were first cemented to an $^1/_8$-in. thick asbestos pad, for convenience in handling, and then were cemented to the inner surface of the skin. Because of the early termination of the flight, only one station reached temperatures above the low (A) temperature range. Since the telemetering accuracy is believed to be 2 or 3 per cent of full scale, only the recordings from the two lowest ranges (A and B) are useful for this firing.

Obviously, the failure of a gage to read correctly might be due to trouble at any one of a number of places in the system between the gage and the film record of the telemetered data. Reliability for a given gage was established by comparing the initial temperature values (at take-off) with the initial temperature values of the other gages and by comparing the temperature changes indicated by the A and B gages at the same temperature station. If the A and B gages at a given station did not satisfy these criteria, then neither of them was used. In all, there were 31 temperature gages and 60 per cent of them gave a satisfactory signal on this basis.

Unfortunately, the temperature gages have a significant effect on the skin temperature being measured. The heat input to the gage resistance wire was large enough to heat the plate in the neighborhood of the gage, at least for the A and B gages (where the heat input was approximately 2.9 watts and 1.3 watts, respectively). In the case of the A gage, this heat input would be sufficient to heat the plate at a rate of 0.6° C. per sec. if the heat were restricted to the plate over the area of the gage. However, heat conduction in the plate greatly reduces the plate temperature rise. Laboratory experiments showed that, after voltage was applied to an A gage, the plate temperature increased about 3.5° in the first minute and then at a rate of about 1° C. every 3 min. The indicated plate temperatures on the V-2 cone were about 10° C. above the air temperature at the start of the flight. By comparing the total heat input from the gages before the start of the flight (power was on about 5 min.) with the indicated plate temperature rise at the gages and the heat capacity of the nose skin, it was clear that there were warm spots in the neighborhood of the gages and that most of the skin was unaffected.

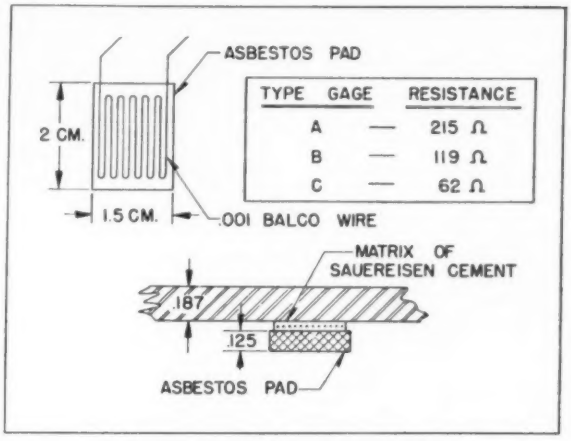

Fig. 12. Typical temperature gage.

On the other hand, where there was a rapid rise of skin temperature during the flight, the asbestos pad acted as a heat sink, since the pad has about 30 per cent of the plate heat capacity for the same surface area. All of this heat capacity is not effective because, as the skin temperature rises, the temperature of the asbestos pad lags far behind. Calculations have been made for the temperature distributions in a pad (one-dimensional) when the temperature of one surface rises at a rate comparable with the experimental rates. After the surface temperature has increased about 50° C., the heat flow into the pad from the heated surface is about 15 per cent of the heat flow into the metal and is approximately equal to the heat input from the A gage. The computations for the skin temperature rise due to aerodynamic heating start with the initial indicated skin temperature, and therefore they include the effect of the heat input from the gages.

Laboratory tests showed that there were other aspects of the performance of the temperature gages which had to be taken into account. It was found that the variation of wire resistance with temperature, with the wire embedded in the Sauereisen Cement, was

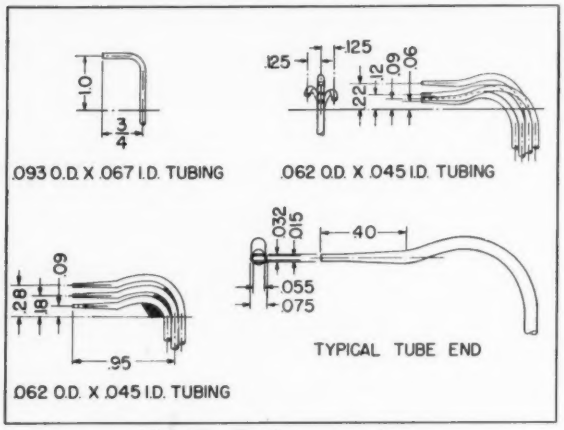

FIG. 13. Total pressure tubes.

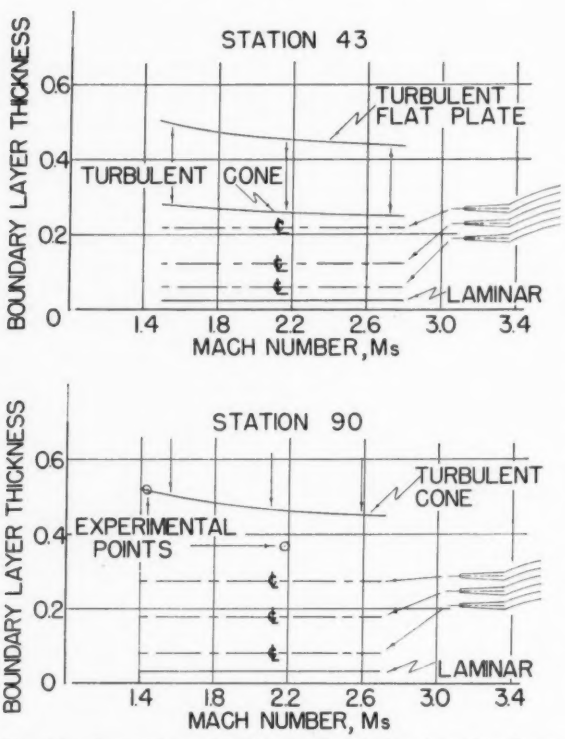

FIG. 14. Comparison of laminar and turbulent boundary-layer thicknesses.

about 10 per cent less than for the wire in air. Also, the layer of cement between the resistance wire and the plate surface is a good enough insulator to maintain a temperature differential between the wire and the plate when the heat generated in the wire flows into the plate. When the plate is only heated by the gage, almost all of the heat input flows into the plate and the wire temperature is about 7° C. higher than the plate temperature. However, when the plate is heated at a representative rate (with a burner) the temperature differential between the wire and the plate decreases, so that, when the plate temperature has risen about 70° C., the indicated temperatures are the same. As noted before, as the plate heats up, the gage heat input and the heat flow to the asbestos pad approach equality. It appears, then, that as the plate temperature rises a rapidly increasing percentage of the heat input from the wire flows into the pad rather than into the plate so that the wire plate temperature differential is reduced. The indicated temperatures have been corrected on the basis of these laboratory experiments.

It should be noted that, at high heat-transfer rates, there will be a measurable temperature variation through the skin. Estimates indicate that, at the highest heat-transfer rates reached during the flight, there should have been about a 6° C. differential between the inner and outer surface. Possibly then, the measured temperatures of the inner skin may have been several degrees lower than the mean temperature of the skin, which was the quantity calculated.

Boundary-Layer Measurements

Fig. 13 shows the details of the boundary-layer rakes. Two of the three-tube rakes, each covering a different pressure range, were placed side by side at Station 95S. The following ranges were obtained on Giannini Pressure Transmitters: (1) 0–75 lbs. per sq.in. for 0–5 volts, and (2) 0–300 lbs. per sq.in. for 0–5 volts. The four-tube rake was placed at Station 48N just ahead of the door. The tube 0.1 in. from the surface transmitted pressures from 0–300 lbs. per sq.in.; the other three tubes covered the range 0–75 lbs. per sq.in. Fig. 14 shows how the tube distances from the surface compare with various estimates of the boundary-layer thickness through the supersonic portion of the flight. The possible extent of the boundary layer, if laminar, is the most important dimension involved, and, fortunately, the estimate for the laminar case should be fairly reliable. The turbulent boundary-layer thicknesses involved more guesswork, and it was hoped that the thickness would actually be large enough to include all of the total pressure tubes.

Skin Temperature Predictions

(a) Laminar Heat Transfer

The theory of the compressible laminar boundary layer has been extensively developed by many authors. However, at high Mach Numbers where there are large temperature variations through the boundary layer, some error may arise from the fact that the Pr is assumed to be constant through the boundary layer. On the basis of available wind-tunnel data, the recovery factor seems to be represented by the theoretical solution $r = \sqrt{Pr}$ if the Pr is based on the wall temperature. (However, the results are for a fairly limited temperature range.) A similar difficulty exists in the prediction of the theoretical dependence of the heat transfer, since the ratio of the local heat transfer

to the local skin friction theoretically should depend on the $(Pr)^{2/3}$. There appear to be insufficient data to show whether using the Pr in this relation, based on the wall temperature, improves or worsens agreement with experiment. However, even relatively large errors in estimating the laminar heat-transfer rate are not important in this experiment, and the calculations have been made as follows: results of reference 11 (including corrections to cone from flat plate) with Pr based on wall conditions.

(b) Turbulent Heat Transfer

The theory for the compressible turbulent boundary layer appears to be in a much more primitive state. Some investigators have predicted that the recovery factory should vary as $Pr^{1/3}$ and be independent of Mach Number, and others predict a Mach Number effect. However, such calculations necessarily involve a large number of arbitrary assumptions. Measurements on a flat plate and cones[12–14] and some recent unpublished measurements on a cone at the Ballistic Research Laboratories give a value for r of about 0.88, with surface temperatures of about 270° K. up to Mach Numbers of 3.5. In view of the uncertainty of the theories at this stage, the wind-tunnel value may be the most reliable value to be used even if the temperatures involved are somewhat different.

Reynolds analogy for obtaining the heat transfer apparently works well for incompressible turbulent flow, and because of this it has been hopefully applied to compressible flow. Some theoretical justification for using the analogy is given by Van Driest[15] for the case when a turbulent Pr (based on an eddy viscosity and eddy heat conductivity) is set equal to one. The dependence of the temperature on the velocity through the boundary layer is found to be the same for both the laminar and the turbulent boundary layers provided mean temperatures and mean velocities are used in the turbulent case. As yet, there does not seem to be a theoretical basis for the dependence of the heat transfer on $(Pr)^{2/3}$, which dependence applies for incompressible turbulent flow and for compressible laminar flow.

Assuming that Reynolds analogy with a $(Pr)^{2/3}$ correction can be used, the problem reduces to predicting the local friction coefficient C_f. Several authors predict a sizable decrease of the local friction coefficient with Mach Number, defining the coefficient for free-stream air properties. Rubesin, et al.,[16] have found good agreement with the predictions of what is called the extended Frankl-Voishel method, and their results have been used for the insulated flat plate Mach Number effect on C_f.

By using the von Karman integral method for the turbulent boundary layer on a cone, the size of the cone boundary layer can be related to the flat plate boundary layer. The turbulent profile on the cone is assumed to be the same as for the flat plate, and the same law for the dependence of the local shear on R_θ is assumed to apply. For the case of this V-2, the situation is complicated by the fact that the effective starting point of the turbulent layer is probably well back on the cone, though its location is uncertain. This is especially true for the flow over the door where the boundary-layer momentum losses produced by the rake or the leading edge of the door are unknown. The correction from a flat plate to a cone when the turbulent boundary layer starts from the tip amounts to an increase of 17 per cent in the local heat-transfer rate.[17] On the other hand, Van Driest predicts some reduction of the local friction coefficient when there is a large degree of cooling. Because of the uncertainties involved, the heat-transfer values used in the computations have not been adjusted either for the correction from the flat plate to the cone or for the effect of a large amount of cooling. This source of error in the heat-transfer values is probably not more than 15 per cent. In summary then, the following expressions have been used for the turbulent heat-transfer calculations on the V-2 nose: (a) $r = 0.88$; (b) Reynolds analogy with Pr correction,

$$h/C_P\rho\,(Pr)^{2/3} = C_f/2$$

($C_f/C_{f_{M=0}}$ from page 29, *N.A.C.A. T.N. No. 2305*), Pr evaluated at wall temperature, and T_s temperature basis used for other terms.

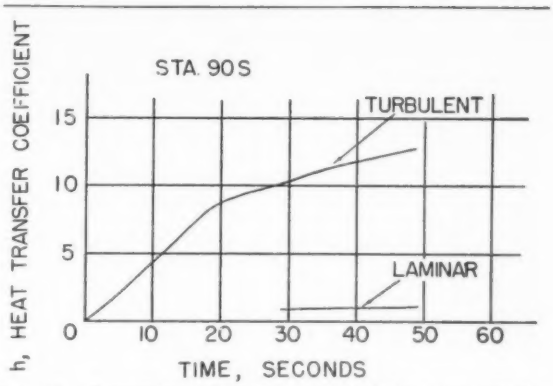

FIG. 15. Comparison of laminar and turbulent heat-transfer coefficients.

It should be noted that, on the basis of theoretical results for $Pr = 1$, the temperature basis for N_u, C_f, and R should be the same. The temperature basis for Pr is arbitrary. Fig. 15 shows the comparison between the laminar and turbulent values for h, where

$$h = q/\Delta T = q/(T_R - T_W)$$

at two stations on the cone. Near the end of the flight, $(T_R - T_W)$ for the turbulent boundary layer is about 80% of $(T_R - T_W)$ for the laminar boundary layer because of the higher skin temperatures in the turbulent case; therefore, the effect of the spread between the h values in Fig. 15 is somewhat lessened.

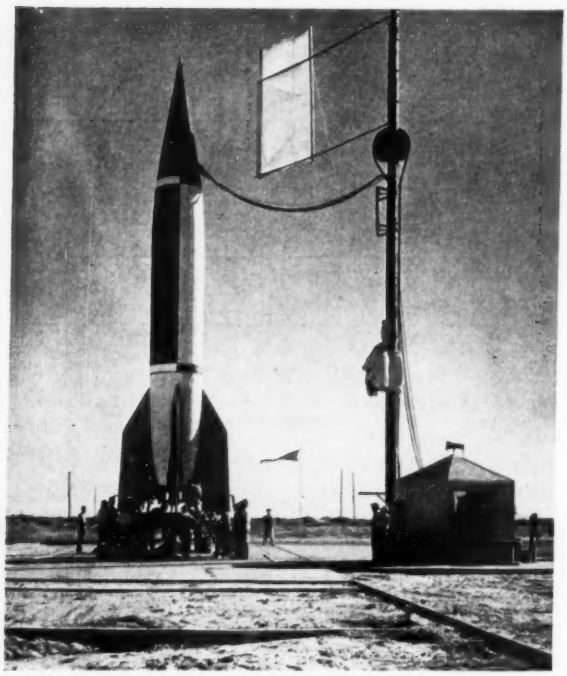

FIG. 16. Rocket at launching site.

SKIN CONDUCTION AND RADIATION

Conduction along the skin presumably caused significant temperature changes where large temperature gradients existed. The solid nose cone and the substantial base ring and associated structure probably remained fairly close to the initial temperature through the flight. Simplified heat-conduction calculations indicated that neither the first station, 6 in. from the solid tip, or the last station, 9 in. upstream of the base structure, should have been appreciably affected by heat-conduction effects. When transition occurred on the cone, it is to be expected that surface temperatures within several inches of the transition region will be modified.

The rocket was fired late in the afternoon, so radiation from the sun was negligible. During the day the rocket nose was shielded from the sun by a sun shade (see Fig. 16).

Calculations show that, at the temperatures reached, radiation from the skin was negligible; if the flight had lasted longer, radiation would have been included (see Fig. 10).

To avoid radiation from the skin to the internal structure, the internal structure was covered with an asbestos pad over which was cemented aluminum foil.

RESULTS

The pressure and temperature structure of the atmosphere was obtained using meteorological balloons. Runs were made before and after the firing both at the launching site and about 12 miles uprange. The data obtained showed that atmospheric conditions were quite stable during the afternoon of the firing. Fig. 17 shows the computed values for the Mach Number and the R_x (for Station 90) based on the trajectory and meteorological data. Using available conical flow tables and the above data, the supposed static pressures on the surface and total pressures near

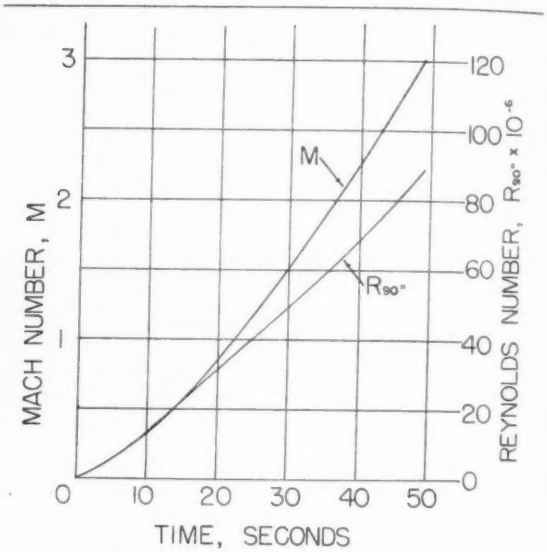

FIG. 17. Mach and Reynolds numbers for flight.

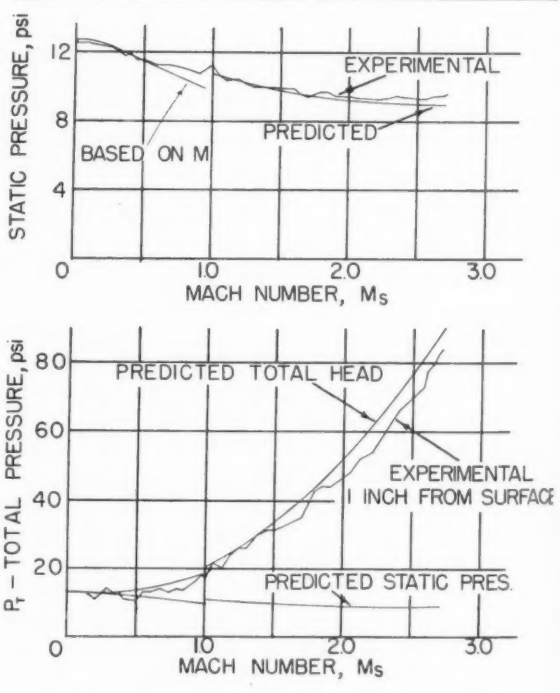

FIG. 18. Total and static pressure near cone surface.

the cone surface were computed. A comparison of the computed and telemetered pressures shows agreement within 2 or 3 per cent which is about the order of the telemetering accuracy (see Fig. 18).

Boundary-layer transition probably occurs well forward on the cone during the subsonic portion of the flight so that, for a transition R_x of say 3×10^6, when $M = 0.8$, transition would be about 10 in. from the cone tip. However, predictions of subsonic transition may be very much in error. The rocket had a sizable angle of attack up to M of approximately 0.8 and through the transonic region from $M_s = 1$ to 1.35, at which point $\alpha = 1°$. Also, there is a high sound level from the motor which can act on the cone boundary layer when $M < 1$. Therefore, it seems reasonable to believe that laminar flow over a large portion of the cone surface would not be realized until $M > 1$.

Computations were made using a step-by-step integration procedure, and the predicted skin temperatures for the two stations where there were both temperature and pressure instrumentation are shown in Figs. 19 and 20. For the calculations, it was arbitrarily assumed that the boundary layer is turbulent up to $M_s = 1.25$ in all cases. Actually, up to this point, the total amount of heat transfer is small so that the accuracy of this assumption is not too important. The temperature measurements on the door are also shown on Fig. 19 for comparison purposes. Since there is little difference between the predicted temperature variation for Stations 43N and 90S, no prediction for Station 65N is shown.

Figure 19 shows the pressure and temperature data for Station 43N. The tubes at 0.07 and 0.14 in. from the surface show excellent agreement with the total pressure for $M_s > 1.25$ up to the limit of their range (75 lbs. per sq.in.). The pressures for the tubes 0.24 and 0.1 in. from the surface are much lower than the total pressure and do not agree with one another. It is hard to see why a total pressure 0.24 in. from the surface should be much less than pressures 0.07 and 0.14 in. from the surface or why pressure 0.1 in. from the surface should be less than the static pressure. We believe that something in the system malfunctioned for these two pressures and that they are not correct. The measured temperatures are in good agreement with the predicted wall temperatures using laminar heat transfer from the time when $M_s = 1.25$. The temperatures at Station 43N also agree generally with the temperature measurements at Stations 18S and 57S (see Fig. 21). The temperature curve for Station 65N on the door is in marked contrast to these data and is fairly close to the turbulent predictions. The approximate nature of the turbulent predictions should be emphasized. The heat-transfer estimates could easily be off by 20–30 per cent, which would correspond to about 15°–22° C. in the final wall temperature. However, even with an error of 50 per cent,

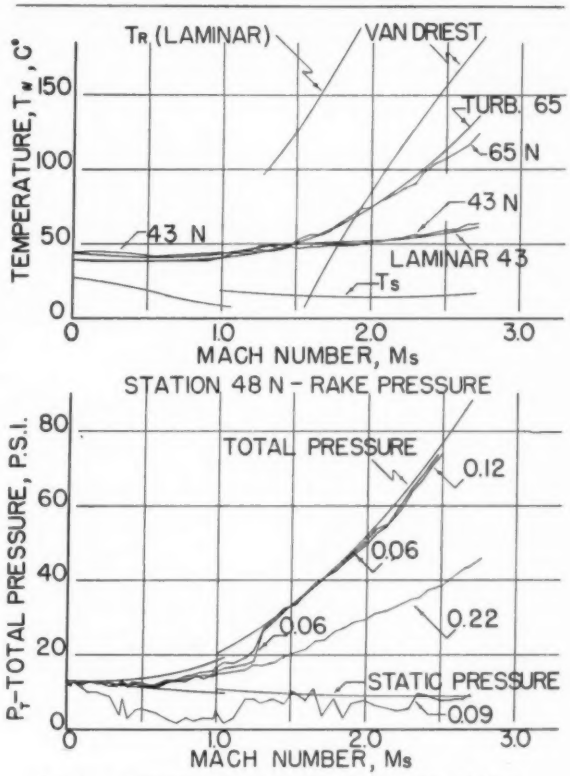

FIG. 19. Temperature and pressure data ahead of door.

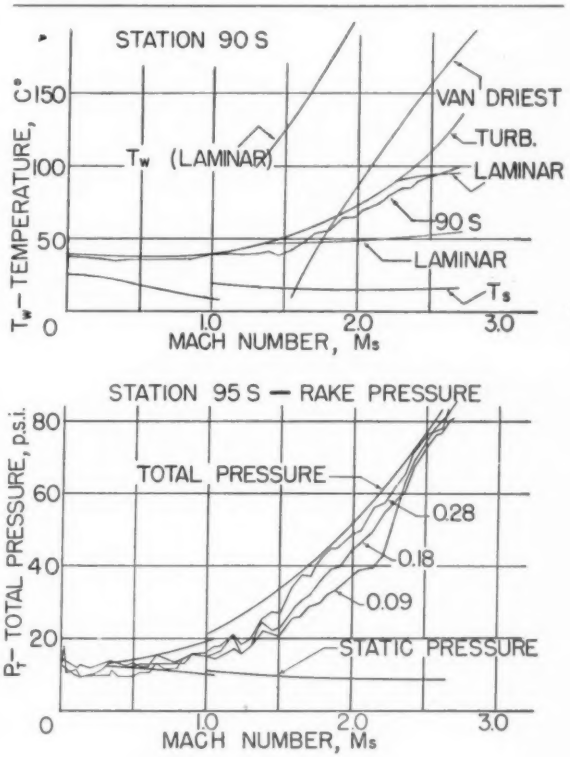

FIG. 20. Temperature and pressure data at cone base.

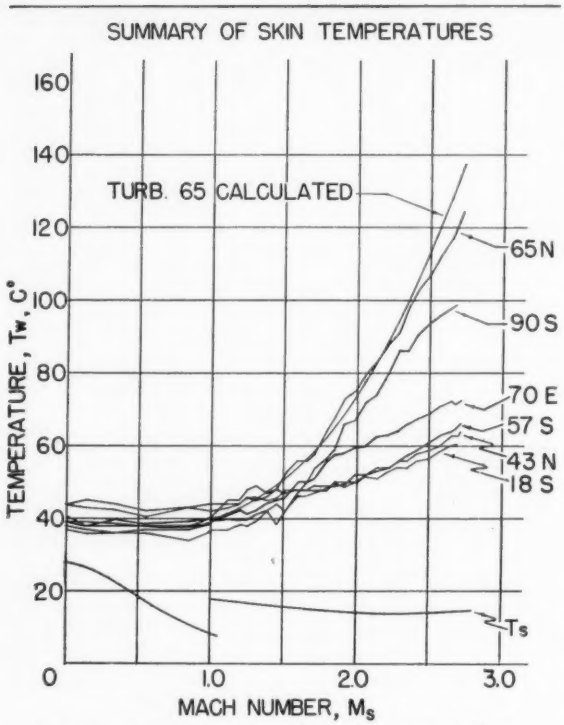

FIG. 21. Temperature data for all of the cone stations.

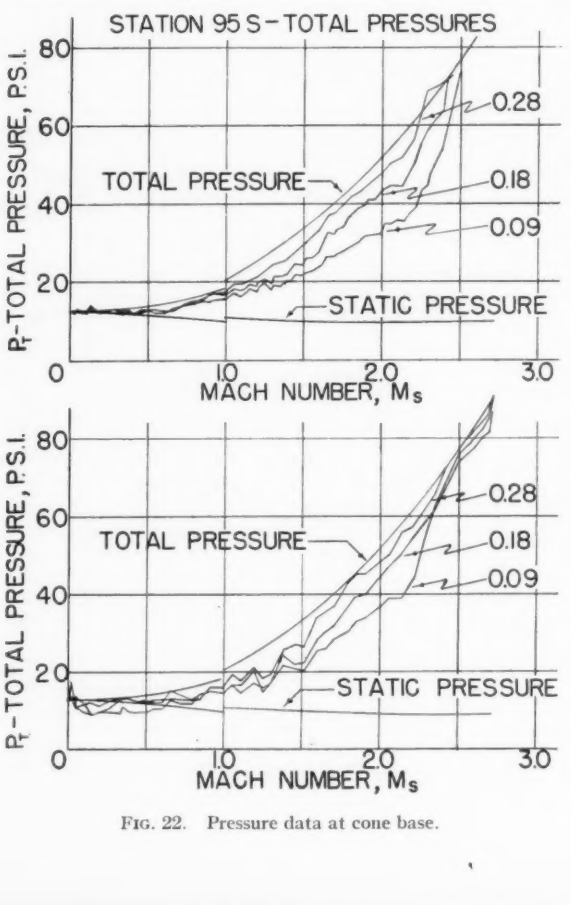

FIG. 22. Pressure data at cone base.

the difference between the laminar and turbulent curves would still be well outside of the estimated experimental error.

Figs. 20 and 22 show the pressure and temperature data for Station 90S. The total pressures for the rake on the coarse range, 0–300 lbs. per sq.in., show a systematic separation up to $M_s = 2.3$, after which they coalesce and follow the total pressure curve to the flight termination. The pressures from the other rake, range 0–75 lbs. per sq.in., show the same separation and coalescence before the pressure range limit is reached (accuracy ≈ 1.5 lbs. per sq.in.).

Assuming a turbulent $Pr = 1$[18], the variation of the total pressure through a turbulent boundary layer for $M = 1.43$ and 2.17 has been computed, and the results are shown in Fig. 23. The velocity was assumed to depend on one-eighth the power of the distance from the wall.

$$u/U_s = (y/\delta)^{1/8}$$

and the experimental wall temperatures were used in obtaining the mean temperature variation across the boundary layer. The experimental results could be compared with these calculations by using predicted boundary-layer thicknesses and the tube distances from the surface for calculating the experimental y/δ values. However, because of the crude nature of the boundary-layer thickness estimates previously indicated, an alternate procedure has been used. The ratio of y/δ for the tube nearest the surface has been arbitrarily set equal to the computed curve. The boundary-layer thicknesses obtained by this procedure are shown on Fig. 14, and they are of the expected magnitude. The y/δ values for the other two pressure tubes can then be computed, and they are shown on Fig. 23. It appears that with the pressure nearest the surface (or either of the other two points) arbitrarily set on the curve, the other two pressures are reasonably consistent with the total pressure variation to be expected through a turbulent boundary layer.

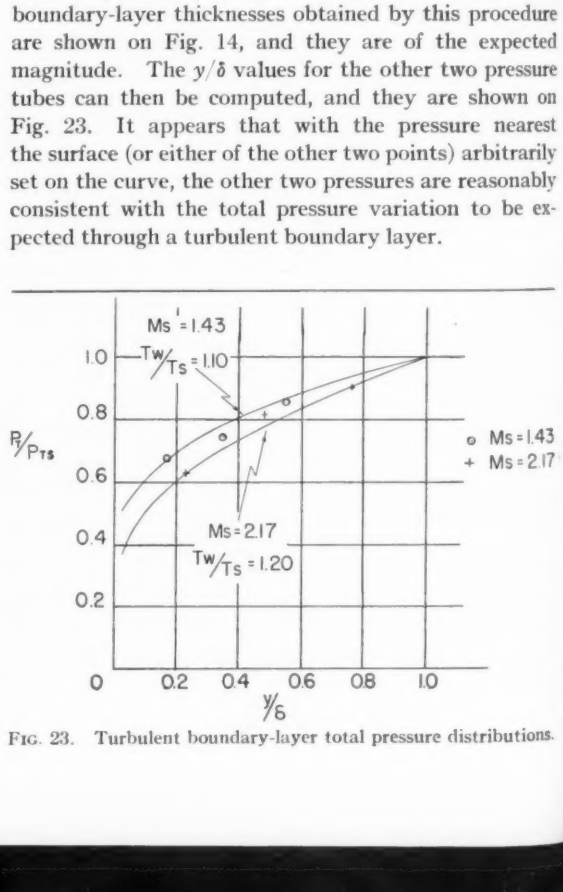

FIG. 23. Turbulent boundary-layer total pressure distributions.

The measured temperatures at Station 90S clearly do not follow the laminar curve and, within the limts previously discussed, correspond to the turbulent curve. There appears to be a break in the measured temperatures when $M_s = 2.3$, although the flight did not last long enough to make this break definitive. For comparison, a computation assuming laminar heat transfer from after $M_s = 2.3$ has been included on Fig. 20. We can only say that, as far as they go, the data are consistent with a change from turbulent to laminar heat transfer about $M_s = 2.3$.

Reference to Figs. 19 and 20 shows that, for the supersonic portion of the flight, the wall temperatures were well below the recovery temperatures, after $M_s = 1.8$ falling below the Van Driest stability limit curve.

Conclusions

The possibility of maintaining supersonic laminar boundary-layer flow at high R has been investigated using the surface of a polished cone more than 8 ft. long as the test area. A modified V-2, with the cone in place of the standard V-2 warhead, was fired in a low trajectory to reach the desired high Reynolds Numbers at supersonic speeds. During most of the supersonic portion of the flight, the heat transfer from the air to the surface was greater than that required to damp small laminar boundary-layer oscillations according to the boundary-layer stability theory.

Telemetered skin temperatures at 43 in. from the tip are in good agreement with skin temperature predictions for laminar flow. Total pressure readings 0.07 and 0.14 in. from the surface indicate that the boundary layer was less than 0.07 in. thick, several times smaller than thickness estimates for a turbulent boundary layer. It is concluded that the flow was laminar at Station 43N from $R_x = 20 \times 10^6$ at $M_s = 1.25$ to $R_x = 40 \times 10^6$ at $M = 2.7$.

Temperature measurements at Stations 18S and 57S also follow the laminar predictions.

The measured temperatures at Station 65N are considered close enough to the calculated values for turbulent flow to indicate that the boundary layer at Station 65N was turbulent. The turbulent state of the flow is attributed to the disturbances caused by the total pressure rake ahead of the door with help from the surface discontinuity at the door's leading edge.

For Station 90S, on the basis of the total pressure measurements with supporting evidence from the skin temperature measurements, it is concluded that the boundary layer was laminar for the last 6 sec. of the flight, during which time the Mach Number increased from 2.3 to 2.7 and the Reynolds Number increased from 75×10^6 to 90×10^6. According to theory, the laminar boundary layer on a cone at some R_x should be 0.58 of the corresponding laminar boundary-layer thickness on a flat plate. On this basis, laminar flow was obtained at $M_s = 2.7$ at an equivalent flat plate R_x of 50×10^6.

References

[1] Lees, Lester, *The Stability of the Laminar Boundary Layer in a Compressible Fluid*, N.A.C.A. T.N. No. 1360, 1947.

[2] Weil, Herschel, *Effects of Pressure Gradient on Stability and Skin Friction in Laminar Boundary Layers in Compressible Fluids*, Journal of the Aeronautical Sciences, Vol. 18, No. 5, p. 311, May, 1951.

[3] Lees, Lester, *Stability of the Supersonic Laminar Boundary Layer with a Pressure Gradient*, Princeton University, Aeronautical Engineering Laboratory Report No. 167, November 20, 1950.

[4] Van Driest, E. R., *Calculation of the Stability of the Laminar Boundary Layer in a Compressible Fluid on a Flat Plate with Heat Transfer*, North American Aviation Report AL-1334.

[5] Liepmann, Roshko, and Sarvan, *On Reflection of Shock Waves from Boundary Layers*, N.A.C.A. T.N. No. 2334, 1951.

[6] Eber, E. R., *Recent Investigation of Temperature Recovery and Heat Transmission on Cones and Cylinders in Axial Flow in the N.O.L. Aeroballistics Wind Tunnel*, Journal of the Aeronautical Sciences, Vol. 19, No. 1, p. 1, January, 1952.

[7] Scherrer, R., *Boundary Layer Transition on a Cooled 20° Cone at Mach Numbers of 1.5 and 2.0*, N.A.C.A. T.N. No 2131, July, 1950.

[8] Higgins, Robert W., and Pappas, Constantine C., *An Experimental Investigation of the Effect of Surface Heating on Boundary Layer Transition on a Flat Plate in Supersonic Flow*, N.A.C.A. T.N. No. 2351, 1951.

[9] Fischer, W. W., and Norris, R. H., *Supersonic Convective Heat Transfer Correlation from Skin Temperature Measurements on a V-2 Rocket in Flight.* Presented at the meeting of the Heat Transfer and Fluid Mechanics Institute, Los Angeles, Calif., June 21, 1948.

[10] Hantzsche and Wendt, *Die laminare Grenzschicht bei einem mit Uberschallgeschwindigkeit angestromten nichtangestellten Kreiskegel*, Jahrbuch Der Deutschen Luftfahrtforschung, 1941.

[11] Crocco, Luigi, *The Laminar Boundary Layer in Gases*, Monografie Scientifiche di Aeronautica No. 3, December, 1946 (Translation); North American Aviation Report CF-1038.

[12] Stalder, Rubesin, and Tendeland, *A Determination of the Laminar-, Transitional-, and Turbulent-Boundary-Layer Temperature-Recovery Factors on a Flat Plate in Supersonic Flow*, N.A.C A. T.N. No. 2077, June, 1950.

[13] Wimbrow, W. R., *Experimental Investigation of Temperature Recovery Factors on Bodies of Revolution at Supersonic Speeds,"* N.A.C.A. T.N. No. 1975, October, 1949.

[14] Stine, H. A., and Scherrer, R., *Experimental Investigation of the Turbulent-Boundary-Layer Temperature-Recovery Factor on Bodies of Revolution at Mach Numbers from 2.0 to 3.8 In.*, N.A.C.A. T.N. No. 2664, March, 1952.

[15] Van Driest, E. R., *Turbulent Boundary Layer for Compressible Fluids on an Insulated Flat Plate*, North American Aviation Report AL-958.

[16] Rubesin, Morris W., Maydew, Randall C., and Varga, Steven A., *An Analytical and Experimental Investigation of the Skin Friction of the Turbulent Boundary Layer on a Flat Plate at Supersonic Speeds*, N.A.C.A. T.N. No. 2305, February, 1951.

[17] Gazley, C., Jr., *Theoretical Evaluation of the Turbulent Skin Friction and Heat Transfer on a Cone in Supersonic Flight*, Report No. R49A0524, General Electric Company, November, 1949.

[18] Van Driest, E. R., *The Turbulent Boundary Layer for Compressible Fluids on a Flat Plate with Heat Transfer*, North American Aviation Report No. AL-997.

On the Flow Behind an Attached Curved Shock*

S. I. PAI†

University of Maryland

SUMMARY

The flow field behind a curved shock is investigated. The essential feature of this flow pattern is that the flow is rotational with nonuniformity of entropy. The characteristic differential equation of the stream function for this flow pattern in both the two-dimensional and the axially symmetrical case is derived and then linearized by an extended form of the Ackeret iteration method.

The first-order linearized differential equation of the stream function, the so-called Sears equation, is solved for the flow over a plane ogive behind an attached curved shock. The flow patterns are divided into two groups—one is designated as "weak shock," behind which the flow is still supersonic, and the other is designated as "strong shock," behind which the flow is subsonic. They are investigated separately. Analytic expressions for the flow field for both cases are obtained. The velocity field can be divided into three components—i.e., one is due to the basic disturbances from the surface of the ogive; the second is due to the reflected disturbances from the shock front; and the third is due to vorticity. Their relative contributions are indicated.

The first-order linearized theory fails at two points: One is that point where the change of stream function due to the change of velocity and that due to the change of density just cancel each other so that the velocity distribution is indeterminate from the stream function. The other point is that at which the reflecting disturbance, itself, satisfies the Rankine-Hugoniot relations; then, according to the first-order linearized theory, the boundary condition at the shock front cannot be satisfied. Both of these points occur in the weak shock region. Excluding the immediate neighborhood of these points, the first-order linearized theory shows the general behavior of the flow pattern behind the curved shock. Within the neighborhood of these two singular points, it is suggested that the exact differential equation should be used which can be solved by the method of characteristics because the flow behind the attached shock is still supersonic.

LIST OF SYMBOLS

a = local sound speed
A = $(S - S_0)/C_v$
b = factor defined by Eq. (45)
C = constant
C_p = specific heat at constant pressure
C_v = specific heat at constant volume
d_1 = small height
f = arbitrary function
h = enthalpy
M = Mach Number
p = pressure
q = magnitude of velocity
R = gas constant
R_f = reflection factor defined by Eq. (44)
S = entropy
T = absolute temperature
U, V = velocity components along x- and y-axis, respectively
u, v = perturbation flow velocity components along x- and y-axis, respectively
x, y = reference axes
α = shock angle with respect to U_1
γ = C_p/C_v
δ = shock angle with respect to U_2
ϵ = 0 for two-dimensional flow
ϵ = 1 for axially symmetrical flow
η = variable similar to y
μ = $\sqrt{\lvert 1 - M_2^2 \rvert}$
ρ = density
σ = arc length along the shock front
ψ = stream function
ω = vorticity

Subscripts

1 = value ahead of shock except as otherwise specified
2 = value behind the shock except as otherwise specified
0 = some reference value

(I) INTRODUCTION

ALTHOUGH FLOWS INVOLVING a curved shock are of great theoretical interest and practical importance, our knowledge is limited. One of the essential characteristics of flows behind a curved shock is that the flow is rotational and the entropy distribution varies normal to the stream lines. Furthermore, the distribution of entropy is in general not known *a priori* and depends on the solution of the problem. This is one of the difficulties in solving the problem of flow behind a curved shock. Another difficulty is the nonlinearity of the differential equation that governs the flow of a compressible fluid. In the present paper, an iteration method is suggested to study the whole pattern of flow behind the curved shock.

The differential equation of the stream function in rotational flow is linearized by an extended form of the Ackeret iteration method.[3] This linearization is accomplished by assuming the development of the stream function ψ to be of the form

$$\psi = \psi_0(x, y) + \psi_1(x, y) + \psi_2(x, y) + \psi_3(x, y) + \dots \tag{1}$$

where $\psi_0(x, y)$ is a certain known solution for irrotational motion corresponding to the problem considered. ψ_1 is the first-order perturbation of ψ_0. For the purpose of defining the iteration procedure, the function ψ_{n+1} is regarded as small compared with the preceding

Received May 15, 1952.

* This paper is based on the work that author did for Cornell Aeronautical Laboratory, Inc., Buffalo, N.Y., in 1949, under Navy Bureau of Ordnance Contract NOrd 10057.

† Associate Research Professor, Institute for Fluid Dynamics and Applied Mathematics.

function ψ_n, and the derivatives have similar relationships. Then, the total index decides the order of the terms; for example, ψ_2 is of the same order as ψ_1^2 or $\psi_0\psi_2$.

In order to solve the linearized equations of ψ_n's, we have to know the entropy distribution in the flow which is not known *a priori* but should be consistent with the stream lines of the given problem. Thus the equation of ψ_n's is the so-called "*self-consistent*" equation that often occurs in many problems in theoretical physics and which can be solved by a method of iteration.

Finally, we investigate the flow over a plane ogive behind the attached curved shock by the method developed above. The flow field has been analyzed in detail in order to determine the relative contribution of rotationality and other factors.

When the flow behind the curved shock is supersonic, the method of characteristics can be used to calculate the flow pattern numerically. One of the disadvantages of an all-numerical method is that it is difficult to obtain general conclusions. Furthermore, if the flow behind the curved shock is subsonic, the method of characteristics cannot be used. In the present method, both the supersonic and the subsonic flows behind the curved shock can be investigated and analytic expressions can be obtained so that general conclusions may be drawn.

In this paper, the flow is considered as steady, inviscid, and adiabatic. Furthermore, the flow in front of the curved shock is assumed to be uniform—i.e., isentropic and irrotational—hence, the whole flow field is isoenergetic.

(II) Fundamental Equations

Consider two-dimensional or axisymmetric flow with velocity components U and V along the x and y direction. A stream function may be defined in order to satisfy the equation of continuity such that

$$\frac{\partial \psi}{\partial y} = \rho U y^{\epsilon}, \qquad \frac{\partial \psi}{\partial x} = -\rho V y^{\epsilon} \tag{2}$$

where $\epsilon = 0$ for two-dimensional flow and $\epsilon = 1$ for axisymmetric flow.

For steady isoenergetic flow, the vorticity ω for the present cases may be written as

$$\omega = \frac{\partial V}{\partial x} - \frac{\partial U}{\partial y} = \frac{p}{R}\frac{dS}{d\psi} y^{\epsilon} \tag{3}$$

where S is the entropy.

The differential equation for the stream function ψ of the rotational flow[1]

$$\left(1 - \frac{U^2}{a^2}\right)\frac{\partial^2 \psi}{\partial x^2} - 2\frac{UV}{a^2}\frac{\partial^2 \psi}{\partial x\,\partial y} + \left(1 - \frac{V^2}{a^2}\right)\frac{\partial^2 \psi}{\partial y^2} - \frac{\epsilon}{y}\frac{\partial \psi}{\partial y} = -\rho y^{\epsilon}\omega\left\{1 + \frac{\gamma - 1}{\rho^2 a^2 y^{\epsilon}}\left[\left(\frac{\partial \psi}{\partial x}\right)^2 + \left(\frac{\partial \psi}{\partial y}\right)^2\right]\right\} \tag{4}$$

If the vorticity ω or the variation of entropy with stream lines $dS/d\psi$ vanishes, Eq. (4) reduces to the well-known equation of stream function for irrotational flow.

The equation of state for the adiabatic flow is

$$p/\rho^{\gamma} = e^{S/C_V} = f(\psi) \tag{5}$$

For isoenergetic flow, if T_0 is the stagnation temperature, we have

$$\frac{T}{T_0} = 1 - \frac{\gamma - 1}{2}\frac{1}{\rho a_0^2 y^{\epsilon 2}}\left[\left(\frac{\partial \psi}{\partial x}\right)^2 + \left(\frac{\partial \psi}{\partial y}\right)^2\right] \tag{6}$$

Therefore, together with Eqs. (5) and (6), Eq. (4) is the differential equation for the stream function in rotational flow. It can be investigated if ω or $dS/d\psi$ is specified. However, in the case of flow behind a curved shock, ω or $dS/d\psi$ is specified by the shape of the curved shock which itself has to be fixed by matching the flow calculated by Eq. (4) to that given by the shock-wave equation. The problem is thus rather complicated. However, we shall show that it can be solved by the method of iteration.

(III) Linearization of the Differentiation Equation of Stream Function

In order to linearize Eq. (4), we assume that the stream function ψ can be developed into the form of Eq. (1). $\psi_0(x, y)$ is a certain known solution for irrotational motion corresponding to the problem considered. The simplest form of ψ_0 will be that of uniform flow with velocity U_0—i.e.,

$$\psi_0 = [\rho_0 U_0/(1 + \epsilon)]y^{1+\epsilon}$$

Another simple form of ψ_0 will be the solution for flow over an unyawed cone which is useful in the case of axisymmetric flow. The order of the terms is decided by the total index, as explained before.

In order to find the equations for the ψ_n's, we have to calculate the density ratio in terms of ψ_n and the entropy perturbation because, in the present problem, the perturbed velocity is of the same order of magnitude as the perturbed entropy.

Write

$$\left.\begin{aligned} \frac{\partial \psi_0}{\partial y} &= \rho_0 U_0 y^{\epsilon}, \quad \frac{\partial \psi_0}{\partial x} = -\rho_0 V_0 y^{\epsilon} \\ q_0^2 &= U_0^2 + V_0^2,\ M_0 = q_0/a_0 \end{aligned}\right\} \tag{6a}$$

The density ratio ρ_0/ρ obtained from the energy equation is as follows:

$$\rho_0/\rho = 1 + \zeta \tag{7}$$

where

$$\zeta = \frac{M_0^2}{1 - M_0^2}\frac{U_0}{\rho_0 q_0^2 y^{\epsilon}}\frac{\partial \psi_1}{\partial y} - \frac{M_0^2 V_0}{(1 - M_0^2)\rho_0 q_0^2 y^{\epsilon}}\frac{\partial \psi_1}{\partial x} + \frac{A}{(\gamma - 1)(1 - M_0^2)} + \dots \tag{8}$$

$$A = (S - S_0)/C_v \tag{9}$$

which is of the same order of magnitude as ψ_1.

The vorticity ω in iteration form is

$$\omega = \omega_1 + \omega_2 + \omega_3 + \dots \tag{10}$$

Substituting Eqs. (1) and (10) into Eq. (4) and with the help of Eq. (7), and collecting terms of same order of magnitude, we have

$$\left(1 - \frac{U_0^2}{a_0^2}\right)\frac{\partial^2\psi_0}{\partial x^2} - \frac{2U_0V_0}{a_0^2}\frac{\partial^2\psi_0}{\partial x\,\partial y} + \left(1 - \frac{V^2}{a_0^2}\right)\frac{\partial^2\psi_0}{\partial y^2} - \frac{\epsilon}{y}\frac{\partial\psi_0}{\partial y} = 0 \tag{11}$$

This is the equation of the stream function for irrotational flow. Hence, our assumption that ψ_0 is a solution for irrotational flow is satisfied.

The first-order differential equation for the perturbed stream function ψ_1 is

$$\left(1 - \frac{U_0^2}{a_0^2}\right)\frac{\partial^2\psi_1}{\partial x^2} - \frac{2U_0V_0}{a_0^2}\frac{\partial^2\psi_1}{\partial x\,\partial y} + \left(1 - \frac{V_0^2}{a_0^2}\right)\frac{\partial^2\psi_1}{\partial y^2} - \frac{\epsilon}{y}\frac{\partial\psi_1}{\partial y} - \frac{U_0^2}{a_0^2}\frac{\partial^2\psi_0}{\partial x^2}\left[\left(KU_0 + \frac{2}{U_0L}\right)\times \frac{\partial\psi_1}{\partial y} - KV_0\frac{\partial\psi_1}{\partial x} + A^*\right] - 2\frac{U_0V_0}{a_0^2}\frac{\partial^2\psi_0}{\partial x\,\partial y}\left[\left(KU_0 + \frac{1}{U_0L}\right)\frac{\partial\psi_1}{\partial y} - \left(KV_0 + \frac{1}{V_0L}\right)\frac{\partial\psi_1}{\partial x} + A^*\right] - \frac{V_0^2}{a_0^2}\frac{\partial^2\psi_0}{\partial y^2}\left[KU_0\frac{\partial\psi_1}{\partial y} - \left(KV_0 + \frac{2}{V_0L}\right)\frac{\partial\psi_1}{\partial x} + A^*\right] = -\rho_0 y^\epsilon\,\omega_1\,[1 + (\gamma - 1)\,M_0^2] \tag{12}$$

where

$$\left.\begin{aligned} K &= (\gamma + 1)M_0^2/(1 - M_0^2)\rho_0 q_0^2 y^\epsilon \\ L &= \rho_0 y^\epsilon \\ A^* &= [2A/(\gamma - 1)\,(1 - M_0^2)]\,\{1 + [(\gamma - 1)/2]\,M_0^2\} \end{aligned}\right\} \tag{13}$$

If the basic flow is a uniform flow of velocity U_0 = constant and $V_0 = 0$, the first-order equation of ψ_1 becomes

$$\left(1 - \frac{U_0^2}{a_0^2}\right)\frac{\partial^2\psi_1}{\partial x^2} + \frac{\partial^2\psi_1}{\partial y^2} - \frac{\epsilon}{y}\frac{\partial\psi_1}{\partial y} = -\rho_0 y^\epsilon\,\omega_1\,[1 + (\gamma - 1)M_0^2] \tag{14}$$

This equation was first derived by Sears.[2]

For the case of uniform basic flow, the second-order differential equation of perturbed stream function for rotational flow is

$$\left(1 - \frac{U_0^2}{a_0^2}\right)\frac{\partial^2\psi_2}{\partial x^2} + \frac{\partial^2\psi_2}{\partial y^2} - \frac{\epsilon}{y}\frac{\partial\psi_2}{\partial y} = \frac{U_0^2}{a_0^2}\frac{\partial^2\psi_1}{\partial x^2}\left[\left(KU_0 + \frac{2}{U_0L}\right)\frac{\partial\psi_1}{\partial y} + A^*\right] - 2\frac{\partial^2\psi_1}{\partial x\,\partial y}\frac{U_0}{La_0^2}\frac{\partial\psi_1}{\partial x} - \rho_0 y^\epsilon(-\zeta\omega_1 + \omega_2)\,[1 + (\gamma - 1)\,M_0^2] - \rho_0\,y^\epsilon\,\omega_1(\gamma - 1)\,M_0^2 \left\{\frac{2}{\rho_0 y^{2\epsilon} q_0^2}\left[\rho_0 U_0 y^\epsilon\left(\frac{\partial\psi_1}{\partial y}\right)\right] + KU_0\frac{\partial\psi_1}{\partial y} + A^*\right\} \tag{15}$$

In order to solve Eq. (12), (14), or (15), we have to know the distribution of vorticity or $dS/d\psi$ in the flow. The entropy S is a function of the shock angle α of the curved shock with respect to the uniform stream M_1 in front of the curved shock, which is

$$\frac{S - S_1}{C_v} = \log\left[\left(\frac{2\gamma}{\gamma + 1}M_1^2\sin^2\alpha - \frac{\gamma - 1}{\gamma + 1}\right)\left(\frac{\gamma - 1}{\gamma + 1} + \frac{2}{(\gamma + 1)M_1^2\sin^2\alpha}\right)^\gamma\right] \tag{16}$$

From Eq. (16) we have

$$\frac{dS}{d\psi} = \frac{1}{\sin\delta}\,\frac{1}{\rho q y^\epsilon}\,\frac{dS}{d\alpha}\,\frac{d\alpha}{d\sigma} \tag{17}$$

where δ is the shock angle with respect to the flow behind the curved shock and σ is the arc length along the shock front.

If the shape of the curved shock $d\alpha/d\sigma$ is given, we can calculate $dS/d\psi$ by Eq. (17), and then the equation of the stream function can be investigated. However, for most of the practically interesting problems, the shape of the shock is not known *a priori* but should be consistent with the stream lines of the given problem—i.e., it depends on the solution of the equation of the stream function. This is the so-called "self-consistent" equation, which can be solved by the method of iteration as follows:

First, we assume that the flow is irrotational and obtain the solution ψ_1 for the given boundary conditions, say

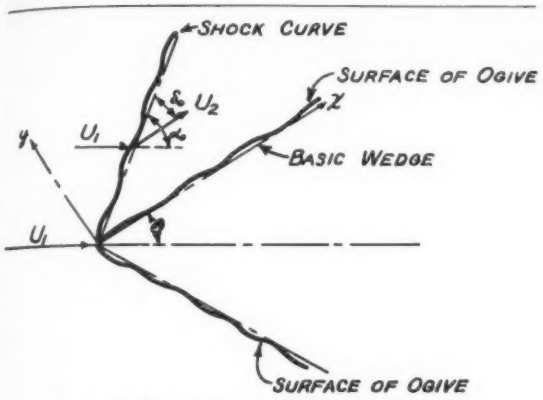

FIG. 1. Uniform supersonic flow over plane ogive.

$$\psi_1 = f_0(x, y) \tag{18}$$

For the irrotational flow, the original shock is straight, which location is known. At the position of the original straight shock, we can determine the curvature of the stream line behind the shock from Eq. (18), and then we obtain $d\alpha/d\sigma$ along the locus of the straight shock. Finally, we can calculate $dS/d\psi$ by Eq. (17).

Substituting $dS/d\psi$ so obtained into the equation of ψ_1 and solving it for the given boundary conditions again, we obtain a new solution, say

$$\psi = f_1(x, y) \tag{19}$$

This process can be repeated until f_n is equal to f_{n-1} or until the desired accuracy is obtained.

We are going to apply this method to study the flow over a plane ogive behind an attached curved shock. Only the first-order perturbation theory is carried out in detail. Extension to the higher order theory may be made by a similar procedure.

(IV) Uniform Supersonic Flow over Plane Ogive

We consider a uniform supersonic flow of ideal gas passing over a plane ogive. If the leading-edge angle of the ogive is smaller than the critical angle, a curved shock front is attached to the vertex of the ogive. Behind the curved shock, the flow is rotational with non-uniform entropy. From the shock polar it is well known that, for a given angle of deflection of flow, there are two possible configurations of shock angles—the strong shock and the weak shock. Behind the weak shock, the flow is usually supersonic; while, behind the strong shock, the flow is always subsonic. These two cases should be treated separately, because the fundamental differential equations for the stream function are of different nature—i.e., one is of hyperbolic type and the other is of elliptical type.

The basic flow in this case will be that passing over a wedge that will be closely approximated to the ogive (Fig. 1). Since the flow in front of the shock is supersonic and the curved shock is attached to the ogive, the flow over the upper half of the ogive is independent of that over the lower half. One may thus consider the half plane only. We choose the x-axis along the surface of the wedge and the y-axis perpendicular to the x-axis. Hence, the surface of the ogive will be

$$y = d_1 Y(x) \tag{20}$$

where d_1 is a small quantity of same order of magnitude as ψ_1. $Y(x)$ gives the geometrical shape of the ogive.

The location of the curved shock will be approximately on the line

$$y = x \tan \delta_0 \tag{21}$$

The basic flow is now a uniform flow of velocity U_2 and density ρ_2. In the rest of this paper we will use a nondimensional form for the stream function, which is defined as

$$\left.\begin{aligned} \frac{\partial \psi}{\partial y} &= \frac{\rho U}{\rho_2 U_2} = \frac{\rho}{\rho_2}\left(1 + \frac{u}{U_2}\right) \\ \partial\psi/\partial x &= -(\rho V/\rho_2 U_2) \end{aligned}\right\} \tag{22}$$

where $U = U_2 + u$ and $V = v$ are the resultant velocity components behind the curved shock. Hence, the relations between the perturbed stream function ψ_1 and the perturbed velocity components u, v and density $\Delta\rho = \rho - \rho_2$ are

$$\left.\begin{aligned} \partial\psi_1/\partial y &= (\Delta\rho/\rho_2) + (u/U_2) \\ \partial\psi_1/\partial x &= -(v/U_2) \end{aligned}\right\} \tag{23}$$

where

$$\frac{\Delta\rho}{\rho_2} = -M_2^2 \frac{u}{U_2} - \frac{S - S_1}{R} \tag{24}$$

The boundary conditions of the present problems are as follows:

The condition that the surface of the ogive is a stream line gives

$$\psi[x, d_1 Y(x)] = 0 \tag{25}$$

For the first-order theory, Eq. (25) becomes

$$\psi_1(x, 0) = -d_1 Y(x) \tag{26}$$

This is one of the boundary conditions for $\psi_1(x, y)$, which is to be satisfied at the axis $y = 0$ but not at the profile.

Let the shock angle with respect to the uniform flow in front of the curve be $\alpha_0 + \alpha$ where α_0 is the shock angle of the basic flow with respect to U_1 and α is the first-order perturbed shock angle.

Under the assumption of small perturbation, it is possible to find the relations of α to the perturbed velocity components u_s, v_s immediately behind the curved shock as follows:

$$u_s = U_\alpha \cdot \alpha, \qquad v_s = V_\alpha \cdot \alpha \tag{27}$$

where

$$U_\alpha = U_1 U_{\alpha_1} = U_1 \frac{[(\rho_1/\rho_2) - 1] \sin(\alpha_0 + \delta_0)}{1 + K_p U_2^2 \sin^2 \delta_0} \tag{28}$$

$$V_\alpha = U_1 V_{\alpha_1} = U_1 \frac{[(\rho_1/\rho_2) - 1]\,[K_\rho U_2^2 \sin \alpha_0 \sin \delta_0 - \cos\,(\alpha_0 + \delta_0)]}{1 + K_\rho U_2^2 \sin^2 \delta_0} \tag{29}$$

and U_1 and ρ_1 are the velocity and the density in front of the shock, respectively. δ_0 is the shock angle of the basic flow with respect to U_2.

$$K_\rho = -\frac{\gamma - 1}{\gamma}\frac{\rho_2}{p_2}\frac{\left(\frac{\gamma+1}{\gamma-1} - \frac{\rho_1}{\rho_2}\right)\left(\frac{\gamma+1}{\gamma-1} - \frac{\rho_2}{\rho_1}\right)}{\frac{\gamma+1}{\gamma-1}\left(\frac{\rho_2}{\rho_1} + \frac{\rho_1}{\rho_2}\right) - 2} \tag{30}$$

$$(\Delta\rho/\rho_2)_s = K_\rho U_2 u_s \tag{31}$$

Eq. (31) shows the relation between the perturbation density and x-wise velocity component immediately behind the shock, which is obtained from the energy equation. Fig. 2 shows a typical variation of $K_\rho U_2^2$ at a given $M_1 = U_1/a_1$.

The variation of the shock angle α is obtained from Eqs. (23), (27), and (31) as follows:

$$\alpha = \frac{u_s}{U_\alpha} = \left(\frac{U_2}{U_1}\right)\frac{1}{U_{\alpha_1}(1 + K_\rho U_2^2)}\frac{\partial \psi_1}{\partial y} \tag{32}$$

at $y = x \tan \delta_0$.

The first-order vorticity ω_1 is

$$\omega_1 = \frac{U_2}{\gamma(\gamma - 1)M_2^2}\left[\frac{1}{C_V}\frac{dS}{d\alpha}\right]\frac{d\alpha}{dy} = U_2\omega_1' \tag{33}$$

(say), where

$$\frac{1}{C_V}\frac{dS}{d\alpha} = \frac{2\gamma M_1^2 \sin 2\alpha_0[(\gamma - 1)M_1^2 \sin^2 \alpha_0 + 2] - 4\gamma \cot \alpha_0[2\gamma M_1^2 \sin^2 \alpha_0 - (\gamma - 1)]}{[(\gamma - 1)M_1^2 \sin^2 \alpha_0 + 2]\,[2\gamma M_1^2 \sin^2 \alpha_0 - (\gamma - 1)]} \tag{34}$$

Finally, our problem is to solve the nondimensional differential equation for ψ_1.

$$(M_2^2 - 1)\frac{\partial^2 \psi_1}{\partial x^2} - \frac{\partial^2 \psi_1}{\partial y^2} = \omega_1'[1 + (\gamma - 1)M_2^2] = \omega_{10}(x, y) \tag{35}$$

with the boundary conditions

$$\psi_1(x, 0) = -d_1\, Y(x) \tag{36}$$

$$\frac{\partial \psi_1(x, x \tan \delta_0)}{\partial y} = -\frac{U_{\alpha_1}}{V_{\alpha_1}}(1 + K_\rho U_2^2)\frac{\partial \psi_1(x, x \tan \delta_0)}{\partial x} \tag{37}$$

The last boundary condition shows that the perturbed velocity components must match those given by Rankine-Hugoniot relations—i.e., Eqs. (27). At the shock line, $y = x \tan \delta_0$.

(V) Weak Attached Shock—Supersonic Flow Behind the Curved Shock

When the strength of the basic shock is not large enough, the flow behind the shock is still supersonic—i.e., $M_2 > 1$. Eq. (35) is of hyperbolic type.

The inhomogeneous partial differential equation [Eq. (35)] with the boundary conditions (36) and (37) can be solved by the following procedure: Write

$$\psi_1 = \psi_{10} + \psi_{11} \tag{38}$$

where ψ_{10} and ψ_{11} are functions such that

$$\left.\begin{aligned} \mu^2\,(\partial^2\psi_{10}/\partial x^2) - (\partial^2\psi_{10}/\partial y^2) &= 0 \\ \psi_{10}(x, 0) &= -d_1\, Y(x) \\ \frac{\partial \psi_{10}(x, x \tan \delta_0)}{\partial y} &= -\frac{U_{\alpha_1}}{V_{\alpha_1}}(1 + K_\rho U_2^2) \times \\ & \qquad \frac{\partial \psi_{10}(x, x \tan \delta_0)}{\partial x} \end{aligned}\right\} \tag{39}$$

where $\mu^2 = M_2^2 - 1$ and

$$\mu^2\frac{\partial^2 \psi_{11}}{\partial x^2} - \frac{\partial^2 \psi_{11}}{\partial y^2} = \omega_1'[1 + (\gamma - 1)M_2^2] = \omega_{10}(x, y)$$

$$\psi_{11}(x, 0) = 0 \tag{40}$$

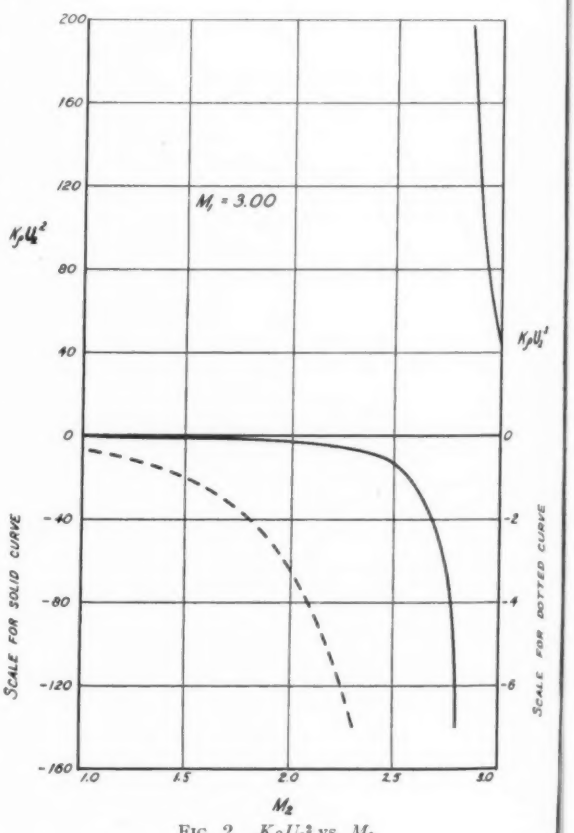

Fig. 2. $K_\rho U_2^2$ vs. M_2.

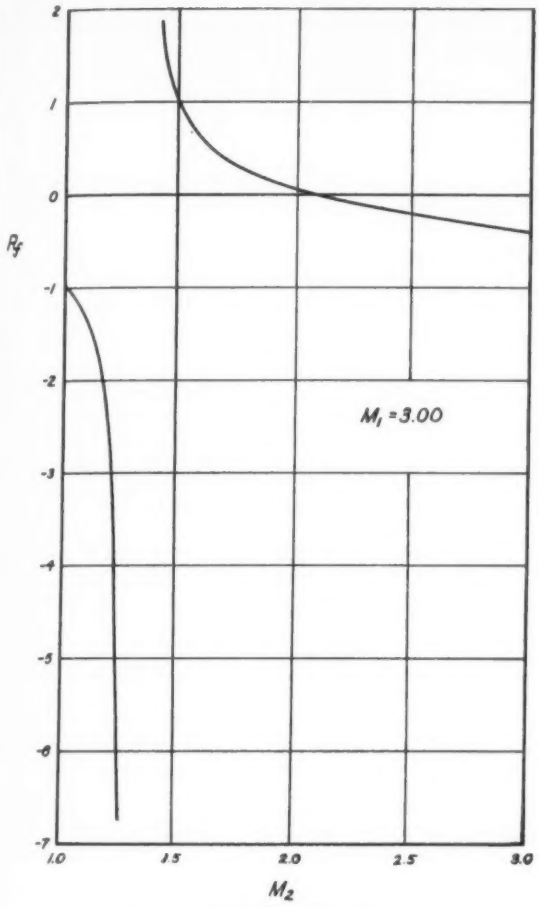

FIG. 3. Reflection factor R_f.

$$\frac{\partial \psi_{10} + \psi_{11}}{\partial y} = -\frac{U_{\alpha_1}}{V_{\alpha_1}}(1 + K_\rho U_2^2)\frac{\partial \psi_{10} + \psi_{11}}{\partial x}$$

at $y = x \tan \delta_0$.

The solution of Eq. (39) is

$$\psi_{10} = -d_1[f(x - \mu y) + f_r(x + \mu y)] \tag{41}$$

where $f(x - \mu y)$ represents the basic disturbance originating from the surface $Y(x)$ and $f_r(x + \mu y)$ represents the reflected disturbances from the shock front. The functions f and f_r can be determined from the boundary conditions. From the first boundary condition of Eq. (39), we have

$$f(x) + f_r(x) = Y(x) \tag{42}$$

From the second boundary condition of Eq. (39), we have

$$f_r(x) = (R_f/b)\, f(bx) \tag{43}$$

where

$$R_f = \frac{\mu V_{\alpha_1} - U_{\alpha_1}(1 + K_\rho U_2^2)}{\mu V_{\alpha_1} + U_{\alpha_1}(1 + K_\rho U_2^2)} \tag{44}$$

$$b = (1 - \mu \tan \delta_0)/(1 + \mu \tan \delta_0) \tag{45}$$

Fig. 3 shows a typical variation of R_f at a given M_1. Substituting Eq. (43) into Eq. (42), we have

$$f(x) + (R_f/b)\, f(bx) = Y(x) \tag{46}$$

The expression of the basic disturbance function $f(x)$ can be determined from Eq. (46). Hence, ψ_{10} is obtained.

In order to solve Eq. (40), we must first know the expression ω_1'. Since ω_1' depends on the solution of Eq. (35), it can only be estimated by the method of iteration. For first approximation, we estimate ω_1' by putting $\psi_1 = \psi_{10}$; hence,

$$\alpha \cong \left(\frac{U_2}{U_1}\right)\frac{1}{U_{\alpha_1}(1 + K_\rho U_2^2)}\frac{\partial \psi_{10}}{\partial y} \tag{47}$$

at $y = x \tan \delta_0$. From Eqs. (47) and (33), we have

$$\omega_{10}(x, y) \cong -K_\omega d_1 \mu \frac{df'[(\cot \delta_0 - \mu)y]}{dy} = \omega_{10}(y) \tag{48}$$

where

$$K_\omega = -\frac{1 - R_f}{\gamma(\gamma - 1)M_2^2}\frac{[1 + (\gamma - 1)M_2^2]}{(1 + K_\rho U_2^2)U_{\alpha_1}} \times \left(\frac{U_2}{U_1}\right)\left(\frac{1}{C_v}\frac{dS}{d\alpha}\right) = (1 - R_f)K_\omega' \tag{49}$$

Fig. 4 shows a typical variation of K_ω' at a given M_1.

In order to solve Eq. (40), we express $\omega_{10}(x, y)$ in terms of Fourier integral of x as follows:

$$\omega_{10}(x, y) = \frac{1}{\pi}\int_0^\infty d\lambda \int_{-\infty}^{\infty} \omega_{10}(\xi, y) \cos \lambda(\xi - x)\, d\xi \tag{50}$$

The solution ψ_{11} is then of the following form:

$$\psi_{11} = \int_0^\infty Y_1(y) \cos \lambda x\, dx + \int_0^\infty Y_2(y) \sin \lambda x\, d\lambda \tag{51}$$

Substituting Eqs. (48), (50), and (51) into Eq. (40), we have

$$Y_i''(y) + \mu^2\lambda^2\, Y_i(y) = -H_i(y) \tag{52}$$

where $i = 1$ or 2,

$$Y_i'' = d^2Y_i(y)/dy^2$$

and

$$\left.\begin{aligned} H_1(y) &= -\frac{\omega_{10}(y)}{\pi}\frac{\sin(\lambda y \tan \delta_0)}{\lambda} \\ H_2(y) &= \frac{\omega_{10}(y)}{\pi}\frac{\cos(\lambda y \tan \delta_0)}{\lambda} \end{aligned}\right\} \tag{53}$$

The solution Y_i is

$$Y_i = \frac{1}{\lambda\mu}\int_0^y H_i(y) \sin \lambda\mu(y - \eta)\, d\eta \tag{54}$$

Finally, the solution ψ_{11} is

$$\psi_{11} = -\int_0^y \frac{\omega_{10}(\eta)}{\pi\mu}\, d\eta \int_0^\infty \frac{1}{\lambda^2} \sin \lambda(x - \eta \tan \delta_0) \times \sin \mu\lambda(y - \eta)\, d\lambda \quad (55)$$

Since we consider the region behind the curved shock only, Eq. (55) can be integrated with respect to λ, and we then have

$$\psi_{11}(x, y) = yW(0) - \int_0^y W(\eta)\, d\eta \quad (56)$$

where

$$dW(\eta)/d\eta = \omega_{10}(\eta) \quad (57)$$

It is evident that $\psi_{11}(x, 0) = 0$. For the second boundary condition of Eq. (40), we substitute Eqs. (56) and (41) into the second boundary condition

$$f_r(x) = \left[\frac{R_f}{b} + \frac{1 + R_f}{b} K_\omega\right] f(bx) - \frac{1 + R_f}{2} K_\omega f'(0)x \quad (58)$$

Substituting Eq. (58) into Eq. (42), we have

$$f(x) + \left[\frac{R_f}{b} + \frac{1 + R_f}{2b} K_\omega\right] f(bx) = Y(x) + \frac{1 + R_f}{2} K_\omega f'(0)x \quad (59)$$

Eq. (59) gives the functional relation of the basic disturbance function f. Since the vorticity function depends mainly on the conditions at the shock, it turns out that the vorticity function and the reflected function f_r are of similar form and that they can be combined together.† After the basic function f is determined, we then have

$$\psi_1 = -d_1[f(x - \mu y) + f_r(x + \mu y)] + \psi_{11} \quad (60)$$

where both f_r and ψ_{11} can be expressed in terms of f with the help of Eqs. (58), (56), and (48).

(VI) Strong Attached Shock—Subsonic Flow Behind the Curved Shock

When the strength of the shock is large, the flow behind the shock will be subsonic—i.e., $M_2 < 1$. Eq. (35) is then of the elliptical type.

By a similar procedure as in the case of weak shock, we write

$$\psi_1 = \psi_{10} + \psi_{11} \quad (61)$$

where ψ_{10} and ψ_{11} are now functions such that

$$\left.\begin{aligned} \mu^2(\partial^2\psi_{10}/\partial x^2) + (\partial^2\psi_{10}/\partial y^2) &= 0 \\ \psi_{10}(x, 0) &= -d_1 Y(x) \\ \frac{\partial\psi_{10}}{\partial y} &= -\frac{U_{a_1}}{V_{a_1}}(1 + K_\rho U_2^2)\frac{\partial\psi_{10}}{\partial x} \end{aligned}\right\} \quad (62)$$

at $y = x \tan \delta_0$, where $\mu^2 = 1 - M_2^2$ and

† This simplified relation was first pointed out to the author by Dr. F. W. Geiger, of Cornell Aeronautical Laboratory, Inc.

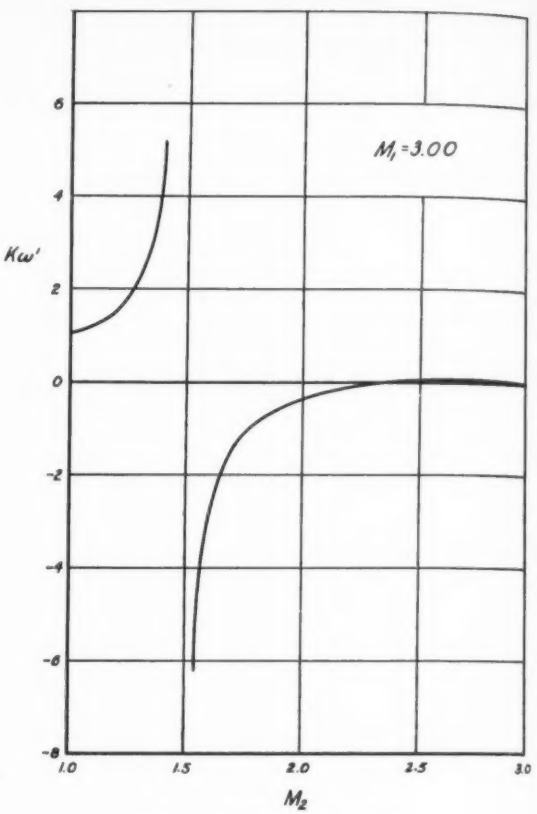

FIG. 4. Vorticity factor $K\omega'$.

$$\left.\begin{aligned} \mu^2(\partial^2\psi_{11}/\partial x^2) + (\partial^2\psi_{11}/\partial y^2) &= -\omega_{10}(x, y) \\ \psi_{11}(x, 0) &= 0 \\ \frac{\partial\psi_{10} + \psi_{11}}{\partial y} &= -\frac{U_{a_1}}{V_{a_1}}(1 + K_\rho U_2^2)\frac{\partial\psi_{10} + \psi_{11}}{\partial x} \end{aligned}\right\} \quad (63)$$

at $y = x \tan \delta_0$.

In order to solve Eq. (62), it is convenient to change the independent variables x and y into r and θ such that

$$r = \sqrt{x^2 + \mu^2 y^2}, \quad \theta = \tan^{-1}(\mu y/x) \quad (64)$$

Eq. (62) then becomes

$$\left.\begin{aligned} \frac{\partial^2\psi_{10}}{\partial r^2} + \frac{1}{r}\frac{\partial\psi_{10}}{\partial r} + \frac{1}{r^2}\frac{\partial^2\psi_{10}}{\partial\theta^2} &= 0 \\ \psi_{10}(r, 0) &= -d_1 Y(r) \\ K_r \frac{\partial\psi_{10}(r, \theta_{\delta_0})}{\partial r} &= K_\theta \frac{1}{r}\frac{\partial\psi_{10}(r, \theta_{\delta_0})}{\partial\theta} \end{aligned}\right\} \quad (65)$$

where

$$\theta_{\delta_0} = \tan^{-1}(\mu \tan \delta_0)$$

$$K_r = [\mu \sin \theta_{\delta_0} + (U_{a_1}/V_{a_1})(1 + K_\rho U_2^2) \cos \theta_{\delta_0}]$$

$$K_\theta = [(U_{a_1}/V_{a_1})(1 + K_\rho U_2^2) \sin \theta_{\delta_0} - \mu \cos \theta_{\delta_0}] \quad (66)$$

The solution of Eq. (65) is

$$\psi_{10} = -d_1 \sum_{n=0}^{\infty} r^n [A_n \cos n\theta + B_n \sin n\theta] \quad (67)$$

The coefficients A_n and B_n can be determined from the boundary conditions.

If we develop $Y(r)$ into power series, we have

$$Y(r) = \sum_{n=0}^{\infty} a_n r^n \quad (68)$$

The first boundary condition of Eq. (65) gives

$$A_n = a_n \quad (69)$$

The second boundary condition of Eq. (65) gives

$$B_n = a_n \frac{K_\theta \sin n\theta_{\delta_0} + K_r \cos n\theta_{\delta_0}}{K_\theta \cos n\theta_{\delta_0} - K_r \sin n\,\theta_{\delta_0}} = b_n \quad (70)$$

(say). Hence, the expression of ψ_{10} is

$$\psi_{10} = -d_1 \sum_{n=0}^{\infty} (x^2 + \mu^2 y^2)^{n/2} \times \left[a_n \cos\left(n \tan^{-1} \frac{\mu y}{x}\right) + b_n \sin\left(n \tan^{-1} \frac{\mu y}{x}\right)\right] \quad (71)$$

In order to solve Eq. (63), we must estimate the shape of the curved shock and the vorticity function $\omega_{10}(x, y)$, which is found as follows:

$$\omega_{10}(x, y) = K_\omega' d_1 \mu k_r \sum_{n=2}^{\infty} n(n-1) r_{\delta_0}^{n-2} [-a_n \sin (n-1)\theta_{\delta_0} + b_n \cos (n-1)\theta_{\delta_0}] = \omega_{10}(y) \quad (72)$$

when $x \geq y \cot \delta_0$ and $\omega_{10}(x, y) = 0$ when $x < y \cot \delta_0$ and

$$r_{\delta_0} = y\sqrt{\mu^2 + \cot^2 \delta_0} = y k_r \quad (73)$$

(say).

The solution of Eq. (63) with the boundary condition $\psi_{11}(x, 0) = 0$ is simply as follows:

$$\psi_{11}(x, y) = \frac{1}{4\pi\mu} \int_0^{\infty} \omega_{10}(\eta)\, d\eta \int_{\eta \cot \delta_0}^{\infty} \log \frac{(x-\xi)^2 + (y+\eta)^2}{(x-\xi)^2 + (y-\eta)^2} d\xi \quad (74)$$

In order to satisfy the boundary condition at the shock, we must modify the solution of ψ_{10} of Eq. (71) so that the last equation of Eqs. (63) is satisfied. We find that $A_n = a_n$ still holds true, but the following expression for B_n should be used:

$$B_n = b_n - \frac{C_{n-1}}{n k_r^{n-1}} = b_{n_1} \quad (75)$$

(say), where

$$\left.\begin{aligned} C_n &= -\left[k_{1n} + \frac{U_{\alpha_1}}{V_{\alpha_1}}(1 + K_\rho U_2^2)\, k_{2n}\right] \\ \frac{\partial \psi_{11}(y \cot \delta_0, y)}{\partial y} &= g_1(y) = \sum_{n=0}^{\infty} k_{1n}\, y^n \\ \frac{\partial \psi_{11}(y \cot \delta_0, y)}{\partial x} &= g_2(y) = \sum_{n=0}^{\infty} k_{2n} y^n \end{aligned}\right\} \quad (76)$$

Finally, we have

$$\psi_1 = -d_1 \sum_{n=0}^{\infty} r^n (a_n \cos n\theta + b_{n_1} \sin n\theta) + \psi_{11} \quad (77)$$

This is the first approximation to ψ_1. An iteration method can be used to obtain more accurate results.

(VII) Velocity and Pressure Formulas

A knowledge of the velocity and the pressure distribution over the surface of an aerodynamic body at high speed is of primary importance in the design of high-speed aircraft. In the present problem, it is advisable to show the difference between the results for rotational flow and those for the corresponding irrotational flow.

(a) *Velocity Distribution*

Let q be the resultant velocity at any point considered. In the region behind the attached curved shock, we have

$$q = \sqrt{(U_2 + u)^2 + v^2} = U_2 + u + \text{higher order terms} \quad (78)$$

Hence, the distribution of u may be used to represent the distribution of the whole velocity field.

(*1*) *The Weak Shock Case.*—From Eqs. (23), (24), (35), (48), and (60) we have, for the rotational flow behind the attached curved shock, the distribution of u as follows:†

$$\left(\frac{u}{U_2}\right)_{\text{rot.}} = +\frac{d_1}{\mu}\left(f'(x - \mu y) - R_f f'[b(x + \mu y)] + K_\omega \left[\frac{1 - M_2^2}{1 + (\gamma - 1)M_2^2}\right]\{f'[(\cot \delta_0 - \mu)y] - f'(0)\}\right) \quad (79)$$

The corresponding formula for irrotational flow is

$$(u/U_2)_{\text{irr.}} = +\frac{d_1}{\mu} Y'(x - \mu y) \quad (80)$$

The ratio of the velocity distributions of Eqs. (79) and (80) may be written as follows:

$$(u/U_2)_{\text{rot.}}/(u/U_2)_{\text{irr.}} = u_B + u_R + u_\omega \quad \text{(say)} \quad (81)$$

† This formula was first derived by Dr. F. W. Geiger when he carried out some numerical examples for the present theory, which will be published by Cornell Aeronautical Laboratory, Inc.

The first term

$$(u_B = f'(x - \mu y)/Y'(x - \mu y)$$

shows the variation of basic disturbance from the irrotational solution. If the reflection factor R_f approaches zero and the vorticity factor also approaches zero, u_B will approach unity, which represents the case when the shock strength is extremely weak.

The second term

$$u_R = -R_f \frac{f'[b(x + \mu y)]}{Y'(x - \mu y)} \tag{82}$$

shows the variation of reflected disturbance from the shock front. This term depends mainly on the reflection factor R_f. A typical curve for R_f at a given M_1 is shown in Fig. 3. It shows that, when the shock strength is large, this term is extremely important. Of course, this analysis breaks down when $R_f = \infty$, because at this point, according to the first order linearized theory, the reflecting disturbance itself satisfies the Rankine-Hugoniot relation; we cannot use it to balance the basic disturbance in order that the resultant velocity components satisfy the Rankine-Hugoniot relations. However, excluding the immediate neighborhood of $R_f = \infty$, this term will show the general behavior of the reflected disturbance.

Although the general functional form of the reflected disturbance is the same as that of the basic disturbance, there is a shift in phase between these two disturbances as is expected.

The third term gives the variation of velocity due to vorticity—i.e.,

$$u_\omega = K_\omega \frac{1 - M_2^2}{1 + (\gamma - 1)M_2^2} \frac{f'[(\cot \delta_0 - \mu)y] - f'(0)}{Y'(x - \mu y)} \tag{83}$$

On the surface of the ogive, y is small in our analysis; hence, this term u_ω is generally small there in comparison with the other two terms. The main effect of this term is to modify the functional form of f.

(*2*) *The Strong Shock Case.*—It is possible to derive a formula similar to Eq. (79) for the $(u/U_2)_{\text{rot.}}$ for the strong case. Since there is no corresponding solution for irrotational flow in this case, we are not going to write the formula down here for comparison. However, from the expression for ψ_1 [Eq. (77)], we see that the distribution of u/U_2 may also be divided into three parts: the basic disturbance that depends on the a_n's, the reflected disturbance that depends on the b_{n_1}'s and the vorticity term that is given by ψ_{11}.

(*b*) *Pressure Distribution*

By definition, the pressure coefficient is

$$C_p = (p - p_2)/(1/2)\rho_2 U_2^2 \tag{84}$$

for first-order linearized theory, we have

$$C_p = -(2u/U_2) - [2(S - S_1)/\gamma M_2^2 R] \tag{85}$$

The difference in pressure coefficient between the results for the rotational flow and those for the irrotational flow are twofold. The first is due to the difference in velocity distribution, and the second is due to the change of entropy $(S - S_1)$.

(VIII) Limitations of the Present Theory

From the above analysis, we see that there are two singular points at which the present theory breaks down.

The first point is that at which the reflection factor R_f equals infinity, which has been discussed in Section (VII).

The second point is that where $K\rho U_2^2 = -1$. At this point the change of stream function immediately behind the shock due to the change of x-wise velocity and that due to the change of density cancel each other. Hence, we cannot determine the vorticity terms.

These two singular points are simply mathematical defects of the first-order linearized theory. From numerical calculations it is found that both of them occur when $M_2 > 1$. Hence, it is suggested that, within the immediate neighborhood of these two points, the exact differential equation for the stream function should be used, and, since $M_2 > 1$, the method of characteristics can be used to solve the exact differential equation for the stream function numerically.

Excluding the immediate neighborhood of these two singular points, the first-order linearized theory will show the general behavior of the flow pattern behind the attached curved shock.

References

[1] Lin, C. C., and Rubinov, S. I., *On the Flow Behind Curved Shocks*, Jour. Math. and Physics, Vol. 27, No. 2, pp. 105–129, July, 1948.

[2] Sears, W. R., *The Linear Perturbation Theory for Rotational Flow*, Jour. Math. and Physics, Vol. 28, No. 4, pp. 268–271, July, 1950.

[3] Kaplan, C., *Effect of Compressibility at High Subsonic Velocities or the Lifting Force Acting on an Elliptic Cylinder*, N.A.C.A. T.N. No. 1118, 1946.

An Impulse-Momentum Method for Calculating Landing-Gear Impact Conditions in Unsymmetrical Landings*

ROBERT T. YNTEMA†

Langley Aeronautical Laboratory, N.A.C.A.

ABSTRACT

A brief review of the landing process is made, and the importance of the unsymmetrical landing condition is considered. A simple impulse-momentum method that takes account of approach conditions and airplane geometric and inertia characteristics is given for calculating landing-gear contact conditions for successive impacts in unsymmetrical landings. Calculated results for a large airplane are used to compare the severity of landing-gear impacts in unsymmetrical and symmetrical landings and to show the effects of such factors as sinking speed, wing lift, and side drift on impact severity in the unsymmetrical case. The importance of landing-gear location and configuration is also shown by a comparison of the contact conditions for two similar airplanes—one having a conventional tricycle arrangement of gears and the other having a quadricycle arrangement.

SYMBOLS

I_v = vertical landing-gear impulse, positive upward

I_d = drag impulse, positive aft

z_g = vertical height of the airplane c.g. above the ground, positive up

θ = angle of pitch measured between the fuselage reference axis and the ground plane

φ = angle of roll, measured between the spanwise reference axis and the ground plane

z = vertical velocity of any point on the airplane, positive upward

$\dot{\theta}$ = pitching velocity of the airplane, positive nose up looking forward

$\dot{\varphi}$ = rolling velocity of the airplane, positive clockwise

V_1 = vertical velocity for the first gear to impact in a landing, positive down (used only in figures, corresponds to $\dot{z}_{i_0}$)

V_2 = vertical velocity for the second gear to impact in a landing, positive down (used only in figures, corresponds to $\dot{z}_{i_f}$)

E = energy present for a particular gear at impact

M = total mass of the airplane

M_e = effective mass acting on a landing gear during an impact

I_{aa} = rolling moment of inertia of the airplane

I_{bb} = pitching moment of inertia of the airplane

K_L = wing lift factor, ratio of aerodynamic lift force to total airplane weight

K_s = ratio of side impulse to vertical impulse, defined by the average coefficient of lateral skidding friction between a tire and the runway

t = time

η_r = energy dissipation efficiency of a landing gear—determines rebound characteristics of the gear

$A_i, B_i, C_i, D_i, A_j, B_j$ = combined constants, moment arms about the c.g.

a_j, b_j, c_j = constants that define the location of a landing gear relative to the airplane c.g.

Subscripts

0 = initial conditions at the beginning of a particular landing impulse

t = terminal conditions at the end of a particular impulse, represents initial conditions for the free-body portion of the analysis

f = final conditions for the free-body motion, corresponds to initial conditions for the next impulse

g = the center of gravity of the airplane

i = the landing gear or gears whose contact initiates a given stage of the motion

j = the landing gear whose contact terminates the free-body motion, j becomes i in the next impulse solution

INTRODUCTION

IN RECENT YEARS, the increased size and landing speed of airplanes and the relatively large weight penalty associated with landing gears have stimulated considerable interest in landing problems and in associated design requirements. Although considerable effort has been directed toward the solution of some of these problems, significant gaps still exist in the general knowledge pertaining to the landing phenomenon. The present paper touches briefly on the state of knowledge concerning various aspects of the landing process and has the particular purpose of evaluating the importance of unsymmetrical landings from an impact standpoint. The remaining introductory material discusses these aims further and is, for convenience, divided into three sections. The first of these sections reviews the landing process, the second discusses the design requirement for the unsymmetrical landing condition, and the third indicates the significance of the unsymmetrical landing by means of a simplified example. The example furnishes the basis for a more complete subsequent analysis permitting consideration of additional factors involved in landing.

Presented at the Structures Session, Nineteenth Annual Meeting, I.A.S., New York, January 29–February 1, 1951. Revised and received April 17, 1952.

*The author is indebted to members of the Dynamic Loads Division and particularly to Benjamin Milwitzky and John Houbolt, who rendered valuable assistance in the preparation of this paper.

† Aeronautical Research Scientist.

The Landing Process

A normal landing of an airplane may logically be divided into three parts: (1) the approach during which airplane motion is largely a function of pilot control; (2) the transition from an air-borne to a ground-borne condition, during which the vertical motion of the airplane is rapidly decelerated and pilot control has little immediate effect, particularly in severe landings; and (3) the ground run, during which the pilot again regains control and maneuvers the airplane to a stopping point.

During the approach, the pilot attempts to make a symmetrical landing with a low vertical and side velocity. Pilot error and unpredictable aerodynamic effects such as gusts, and even unusual conditions such as forced landings may enter the picture, however, and tend to prevent this ideal type of landing. Since these situations are next to impossible to predict analytically, it appears that limits and ranges for airplane velocities and attitudes at initial touchdown are best determined from actual situations—that is, from statistical data. Unfortunately, only meager data concerning these touchdown conditions are currently available.

During the touchdown or transition period, large ground reactions build up rapidly and tend to make this period the most critical part of a landing. The action of these ground loads on the structure is more amenable to analytical treatment and has perhaps received the most attention by investigators. Most of the investigations, however, have been largely concerned with some particular aspect of the problem such as the determination of a component of the ground reaction, consideration of landing-gear behavior, or the evaluation of dynamic structural effects on the assumption that landing-gear forcing functions are known. It appears that little consideration has been given the tie-in between the actual approach conditions and the loads that develop in the structure. As a consequence, a rational link between the approach conditions and the design impact conditions is missing, particularly for the unsymmetrical condition. It is with this link that the present paper is largely concerned.

After the transition period, airplane motions are largely a function of pilot action and the loads imposed on the airplane structure become those associated with braking, turning, and surface irregularities. During this period, unstable oscillations such as shimmy may also arise. Of the problems associated with the runout phase of landing, the shimmy problem has perhaps received the most attention, but this attention has not always been realistic. There is still much to be desired with regard to this and other problems.

Design Requirements for Unsymmetrical Landings

Since a unified knowledge of the landing process and the associated problems has not been available, current design requirements are based largely on experience rather than on statistical data or rational analytical treatments. Thus they include hidden factors that tend to compensate for the combined effect of many conditions not rationally considered in detail. As an example, the present requirements specify the same impact velocities and landing-gear reactions in unsymmetrical as in symmetrical landings. Experience and calculations indicate, however, that landing-gear impacts can be appreciably more severe in the unsymmetrical case. On the other hand, limited experimental evidence indicates that the design sinking speed is considerably higher than the maximum descent velocity encountered in normal landings of many aircraft.[2] In other words, a hidden factor that covers the ignorance associated with unsymmetrical landings seems to be included in the sinking speed. While the present requirements generally permit the design of reasonably satisfactory landing gears, at least for aircraft similar to those that have given satisfactory service, they may be inadequate or perhaps unnecessarily stringent for gear design on new types of aircraft. Unfortunately, the present lack of data regarding approach conditions during landing prohibits the design of landing gears on a completely rational basis.

Consideration of Unsymmetrical Impacts

The present paper is concerned with the severity of initial and subsequent impacts in unsymmetrical landings as compared with the severity of landing-gear impacts in symmetrical landings. The treatment considers as the criterion for the severity of impacts the impact velocity and energy rather than the maximum loads or the detailed variation of the loads developed during the impact. In order to assess rapidly the effect that an unsymmetrical landing attitude might

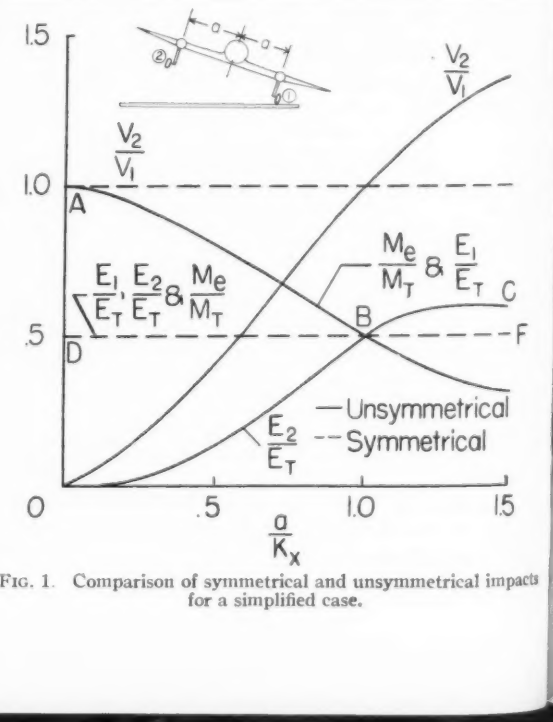

FIG. 1. Comparison of symmetrical and unsymmetrical impacts for a simplified case.

have on the severity of landing-gear impacts, a brief study of the simplified two degree of freedom system indicated by the airplane sketch in Fig. 1 was made. The simplified studies provided the motivations for the more complete subsequent analysis, which takes into account additional factors involved in landing. In the simplified case, the airplane has freedom in roll and in vertical translation and is assumed to impact on one of the main gears. It is further assumed that the landing gears are 100 per cent efficient in dissipating energy, that airplane weight is exactly balanced by lift, that there are no side or drag loads, and that there is no structural flexibility or other complicating effects. The impact velocity and energy for initial and second impacts is determined using simple impulse-momentum relationships. This approach is used because it requires no knowledge of the load time history or of the maximum load factor developed by the gear. While the simplified system does not represent an actual landing, it can be used to point out some interesting and not commonly considered effects.

Nondimensional results for the simplified case are presented in Fig. 1, where a comparison is made of the effect that landing-gear position can have on the severity of landing-gear impacts in unsymmetrical and in symmetrical landings. The significant parameter of this plot, the abscissa, is the ratio of the outboard distance of each landing gear a to the radius of gyration of the airplane in roll K_x; at the value of one, the landing gears are thus located at the radius of gyration position. The ordinates are V_2/V_1, the ratio of the vertical velocity of the second gear to contact to the vertical velocity of the first gear to contact; M_e/M_T the ratio of the effective mass (the portion of the total mass which may be considered to act on a gear during an impact) to the total mass and in this case is the same for either main gear; and E_1/E_T and E_2/E_T, the ratios of the energies absorbed, respectively, by the first and second gears to contact to the total initial energy of the airplane. The dashed straight lines show results for the symmetrical case, while the solid curves represent the unsymmetrical case. The curves show a number of effects, two of which are particularly significant: (1) The contact velocity for the second impact in an unsymmetrical landing may be appreciably larger than the initial descent velocity of the airplane if the landing gears are located outboard of the rolling radius of gyration of the airplane—that is, $a/K_x > 1$; (2) one of the impacts in an unsymmetrical landing must be at least as severe as, and will usually be more severe than, each landing-gear impact in a symmetrical landing (compare energy curve ABC and line DF). The preceding observations are even more significant when it is realized that such factors as unbalanced wing lift and side drift could result in impacts of much greater severity than is indicated by the simplified results. Other preliminary studies have indicated that unsymmetrical landings may be especially important for certain types of unconventional landing-gear configurations.

In the present paper, this simplified impulse-momentum approach has been broadened and improved to permit consideration of additional factors such as freedom to pitch, side drift, reduced wing lift or the action of gravity, angular velocities and attitude angles at initial contact, and landing-gear energy dissipation efficiency. In this analysis the airplane is again considered a rigid body, since flexibility is expected to have little effect on the free-body motions of the airplane and on shock-strut behavior. Adequate consideration of flexibility effects would, of course, greatly complicate the analysis. In the interest of brevity, mathematical detail has been kept at a minimum in the present paper, although a more detailed development has been made. The method is applicable to airplanes with any landing-gear configuration and permits determination of contact conditions for successive impacts in unsymmetrical landings in which landing gear impacts either do not overlap appreciably or occur simultaneously. Unfortunately, the extended analysis is not readily adaptable to generalized trend studies of the type made for the simplified case. Some applications of the method to specific airplanes have been made, however, and these results are presented.

Analysis

The analysis given in the present paper has two basic objectives: (1) the determination of the contact velocity for landing-gear impacts that occur subsequent to initial touchdown and (2) the determination of the effective mass acting at a landing gear during a landing-gear impact throughout which the resultant ground force does not necessarily maintain a fixed direction. For convenience, the analysis is divided into three parts entitled Impulse, Free-Body Motion, and Effective Mass. In each of these parts, general equations applicable to landings in which any combination of gears contact the ground simultaneously are first written; these equations are then adapted to the particular case of an unsymmetrical landing in which initial contact occurs on one gear.

Impulse

The impulse analysis considers changes in airplane linear and angular velocities resulting from the initial landing impact. These changes are determined from impulse momentum relationships that assume that the time duration of vertical, drag, and side impulses acting on a landing gear during an impact is short and, thus, that the attitude of the airplane remains substantially fixed during the impulse of these ground forces. No knowledge of the vertical force time history or of the maximum load factor developed by the gear is required in the solution of the impulse-momentum equations. The vertical impulse is included in these relations as an

unknown, the side impulse (associated with a drift or yawed landing) is assumed to be related to the vertical impulse by some average coefficient of friction, and the drag impulse is taken equal to the change in angular momentum of the wheel or wheels attached to a landing gear as they are spun up to ground speed.

Immediately following impact, the contacting gear is assumed to rebound with a vertical velocity that is a function of the impact velocity and the energy dissipation efficiency of the landing gear. Since no time delay is considered in the impulse analysis, the effect of reduced wing lift (unbalanced airplane weight) on the landing-gear impulses and therefore on the linear and angular velocities of the airplane at rebound must be neglected. This error tends to make results of the impulse solution somewhat unconservative in cases where the wing lift is less than the weight of the airplane.

General Equations.—The pertinent impulse equations for an airplane making an unsymmetrical landing in which n landing gears contact the runway simultaneously may be written as follows:

For the vertical motion,

$$\sum_{i}^{n} I_v = M(\dot{z}_{gt} - \dot{z}_{g0}) \tag{1}$$

For the pitching motion,

$$I_{bb}(\dot{\theta}_t - \dot{\theta}_0) = \sum_{i}^{n} I_{v_i} A_i - \sum_{i}^{n} I_{d_i} C_i \tag{2}$$

For the rolling motion,

$$I_{aa}(\dot{\varphi}_t - \dot{\varphi}_0) = \sum_{i}^{n} I_{v_i} B_i + K_s \sum_{i}^{n} I_{v_i} D_i \tag{3}$$

where the subscript i denotes any of the n landing gears making simultaneous contact; the subscripts 0 and t refer, respectively, to conditions at initial contact and at rebound; and A_i, B_i, C_i, and D_i are appropriate moment arms about the airplane center of gravity for the landing-gear impulses. Since these three equations contain $n + 3$ unknowns—namely, the three velocities $\dot{z}_{gt}$, $\dot{\theta}_t$, and $\dot{\varphi}_t$ and the n vertical landing-gear impulses—they are insufficient in number to permit solution. Additional equations may, however, be written for the kinematic relationship that must exist between the vertical velocity of rebound of each gear and the vertical, pitching, and rolling velocities of the airplane. Thus, for each gear that contacts simultaneously during a landing impact, the following relationship must be true at rebound:

$$\dot{z}_{gt} + A_i\dot{\theta}_t - B_i\dot{\varphi}_t = \dot{z}_{it} \tag{4}$$

where $\dot{z}_{it}$ is the rebound velocity of each landing gear i, which may be computed from the known initial velocities by the following equation:

$$\dot{z}_{it} = \dot{z}_{i0}\sqrt{1 - \eta_r} = (\dot{z}_{g0} + A_i\dot{\theta}_0 - B_i\dot{\varphi}_0)\sqrt{1 - \eta_r} \tag{5}$$

In this equation η_r is the energy dissipation efficiency of the landing gear which can be determined from drop test data or estimated from the energy dissipation characteristics of similar gears. For most gears a value of 80–96 per cent may be used.

Eqs. (1)–(4) now form a set of $(n + 3)$ equations which in any particular case may be solved simultaneously to determine the velocities of the airplane at the end of the impulse and, if desired, the vertical impulse acting at each of the gears making simultaneous contact.

One Wheel Landing.—For the particular case of an unsymmetrical landing on any one gear, say m, Eqs. (1)–(4) may be reduced to the following set:

$$I_{bb}(\dot{\theta}_t - \dot{\theta}_0) = M(\dot{z}_{gt} - \dot{z}_{g0})A_m - I_{d_m}C_m \tag{6}$$

$$I_{aa}(\dot{\varphi}_t - \dot{\varphi}_0) = M(\dot{z}_{gt} - \dot{z}_{g0})B_m - K_sM(\dot{z}_{gt} - \dot{z}_{g0})D_m \tag{7}$$

$$\dot{z}_{gt} + A_m\dot{\theta}_t - B_m\dot{\varphi}_t = \dot{z}_{mt} \tag{8}$$

Simultaneous solution of Eqs. (6)–(8) yields the vertical and angular velocities of the airplane $\dot{z}_{gt}$, $\dot{\theta}_t$, and $\dot{\varphi}_t$ immediately following a landing impact on any gear m.

Free-Body Motion

The free-body motion analysis considers changes in airplane motion and attitude during the interval between rebound and the next impact. Since the impulse of the ground forces is assumed to occur instantaneously, the interval actually begins immediately following a landing-gear impact. During this interval the airplane is considered a free body under the action of a constant gravitational and wing lift force, and the translational and angular velocities and the attitude of the airplane just before the next impact are determined. Aerodynamic moments are neglected in the analysis. Since these damping moments generally tend to reduce the angular velocities of the airplane, the free-body motion analysis is somewhat conservative and would be expected to yield somewhat higher second-gear contact velocities than actually occur. In landings with wing lift less than airplane weight, however, the previously mentioned unconservatism of results of the impulse analysis tends to balance this conservatism. A limited evaluation of some of these effects is presented in reference 2.

The free-body motion equations defining the vertical velocity, the height of the airplane center of gravity, and the pitching and rolling attitude of the airplane at the instant the next impact begins may be written, respectively, as follows:

$$\dot{z}_{gf} = \dot{z}_{gt} - gt_f(1 - K_L) \tag{9}$$

$$z_{gf} = z_{g0} - \dot{z}_{gt}t_f - (g/2)t_f^2(1 - K_L) \tag{10}$$

$$\theta_f = \theta_0 + \dot{\theta}_t t_f \tag{11}$$

$$\varphi_f = \varphi_0 + \dot{\varphi}_t t_f \tag{12}$$

in which the angular velocities of the airplane ($\dot{\theta}_t$ and $\dot{\varphi}_t$) are considered constant during the free-body

motion, since aerodynamic moments are neglected. In these equations, $\dot{z}_{0f}$, z_{0f}, θ_f, φ_f, and the duration of free-body motion t_f are unknown conditions at the beginning of the next impact which are to be determined. A fifth equation defining the height of the airplane center of gravity above the ground in terms of airplane geometry and attitude at the instant of contact on landing gear j, assumed to be the next gear to contact, may also be written as follows:

$$z_{0f} = c_j - a_j\theta_f + b_j\varphi_f \tag{13}$$

where a_j, b_j, and c_j are distances defining the location of the point of contact of gear j relative to the airplane center of gravity.

Eqs. (9)–(13) may now be solved simultaneously to obtain the time duration of the free-body motion, t_f, in terms of the known conditions at the beginning and the computed conditions at the end of the preceding impulse. With the value of t_f obtained, the vertical velocity, the attitude, and the height of the airplane may be determined from Eqs. (9)–(12). With $\dot{z}_{0f}$ now known and since $\dot{\theta}$ and $\dot{\varphi}$ are assumed not to change during the free-body motion, the contact velocity for landing gear j may be computed by means of the following equation:

$$\dot{z}_{jf} = \dot{z}_{0f} + A_j\dot{\theta}_t - B_j\dot{\varphi}_t \tag{14}$$

If the computed airplane attitude angles following free-body motion indicate that gear j was not the next to contact, the computation must be repeated for the landing gear that does actually contact next. Results of the preceding impulse solution, however, usually give a good indication of which gear will contact next.

Effective Mass

The effective mass analysis is concerned with the determination of the equivalent or effective mass acting on a landing gear during a landing impact in which three independently varying components of ground force act on the gear. Formulas for effective mass are derived on the basis of equal impulse and energy rather than equal instantaneous accelerations as are most conventional formulas.[3] This approach does not require the assumption that the resultant ground force maintains a fixed direction throughout the impact, as is necessary in the acceleration approach. Thus, the present method provides a convenient means of obtaining a mean value for the effective mass acting during an impact which is useful in simulating or calculating the severity of the impact.

The vertical impulse acting on the gear, as obtained in the impulse solution, may also be expressed in terms of the change in vertical velocity of the landing gear and a fictitious effective mass M_{ei} which can be considered to act on the gear—that is,

$$I_{vi} = M_{ei}(\dot{z}_{it} - \dot{z}_{i0}) \tag{15}$$

Solving for M_{ei} gives

$$M_{ei} = I_{vi}/(\dot{z}_{it} - \dot{z}_{i0}) \tag{16}$$

The results of the impulse solution can be used in this equation to obtain the effective mass desired. With this effective mass and the impact velocity, the kinetic energy of each landing gear at contact may be computed by means of well-known formulas for kinetic energy.

In cases where the resultant ground reaction does not maintain a fixed direction during a landing-gear impact, the effective mass defined by Eq. (16) is an average value that satisfies overall impulse and energy requirements for the impact; in cases where the ground reaction is fixed in direction, the effective mass obtained satisfies instantaneous acceleration requirements as well.

It should be noted that aerodynamic damping tends to increase the vertical impulse I_v on gear i and therefore tends to increase the effective mass acting on this gear. Since this effect is not included in the foregoing impulse analysis, the effective mass determined from such results will be somewhat smaller than if damping effects had been considered. Flexibility can also influence the effective mass, but in general its effect on the average value of this mass during an impact is probably small.

Presentation and Discussion of Results

Impact Conditions for Main Landing Gears

The method outlined in the analysis section has been used to calculate values of impact velocity and effective mass for the main landing gears of a twin-engined cargo airplane in unsymmetrical landings. The outboard distance from the airplane centerline to each main landing gear is about one and one-tenth times the rolling radius of gyration of the airplane, and the energy dissipation efficiency of each gear was taken as 80 per cent. In all of the calculations the airplane was assumed to be pitched 3° upward and rolled 7° to the left at initial contact on the left main gear, and the angular velocities of the airplane at initial touchdown were assumed to be zero. These initial conditions resulted in the second impact occurring on the right main gear for each different wing lift and sinking speed treated. Impact energies, which include the kinetic energy based on the vertical impact velocity and the effective mass and the potential energy based on the unbalanced effective weight $[M_e g(1 - K_L)]$ and an assumed travel (strut compression and tire deflection) of 1 ft., are also computed for each landing-gear impact. In all cases the potential energy was found to be small in comparison with the kinetic energy.

The impact velocities and energies computed for landings in which the side-drift velocity of the airplane at initial touchdown was assumed to be zero are shown

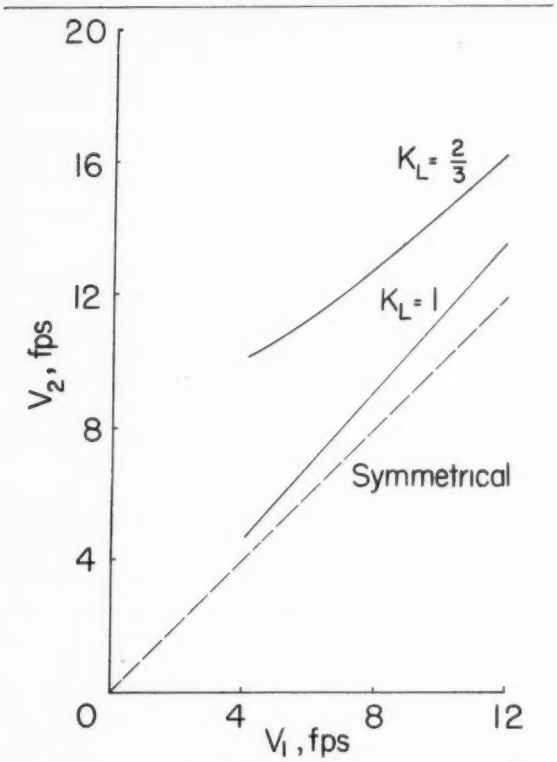

FIG. 2. Contact velocities V_1 and V_2 for first and second impacts in unsymmetrical landings. (First impact on one main gear; second impact on opposite main gear.)

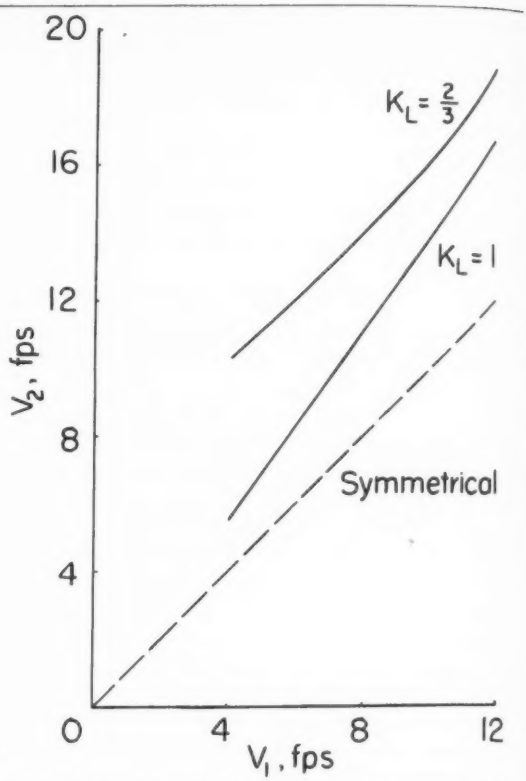

FIG. 4. Contact velocities V_1 and V_2 for first and second impacts in unsymmetrical landings with side drift. (First impact on one main gear; second impact on opposite main gear.)

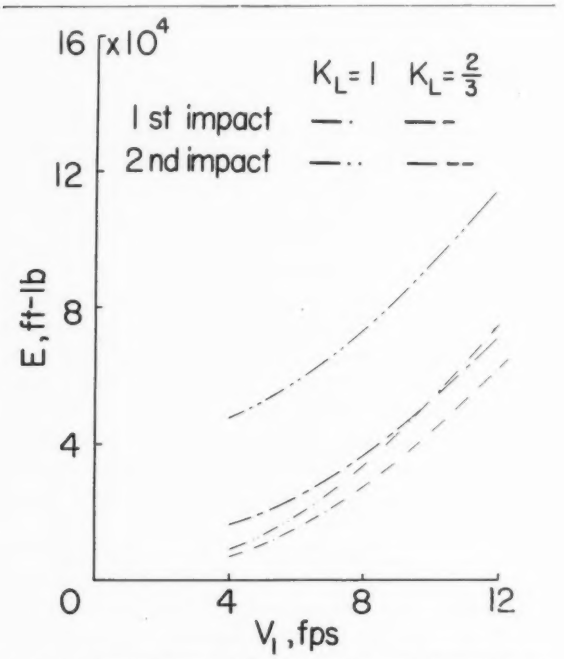

FIG. 3. Impact energy E for first and second impacts in unsymmetrical landings as a function of initial contact velocity V_1. (First impact on one main gear; second impact on opposite main gear.)

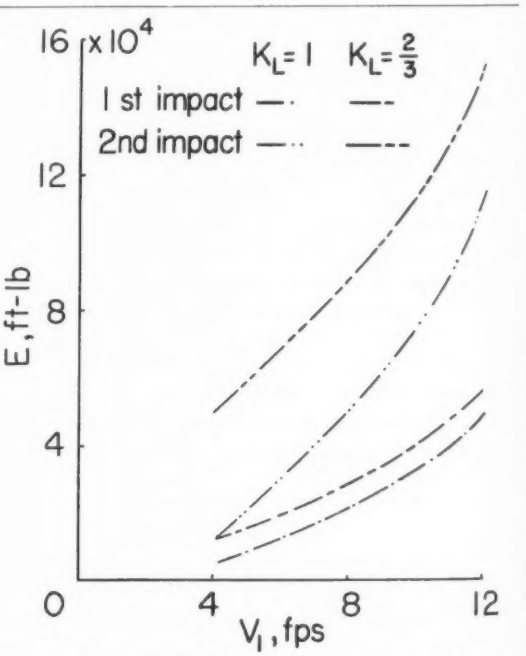

FIG. 5. Impact energy E for first and second impacts in unsymmetrical landings with side drift as a function of initial contact velocity V_1. (First impact on one main gear; second impact on opposite main gear.)

for full-wing lift and for two-thirds full-wing lift in Figs. 2 and 3. These wing-lift values correspond, respectively, to gravitational accelerations of zero and $^1/_3g$ acting during the impact. The vertical velocity for first impacts in the cases considered is, of course, the same as the descent velocity of the airplane at initial contact. The results presented show that, for the airplane under consideration, the vertical velocity for second impacts can be greater than the contact velocity for the first impact. In cases where all the weight of the airplane is balanced by wing lift ($K_L = 1$), the increase in velocity for second impacts may be largely attributed to the outboard location of the main gears relative to the radius of gyration of the airplane in roll. Reducing the wing lift tends to increase the impact velocity for second impacts still more; these effects appear to be more pronounced for landings with lower sinking speeds.

The variation of impact energy with vertical velocity at initial contact for first and second impacts in unsymmetrical landings is shown in Fig. 3. The curves presented show that the energy that must be absorbed by the second gear to contact in an unsymmetrical landing can be considerably greater than the energy to be absorbed by the gear making initial contact. The energy computed for each gear when symmetrical landings were considered was found to be practically the same as the energy for the first impact in the unsymmetrical case. If the main gears had been located inboard of the rolling radius of gyration of the airplane, the first impact in an unsymmetrical landing would be more severe than each landing-gear impact in a symmetrical landing with the same rate of descent.

It is of interest to consider what effect a side-drift velocity or yawed attitude of the airplane at initial contact might have on landing-gear impact conditions such as those presented in Figs. 2 and 3. To show this effect, the results shown in Figs. 4 and 5 were calculated for initial conditions identical to those used in obtaining the results presented in Figs. 2 and 3, with the exception that the airplane was assumed to be drifting to the right when initial contact occurs on the left main gear. In these computations, the side impulse on the first gear to contact was taken as six-tenths times the vertical impulse, and it was assumed that the lateral velocity of the airplane was zero when the second gear to contact touched down. The 0.6 ratio between the side and vertical impulse corresponds to a fairly large yaw angle on the order of 15° for conventional airplane tires (less for high-pressure tires).

Comparison of the results presented in Figs. 2 and 4 shows that the vertical velocity for second impacts in unsymmetrical landings with side drift can be appreciably higher than the contact velocity for second impacts in similar landings without side drift.

The effect of side drift on impact severity is even more striking when the impact energies given in Fig. 5 are compared with the results given in Fig. 3. Such a comparison shows that increases in impact energy as large as 50 per cent may result from side draft of the airplane just prior to initial touchdown. It is of interest to note that in most landings with initial side drift the airplane would probably also be drifting laterally when the second impact occurs. This condition will result in a larger effective mass acting during the second impact, and therefore the gear would have to absorb even more energy than in the cases considered.

If the airplane had been drifting to the left instead of to the right at initial contact on the left gear, the vertical veocity for second impacts would have been reduced rather than increased. In such a case, however, the effective mass acting during the first impact would be considerably larger than in the present case or than in a landing without side drift, and therefore the impact energy would be larger for the first impact. Thus, it is evident that an unsymmetrical landing with appreciable side drift will usually result in impacts of greater severity than those in an unsymmetrical landing without side drift or in a symmetrical landing.

Impact Conditions for Auxiliary Landing Gears

Results have also been computed for landings of an airplane in which the initial attitude was such that second impacts occur on an auxiliary gear. Two similar airplanes having the same inertia characteristics and the same location of the main gears are considered. One of the airplanes has a conventional tricycle arrangement of landing gears, while the other has a quadricycle arrangement. The attitude of the airplanes at initial contact was selected in such a manner that first impacts occurred on the left main gear and second impacts occurred on the nose gear of the tricycle and the right front gear of the quadricycle.

For the case of a positive pitch angle of 2.5° and a roll angle of 9° at initial touchdown, the impact velocity and energy for the nose gear of the tricycle arrangement are compared with similar results for a forward gear of the quadricycle arrangement in Figs. 6 and 7. These results show that a forward gear of the quadricycle arrangement can be subjected to impacts of far greater severity than is the nose gear of a conventional tricycle arrangement. Each of the forward gears must therefore have a larger energy capacity and greater strength than the nose gear in a conventional arrangement. The usefulness of the analysis presented is in part suggested by this example. In this case, the result suggests that there may be an appreciable weight penalty associated with the use of a quadricycle arrangement of landing gears.

The results presented in the preceding example are for a particular landing attitude that perhaps is not too common for large airplanes. Other computations for landings in which the initial roll and pitch angles were assumed to be considerably smaller show the same effects, however. For example, reducing the roll angle

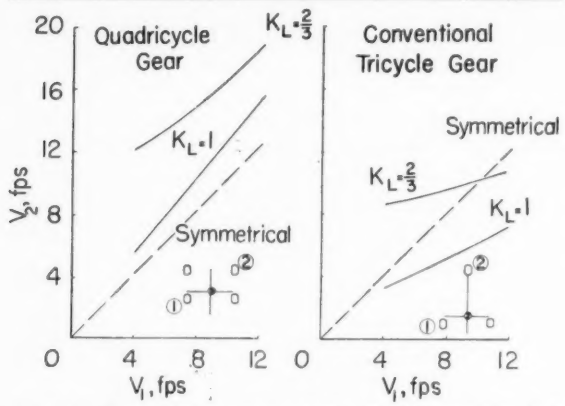

FIG. 6. Front-wheel contact velocity V_2 for unsymmetrical landings on one rear gear as a function of initial contact velocity V_1.

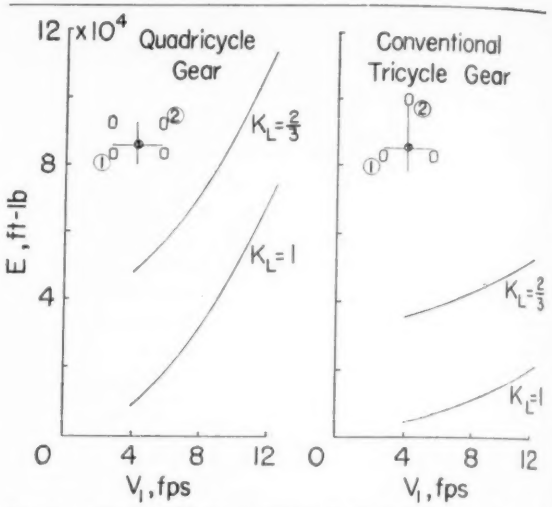

FIG. 7. Front-wheel impact energy E for unsymmetrical landings on one rear gear as a function of the initial contact velocity V_1.

from 9° to 5° for a landing of the quadricycle airplane in which the descent velocity was 12 ft. per sec. reduces the vertical velocity for second impacts only about $^1/_2$ ft. per sec.

It is to be noted that side-drift or angular velocities at initial contact can increase the severity of subsequent impacts for forward gears of the quadricycle, while, save for pitching velocities, they can have little effect on nose gear impacts of the tricycle arrangement. In general, these additional factors tend to widen the range of initial attitudes which will result in second impacts on a forward gear of the quadricycle arrangement. It may be noted that the forward gears of the quadricycle may also be subject to severe initial impacts.

Concluding Remarks

The present paper presents an impulse momentum method that permits the calculation of landing-gear contact conditions in unsymmetrical landings if the approach conditions at initial contact are known. Neglect of flexibility effects is not considered deleterious, since in many cases these effects have little influence on the free-body motions of the airplane and on landing-gear behavior, although they may have a significant effect on the internal stresses developed in the gear and supporting structure. Neglect of aerodynamic damping (particularly damping in roll) in the present analysis tends to make the results somewhat conservative, particularly in landings with wing lift nearly equal to airplane weight. A more detailed analysis, including variable aerodynamic effects and flexibility, would, of course, be desirable but is probably not warranted at the present time because of the lack of data regarding the magnitude of approach conditions likely to be encountered in service operations. Even without adequate information regarding these approach conditions, however, the method presented provides a basis for assessing the effects of airplane characteristics and operating conditions on impact severity and may be used to evaluate the relative merits of various landing-gear locations and configurations from the standpoint of impact severity. For the cases that were presented as examples, the following effects were noted.

(a) Landing-gear location is an important factor in determining the strength and energy requirements for landing gears.

(b) Contact velocities for second impacts in unsymmetrical landings can be appreciably higher than the sinking speed of the airplane at initial touchdown.

(c) The impact energy for either the first or second impact in an unsymmetrical landing will usually be greater than the energy for each gear in a symmetrical landing at the same sinking speed.

(d) Reducing the wing lift that acts during a landing tends to increase the contact velocity for second impacts in unsymmetrical landings.

(e) Side drift of the airplane at initial contact can result in an appreciable increase in the severity of either the initial or second impact in an unsymmetrical landing.

(f) In a quadricycle configuration, each of the forward gears is likely to be subjected to more severe impacts than the single nose gear in a conventional tricycle arrangement.

References

[1] Hootman, J. A., and Jones, A. R., *Results of Landing Tests of Various Airplanes*, N.A.C.A. T.N. No. 863, September, 1942.

[2] Yntema, Robert T., and Milwitzky, Benjamin, *An Impulse Momentum Method for Calculating Landing-Gear Contact Conditions in Eccentric Landings*, N.A.C.A. T.N. No. 2596, January, 1952.

[3] Walker, P. B., *Tricycle Undercarriage Design*, Aircraft Engineering, June, 1940.

[4] Prescott, J., *Mechanics of Particles and Rigid Bodies;* Longmans, Green & Company, London, New York, Bombay, and Calcutta, 1913.

The Subsonic Calculation of Circulatory Spanwise Loadings for Oscillating Airfoils by Lifting-Line Techniques

M. A. DENGLER* AND MARTIN GOLAND†

Midwest Research Institute

SUMMARY

A theoretical model is proposed to permit the convenient calculation of subsonic circulatory spanwise loadings on oscillating finite-span airfoils. The basis for the model is a lifting-line construction which represents a fairly direct extension of the Weissinger steady-state model to the oscillating case. It is shown how the present techniques permit treatment of swept wings with the same convenience as is normally encountered with straight wings.

To evaluate the performance of the model, a study is made of the spanwise loadings on an upswept rectangular wing of aspect ratio 5, oscillating with reduced frequency $^1/_3$ in six different spanwise-symmetrical modes of motion; the results of calculations are reported on the basis of the present model and on the basis of two prior theoretical treatments. An unswept wing is dealt with in the evaluation, since a theoretical background is available only for this class of oscillating wings. Calculations are also reported for a rectangular wing of aspect ratio 5 and 45° sweepback, undergoing the same type motions as the upswept wing.

The considerations of this paper lead to certain general observations regarding the character of the Prandtl, Cicala, and Weissinger wing theories. An effort is made to show how the present ideas stand in relation to current literature on the subject.

Finally, recommendations for further study are made, aimed toward development of a practical design-office procedure for the aerodynamic treatment of oscillating wings of general plan form.

INTRODUCTION

THE PRESENT PAPER CONSTITUTES a revision of an original draft, presented at the Twentieth Annual Meeting of the I.A.S. and circulated as Sherman M. Fairchild Publication Fund Preprint No. 347. It is hoped that this new version reflects the many helpful comments of the discussers of the earlier paper; in particular, the authors are indebted to A. H. Flax and H. R. Lawrence, both of Cornell Aeronautical Laboratory, Inc., for their criticisms and suggestions. It is also possible for the authors to include in this draft certain data and ideas not available at the time of the original writing.

The problem dealt with is that of calculating the circulatory loading on an oscillating finite-span airfoil in subsonic flow. Since subsonic compressibility corrections are thoroughly explored in the literature, the immediate considerations can be restricted to the incompressible flow case. As its principal objective, the present study is aimed toward the derivation of a design-office procedure adequate for treating the aerodynamics of oscillating wings with strong sweep. If a design-office technique is to be deduced, it is obvious that simplicity and calculational convenience must be stressed.

For the unswept airfoil in steady-state flow, the classic Prandtl lifting-line theory reduces the airfoil to an amazingly simple aerodynamic model. In place of dealing with the wing as a lifting surface, requiring the solution of a partial integrodifferential equation in both the chordwise and spanwise coordinates, Prandtl skilfully approximates the solution in terms of an integrodifferential equation in the spanwise coordinate only. The physical basis for the Prandtl approximation is discussed later in this paper, and, from a slightly different point of view, is considered in detail by Reissner,[7] Lawrence,[8] and Flax and Lawrence.[9] Dealing with the oscillating unswept airfoil, Cicala[2] showed how the Prandtl reasoning could be directly extended to the unsteady flow problem. For the solution of practical problems and subject to the restriction of dealing with airfoils with not-too-small aspect ratios, both the Prandtl and Cicala techniques afford enormous computational advantage over any attempt to deal with the problem on a more rigorous lifting surface basis.

For reasons to be made clear later, Weissinger[1] concluded that the Prandtl approach is inapplicable for the treatment of sharply swept wings. However, by adopting a new aerodynamic model, he was able to retain the essential computational advantages of the Prandtl method while meeting many of the important requirements of swept-wing theory. (For a critical discussion of the Weissinger model, see references 7, 8, and 9, and see the discussion later in this paper.) Weissinger's work is restricted to the steady-state problem, and the main objective of the present study is to extend his ideas to the oscillating airfoil case.

It should be particularly noted that all of the theories considered in this paper suffer from one major disadvantage: Since the objective of each is to reduce the lifting surface problem to a single integrodifferential in one variable, they are forced to concentrate attention on the *lift* distribution over the span of the airfoil;

Based on a paper presented at the Aeroelasticity Session, Twentieth Annual Meeting, I.A.S., New York, January 28–February 1, 1952.

* Research Engineer.

† Associate Director for Engineering.

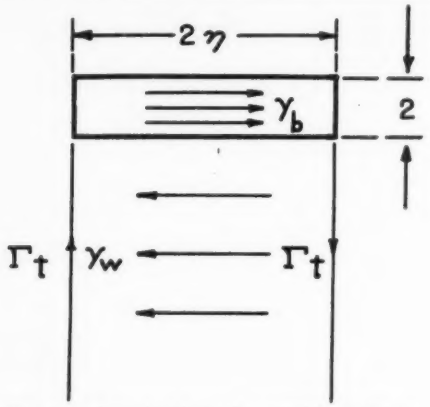

FIG. 1a. A typical horseshoe vorticity pattern.

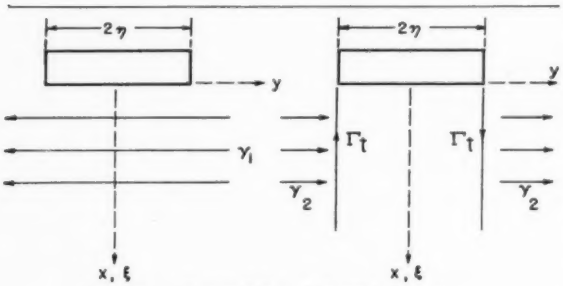

FIG. 1b. Composition of the Fig. 1a wake.

it must be expected that their consideration of the airfoil pitching moment distribution is on a less precise basis. A thorough discussion of this question is given by Reissner.[7] It should also be noted that the present study deals only with circulatory aerodynamic forces; finite-span corrections for the apparent mass terms that enter the unsteady flow problem are not considered.

THE BASIC APPROACH USED IN ESTABLISHING THE CHARACTERISTICS OF THE THEORETICAL WING MODEL

In connection with the general methodology for formulating simplified linear airfoil theories, a highly productive series of papers has appeared in the recent literature. For the steady-state problem, this includes a contribution by Reissner[7] and a set of two papers by Lawrence[8] and Flax and Lawrence.[9] The oscillating unswept airfoil has been treated by Reissner[10] and Lawrence and Gerber[11] on the basis of certain of the ideas of references 7 and 8.

All of these analyses have in common the approach of introducing mathematical simplifications into the partial integrodifferential equation of lifting surface theory. By introducing the simplifications in a systematic, though arbitrary, fashion, the authors mentioned are able to duplicate the mathematics of the various known simplified theories and are also able to point toward new directions for study.

In contrast to the essentially mathematical approach of Reissner, Lawrence, et al., the present authors decided to stress a more physical approach to the formulation of an aerodynamic model of the wing. Considering the Prandtl theory first, the physical reasoning leading to the associated steady-state aerodynamic model is reviewed from the standpoint of relaxing the requirements of the accurate surface loading theory to the least extent. The Cicala extension for the oscillating airfoil is considered in a similar light.

The Weissinger steady-state theory is then treated from an analogous physical point of view, thus leading to the considerations important to the objectives of this paper—i.e., the extension of the Weissinger model to the oscillating airfoil case.

For each of the airfoil theories, a concrete physical model is deduced; however, the exact mathematical relationship of these models to the integrodifferential equation of surface loading theory is *not* explored. For the immediate problem, at least, the authors are of the opinion that this line of attack affords greatest simplicity without sacrifice of theoretical power and authority.

One advantage of the present approach is that, once the appropriate physical model is deduced, convenient means for arranging the required wing calculations at once suggest themselves. Also, directions for research aimed toward improved theories become evident.

Since the present reasoning places the Prandtl and Weissinger theories in a somewhat different perspective from the work of references 7 through 9, this paper may also be of value in supplying a different approach to classification of these basic wing theories.

ANALYTICAL TOOLS

While the approach of this paper is essentially nonmathematical, it is desirable to fix certain ideas in mathematical terms. To permit this, an outline is now given of the aerodynamics of a horseshoe vortex pattern with a bound vorticity of uniform intensity across the horseshoe span but of harmonically varying intensity in the time coordinate. The horseshoe pattern can be thought of as a small spanwise segment of the wing in question. A schematic representation of the pattern is shown in Fig. 1a.

To nondimensionalize the analysis, let all distances be referred to the local semichord b of the wing, and let the time be referred to b/V, where V is the wing forward speed (taken as a constant). Without loss of generality, b can be given the value of 1. Let 2η be the span of the horseshoe pattern, and let k be the reduced frequency of the bound vorticity oscillation.

If the bound vorticity of the horseshoe leads to a bound circulation, constant along the span, of $\bar{\Gamma}e^{ik\tau}$, then known principles permit the deduction that the two trailing vortices $\bar{\Gamma}_t$ must have the variable intensity $\bar{\Gamma}e^{ik(\tau-\xi)}$, while the wake vorticity has the dis-

tribution $ik\bar{\Gamma}e^{ik(\tau-\xi)}$. The positive directions for circulation and vorticity correspond with the arrow directions in Fig. 1.

It should next be noted that the wake vorticity of the Fig. 1a pattern can obviously be represented as the sum of the two wake patterns shown in Fig. 1b. Considering now Fig. 1b, it is seen that the wake effects for the horseshoe can be represented in terms of the two-dimensional vorticity distribution γ_1, plus the pattern consisting of the two trailing vortices Γ_t and the two spanwise semi-infinite vorticity distributions γ_2. Evidently, in absolute magnitude, the vorticities γ_1, γ_2, and γ_w are all equal.

Next, it is of interest to calculate the downward induction velocities due to the Fig. 1b patterns at a point (x, y), the coordinates being defined in the figure. By well-known methods and after some algebraic manipulation and evaluation of integrals, it can be shown that the downwash due to the γ_1 distribution is $\Delta\bar{w}_1 e^{ik\tau}$, where

$$\Delta\bar{w}_1 = (\bar{\Gamma}/2\pi)ike^{-ikx}G(kx) \tag{1}$$

$$G(kx) = \int_{-kx}^{\infty} e^{-i\lambda}\frac{d\lambda}{\lambda} = -Ci(kx) - i\left\{\frac{\pi}{2} + Si(kx)\right\} \tag{2}$$

The downwash due to the $\Gamma_t - \gamma_2$ combination is given by a more complicated expression and is $\Delta\bar{w}_2 e^{ik\tau}$, where

$$\Delta\bar{w}_2 = \frac{\bar{\Gamma}}{4\pi}\left\{\frac{2\eta}{\eta^2 - y^2} + \frac{x}{(\eta + y)R_1(x)} + \frac{x}{(\eta - y)R_2(x)} - ike^{-ikx}\left[I\{k(\eta + y)\} + I\{k(\eta - y)\}\right]\right\} \tag{3}$$

and where

$$\left.\begin{aligned} R_1(x) &= \{x^2 + (\eta + y)^2\}^{1/2}; \qquad R_2(x) = \{x^2 + (\eta - y)^2\}^{1/2} \\ I(k\zeta) &= \int_{-kx}^{\infty} e^{-i\lambda}\left\{\frac{1}{k\zeta} + \frac{1}{\lambda} - \frac{\sqrt{\lambda^2 + (k\zeta)^2}}{\lambda(k\zeta)}\right\}d\lambda \end{aligned}\right\} \tag{4}$$

For the evaluation of the integral $I(k\zeta)$, it is readily shown that, for $\zeta > 0$,

$$I(k\zeta) = F(k\zeta) + H(k\zeta) + (i/k\zeta)(1 - e^{ikx}) \tag{5}$$

where $F(k\zeta)$ is the Cicala function[2]

$$F(k\zeta) = \int_0^{\infty} e^{-i\lambda}\left\{\frac{1}{k\zeta} + \frac{1}{\lambda} - \frac{\sqrt{\lambda^2 + (k\zeta)^2}}{\lambda(k\zeta)}\right\}d\lambda \tag{6}$$

and $H(k\zeta)$ is a new function, readily evaluated,

$$H(k\zeta) = \int_{-kx}^{\infty} e^{-i\lambda}\left\{\frac{1}{\lambda} - \frac{\sqrt{\lambda^2 + (k\zeta)^2}}{\lambda(k\zeta)}\right\}d\lambda \tag{7}$$

For $\zeta < 0$, the integral $I(k\zeta)$ becomes

$$I(k\zeta) = 2G(kx) - I\{k|\zeta|\} \tag{8}$$

It is now of interest to show how the Fig. 1 horseshoe pattern can be used to construct the flow field about an unswept rectangular wing of span $2l$ with a bound circulation distribution across the span of $\Gamma(y)$; for this simple example, it will further be assumed that the wing is oscillating in a spanwise-symmetrical mode—i.e., $\Gamma(y)$ is symmetrical about the mid-span. The procedure in this case is well known; rather than think of the Fig. 1 pattern as a small spanwise segment, it is equally convenient to construct the wing from a series of Fig. 1 patterns, each symmetrical about the mid-span and each of successively larger span from a value near zero to a value approaching $2l$. The bound circulation for each such horseshoe is notated $\Delta\Gamma$.

Since only symmetrical wing modes are considered, it is sufficient to consider the flow over the right-hand side of the wing $0 < y < l$. Then, for the horseshoe with semispan η, the bound circulation intensity should be

$$\Delta\Gamma = -\{(d\Gamma/dy)dy\}_{y=\eta}$$

The downwash velocity at a point (x, y) due to the entire wake behind the wing can thus be compounded as a spanwise integral representing the summation of Δw_1 and Δw_2 components. If these summations yield downwash velocities of w_1 and w_2, respectively, and if w_b is the downwash due to the bound vorticity, then the total downwash at point (x, y) is given by

$$w_t = w_b + w_1 + w_2 \tag{9}$$

If point (x, y) is on the wing and if the downward deflection of the wing at any instant is Z_a, then

$$w_t = (\partial Z_a/\partial \tau) + (\partial Z_a/\partial x) \tag{10}$$

The combination of Eqs. (9) and (10) leads to the integrodifferential equation governing the aerodynamic surface loading problem.

It will be shown later how the Fig. 1 type of pattern can be used to construct the flow about a wing of arbitrary plan form. For this purpose, each horseshoe is used in place of a small spanwise segment of the wing.

The Prandtl and Cicala Models

The classic Prandtl model for a thin wing in steady-state unseparated flow and the Cicala extension to the oscillating wing case are based on so-called "lifting-line" considerations. This designation arises from the mental image of a wing with a substantially larger span than chord, immersed in a large body of fluid. The wing dimensions being small compared with those of the fluid boundaries, the lift forces induced on the wing appear to act over a relatively thin "line" in space.

For the purposes of this paper, it is desirable to replace this graphic usage of the term "lifting line" by its strictly literal connotation—i.e., *as a line vortex immersed in a body of fluid*. On the basis of such a literal interpretation of the term "lifting line," it is interesting to note that the Prandtl-Cicala model does not entail lifting-line considerations but rather can be constructed solely on the basis of surface loading arguments. This will now be demonstrated, using an unswept rectangular wing purely for illustrative purposes and following the line of reasoning advanced by von Kármán and Burgers.[5]

The Prandtl-Cicala simplification of exact wing theory presupposes an essentially unswept airfoil of appreciable aspect ratio. The vorticity pattern associated with the wing aerodynamics consists of the bound vorticity, which runs essentially normal to the main flow direction, and the wake vorticity. For the steady-state case, the wake vorticity trails rearward indefinitely and extends only parallel to the main flow; if the airfoil is oscillating, a wake vorticity pattern running normal to the main flow direction is added (see Fig. 1). For the unswept rectangular wing in particular, it has already been shown how the flow pattern can be constructed from a series of Fig. 1 horseshoe patterns, each of slightly larger span than the next.

Consider now the fluid downwash induced at a spanwise station of the wing, and consider first the component arising from the bound vorticity. Since the wing has a span that is large compared with the chord, it can be assumed that each spanwise wing station "sees" only a slowly changing circulation; thus it becomes possible to approximate the bound vorticity induction by setting it equal to that induced on a wing in two-dimensional flow, with the same chord and total circulation as the wing station in question. It is important to note that by this reasoning the bound vorticity at each station acts independently of that at all other stations—i.e., *interaction of the bound vorticity at different span stations is neglected.*

In terms of a typical horseshoe pattern of span 2η from which the unswept rectangular wing vorticity is constructed, the above argument can be rephrased as follows: In evaluating the induction effects at a point on the airfoil due to the bound vorticity associated with each horseshoe pattern, the span is assumed to be so large compared with the chord that, in the region $-\eta < y < \eta$, the induction of the two-dimensional airfoil theory is obtained. Outside the horseshoe span, the bound vorticity induction at points on the airfoil is zero.

Now, within the horseshoe span, it is at once clear that the combination of the induction due to the bound vorticity and the γ_1 distribution of Fig. 1b is merely equal to the total downwash from the two-dimensional theory. The two-dimensional analysis shows that if the downwash velocity of an uncambered oscillating airfoil is measured at the rear quarter-chord point, then the two-dimensional downwash $\Delta\bar{w}_{II}e^{ik\tau}$ is given by, for $b = 1$,

$$\Delta\bar{w}_{II} = (\Delta\bar{\Gamma}/2\pi)\mu \tag{11}$$

where

$$\mu(k) = \frac{\pi k}{2}\left\{H_0^{(2)}(k) - iH_1^{(2)}(k)\right\}e^{ik} \tag{12}$$

With regard to the calculation of the induction effects due to $\Gamma_t - \gamma_2$ within the horseshoe span and due to $\gamma_1 - \Gamma_t - \gamma_2$ outside the span, it is seen that *consistency with the prior assumptions implies that (a) the wake flows can be considered to start at any arbitrary chordwise point without introducing appreciable error into the analysis and (b) the induction due to the wake is relatively constant over the chord and, hence, can be evaluated at an arbitrary chordwise point.* For convenience, it at once appears reasonable both to start the wake and to evaluate the downwash along the line $x = 0$. It is important to note that the origin of x need no longer be located as in Fig. 1b; its precise location need not be specified and is immaterial, it only being required that the line $x = 0$ pass somewhere within the airfoil chord.

With the model construction now complete, the corresponding differential equation is readily formulated. Adding up the effects of the various horseshoe patterns,

$$\bar{w}_t = \frac{\mu}{2\pi}\bar{\Gamma}(y) - \frac{1}{4\pi}\int_0^y \frac{d\bar{\Gamma}}{d\eta}\left\{\frac{2\eta}{\eta^2 - y^2} - ik[F\{k(y+\eta)\} - F\{k(y-\eta)\}]\right\} d\eta -$$

$$\frac{1}{4\pi}\int_y^l \frac{d\bar{\Gamma}}{d\eta}\left\{\frac{2\eta}{\eta^2 - y^2} - ik[F\{k(\eta+y)\} + F\{k(\eta-y)\}]\right\} d\eta \quad (13)$$

It follows that $\bar{w}_t$, which describes the actual wing motion and is a function of the spanwise coordinate y, should be evaluated at the rear quarter-chord point.

The Prandtl-Cicala model has thus been established by a reasoning process based entirely on surface loading considerations. The terminology "quasi-surface" appears to delineate the model features more accurately than does the conventional lifting-line description.

The Weissinger Model

In analyzing the steady-state spanwise loading of sharply swept wings, Weissinger[1] concluded that the Prandtl theory is not adequate and will not yield results of acceptable accuracy. A principal reason for this is the neglect of bound vorticity interaction, which is embodied in the Prandtl approach. Thus, for a sharply swept wing, it is clear that a particular wing station cannot "see" a bound vorticity induction that can be approximated in terms of a straight two-dimensional (infinite span) wing. To remedy this deficiency, Weissinger proposed a new aerodynamic wing model. However, unlike the Prandtl model, the Weissinger counterpart cannot be constructed solely from surface loading considerations but must be based on replacement of the wing bound vorticity by an actual lifting line—i.e., a line vortex.

The reasoning leading to the Weissinger model is as follows: A general conclusion of two-dimensional unsteady airfoil theory is that the circulation induced around a wing is directly proportional to the downwash acting at the rear quarter-chord point. Moreover, for the steady-state case, if the bound vorticity of the airfoil is assumed to be concentrated into a line vortex placed at the forward quarter-chore point, then the relationship between circulation and downwash for the lifting-line model is the same as that from two-dimensional wing theory. Note further that the center of pressure of the circulatory forces for a two-dimensional wing acts at the forward quarter-chord point; for the line vortex model, the total life force acts at this same point.

Since Weissinger presupposes a wing of reasonably large aspect ratio, in establishing a model for an airfoil with variable circulation across the span, he resorts to a modification of the two-dimensional line vortex model just described. Thus, he first replaces the bound vorticity by a line vortex running along the forward quarter-chord line of the wing; the circulation of the line vortex at each station is the same as that acting for the actual airfoil. The wake vorticity pattern, which must start at the line vortex and trail to the rear, is then fixed in accordance with the known principles of vortex continuity.

The downwash due to this pattern of line and wake vorticity is then calculated along the rear quarter-chord line of the wing, thus affording a relationship between the downwash at each station and the spanwise distribution of bound circulation. The downwash so calculated is set equal to that required by the airfoil motion along the rear quarter-chord line of the plan form. It is readily seen that this procedure leads to an integrodifferential equation relating the wing motion and the spanwise circulation distribution—i.e., the Weissinger equation.

It is to be particularly noted that this model incorporates the effects of interaction of the bound vorticity all along the wing on the downwash at a particular station, a requirement noted earlier as essential to an adequate swept-wing theory.

The final feature of the Weissinger model is the interpretation of the computed circulation distribution in terms of lift and pitching moment. Since the wing is of reasonably large aspect ratio, so that each station can be assumed to approximate two-dimensional behavior, Weissinger sets the local lift and pitching moment for each spanwise station of the wing equal to that which would act on a two-dimensional wing with the same local chord and with the same local circulation as the concentrated line vortex.

The Present Model

It is now possible to establish the characteristics of a model that extends the Weissinger steady-state argument to the oscillating airfoil case. As for the Weissinger model, the bound vorticity of the airfoil is replaced by a concentrated line vortex running along the forward quarter-chord line of the wing. This placement of the lifting line coincides with the theoretical location of the circulatory center of pressure for a two-dimensional wing in unsteady motion.

Consider now the rearward trailing wake vorticity for the actual airfoil. This consists of a component parallel to the main flow and a component normal to the main flow shed from the trailing edge of the wing. Both of these components are shown in Fig. 1 for an isolated spanwise segment of the wing, although it is to be noted that the present argument is not restricted to an unswept wing but is applicable for a general plan form.

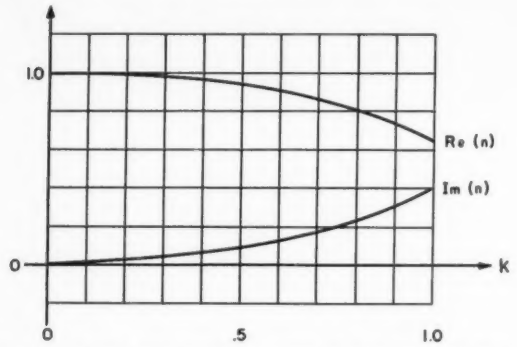

FIG. 2. Real and imaginary parts of the function $n(k)$.

It has earlier been deduced that, if the bound vorticity is $\bar{\Gamma}e^{ik\tau}$, then the trailing vortices in Fig. 1 have the value $\Gamma_t = \bar{\Gamma}e^{ik(\tau-\xi)}$, and the wake vorticity normal to the flow is given by $\gamma_w = ik\bar{\Gamma}e^{ik(\tau-\xi)}$; here, ξ is a rearward coordinate starting at the trailing edge.

Now define a new rearward coordinate ξ' with origin at the local forward quarter-chord point. For a unit local semichord, it follows that $\xi' = \xi + (3/2)$. Then the wake trailing vortices for a Fig. 1 type wing element can be written as $\bar{\Gamma}e^{ik[\tau-\xi'+(3/2)]}$, and the wake vorticity normal to the flow can be written as $ik\bar{\Gamma}e^{ik(\tau-\xi'+(3/2)]}$.

Returning now to the construction of the lifting-line model, it is an obvious computational convenience to assume that the wake springs from the line vortex at the forward quarter-chord point. Since the wing is supposed to be of reasonable aspect ratio, this type of construction seems warranted by the same reasoning as was used by Weissinger. Hence, as a preliminary trial, the model should consist of the concentrated line vortex plus the wake specified in the last paragraph, extending from the forward quarter-chord point $\xi' = 0$ to $\xi' = \infty$.

As in the Weissinger case, the downwash satisfaction should be accomplished along the rear quarter-chord line of the wing—i.e., the actual wing motion should be duplicated by the model along this line.

Now consider the accuracy of this model in terms of a two-dimensional wing; it is clear that one requirement of the model should be that it reduces to the exact results for this limiting situation. The two-dimensional theory leads to the relations Eqs. (11) and (12) between the bound circulation and the rear quarter-chord downwash. *For the present model, it will be found necessary to arbitrarily multiply the bound vorticity by the semiempirical factor* $ne^{i(3/2)k}$ *in order to duplicate these results.* This is seen from the following reasoning:

If the lifting line, actually of intensity $\bar{\Gamma}e^{ik\tau}$, is assigned the intensity $ne^{i(3/2)k}\bar{\Gamma}e^{ik\tau}$, then the downwash induced by it at the rear quarter chord is, for a unit semichord,

$$w_b = (1/2\pi)n\bar{\Gamma}e^{ik[\tau+(3/2)]} \tag{14}$$

The two-dimensional wake of the model contributes a downwash at this same point of

$$w_1 = \frac{1}{2\pi}\int_0^\infty \frac{\gamma_w(\xi')d\xi'}{\xi' - 1} = \frac{ik}{2\pi}\bar{\Gamma}e^{ik[\tau+(1/2)]}G(k) \tag{15}$$

where $G(k)$ is given by Eq. (2). Equating $w_b + w_1$ to the exact theoretical value,

$$w_{II} = \bar{\Gamma}e^{ik\tau}[\mu(k)/2\pi] \tag{16}$$

yields the result

$$e^{i(k/2)}\{n(k)e^{ik} + ikG(k)\} = \mu(k) \tag{17}$$

A plot of n vs. k is shown in Fig. 2. It is seen that n has a value close to unity for small values of k (<0.4) and departs from unity as k increases.

Based on this discussion, it is now possible to finally fix the details of the lifting-line model for the oscillating wing:

(a) The bound circulation of the actual wing is replaced by a line vortex running along the forward quarter-chord line of the wing. For a spanwise wing station where the actual bound circulation is Γ and the local semichord is b, the line vortex is arbitrarily assigned the intensity $n\Gamma e^{ik[(3/2)b]}$.

(b) The wake intensity at a point behind the wing is deduced on the basis of accurate surface loading considerations—i.e., as if the wake is shed from the trailing edge. This determines the wake vorticity at a distance ξ' behind the line vortex. After this is fixed, in the interests of computational convenience, the wake is arbitrarily extended from the trailing edge up to the lifting line.

(c) The boundary conditions relating to the wing downwash are then satisfied along the rear quarter-chord line of the wing.

(d) The model described above leads to an integrodifferential equation for the spanwise distribution of wing circulation. After this is solved, the circulation at each station is related to the local wing lift by the expression from two-dimensional wing theory. The chordwise center of pressure at each station is taken at the forward quarter-chord point.

To fix ideas, the application of this model to the unswept rectangular wing in symmetrical motion is now considered. Constructing the wing from a series of horseshoe patterns, each symmetrical about the midspan and each of slightly larger span than the next, the integrodifferential equation for the problem is readily formulated as

$$\bar{w}_l = \frac{e^{(3/2)ik}}{4\pi}\left\{2ike^{-ik}n(k)G(k)\bar{\Gamma}(y) - \int_0^l \frac{d\bar{\Gamma}}{d\eta}\left[\frac{2\eta e^{-ik}}{\eta^2 - y^2} + \frac{1}{(\eta+y)\{1+(\eta+y)^2\}^{1/2}} + \right.\right.$$
$$\frac{1}{(\eta-y)\{1+(\eta-y)^2\}^{1/2}} + n(k)\left(\frac{\eta+y}{\{1+(\eta+y)^2\}^{1/2}} + \frac{\eta-y}{\{1+(\eta-y)^2\}^{1/2}}\right)\Big]d\eta + ike^{-ik} \times$$
$$\int_0^y \frac{d\bar{\Gamma}}{d\eta}\left[F\{k(\eta+y)\} + H\{k(\eta+y)\} - F\{k(y-\eta)\} - H\{k(y-\eta)\}\right]d\eta + ike^{-ik} \times$$
$$\left.\int_y^l \frac{d\bar{\Gamma}}{d\eta}\left[F\{k(\eta+y)\} + H\{k(\eta+y)\} + F\{k(\eta-y)\} + H\{k(\eta-y)\}\right]d\eta\right\} \quad (18)$$

Sample Calculations

To illustrate the character of the results yielded by the presently proposed model (M.R.I. model), a series of calculations are now reported for an uncambered, untapered wing of aspect ratio 5, oscillating with reduced frequency $^1/_3$; both an unswept wing and a wing with 45° sweepback are considered. The two wings are assumed to be oscillating in a variety of spanwise-symmetrical modes having the following shapes: (a) uniform translation of the entire wing, normal to its own plane, as a rigid body; (b) uniform pitching of the wing about the forward quarter-chord line as a rigid body; (c) flapping motion of the wing according to a mode shape that is linear along the span, starting with zero at the root and reaching the value one at the tip; (d) pitching motion of the wing about the forward quarter-chord line according to a linear spanwise mode shape, starting with zero at the root and reaching the value one at the tip; (e) flapping motion of the wing according to a parabolic spanwise mode shape, with amplitude zero at the root and one at the tip; and (f) pitching motion of the wing according to a parabolic spanwise mode shape, with amplitude zero at the root and one at the tip.

For the unswept wing, to permit comparison of the M.R.I. model results with those from other models, calculations are also reported on the basis of the Cicala theory and on the basis of the Reissner theory.[3, 4]

For the Cicala and the M.R.I. models, the appropriate integrodifferential equations were solved approximately by constructing the flow for each wing from five discrete horseshoe vortex patterns, each symmetrical about the wing mid-span. Letting $y = l\cos\theta$, the horseshoe spans were determined by $\theta = 0°$, 20°, 40°, 60°, and 80°. Satisfaction of the downwash condition was then accomplished at the stations defined by

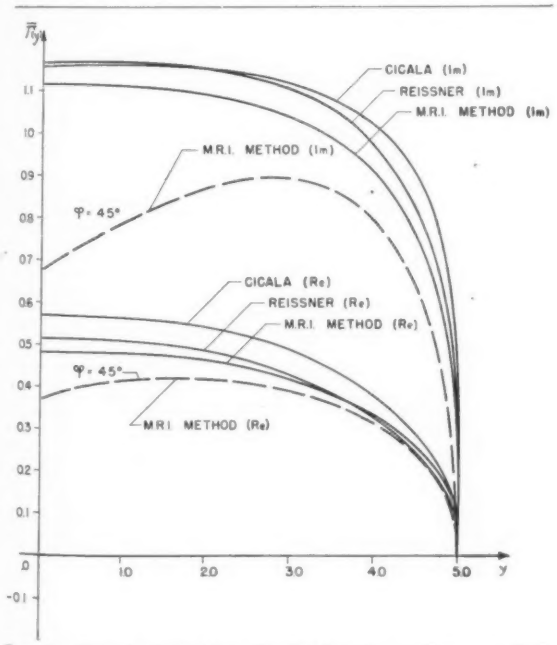

FIG. 3. Bound circulation distribution for uniform vertical translation (A.R. = 5.0, k = 1/3).

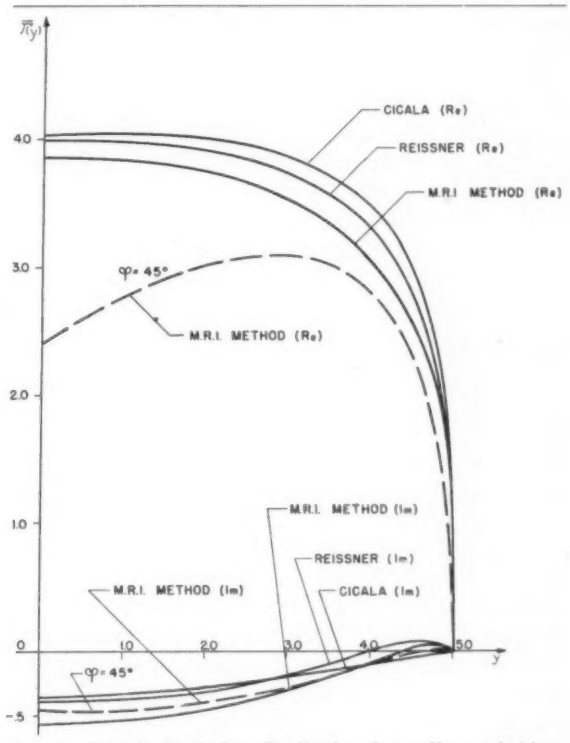

FIG. 4. Bound circulation distribution for uniform pitching (A.R. = 5.0, k = 1/3).

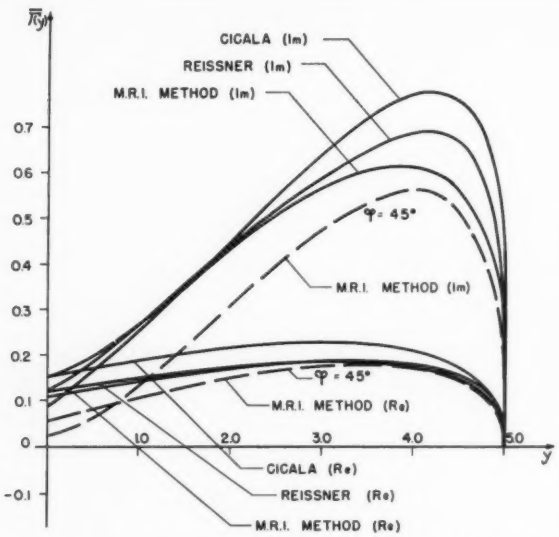

FIG. 5. Bound circulation distribution for symmetrical linear bending (A.R. = 5.0, $k = 1/3$).

$\theta = 14°$, $32°$, $51°$, $70°$, and $90°$; save for the $\theta = 90°$ station, these stations geometrically bisect the distances from the extremity of one horseshoe to the next. This construction permits the determination of the circulation $\bar{\Gamma}$ at the five stations where the downwash conditions are satisfied.

For the computations by the Reissner method, the procedures outlined in reference 4 were followed without change.

The results for all the calculations are shown in Figs. 3 to 8. Considering first the M.R.I. model results alone, it is to be noted that the effect of sweep is to cause a reduction in the relative inboard wing loading; this behavior is similar to that encountered in the steady-state loading case.

For the unswept wing, it is to be noted that both the Cicala and Reissner results are in approximate agreement, while the M.R.I. model yields generally lower wing loading magnitudes, particularly in the tip regions. This behavior of the M.R.I. model is not unexpected, since it coincides with the general performance of the Weissinger method for the steady-state case (see reference 1, p. 18). Weissinger points out that his lifting-line model is useful mainly in the study of swept wings and is, in fact, at a disadvantage when applied to unswept cases.

In view of the paucity of reliable experimental data for the spanwise loading of oscillating wings, a more detailed analysis of the present calculations does not appear to be useful. Perhaps the most efficient means for checking the validity of the M.R.I. model under present experimental circumstances is by comparing the results of carefully conducted flutter experiments with those from analytical computations. Limited experience with the M.R.I. model in such studies indicates that it yields fair results for unswept wings and fairly good results for sharply swept wings.

Further Developments

As extensions to the present work, it is worthy of mention that a continuation of the present reasoning to a more advanced wing model might entail the use of two discrete line vortices instead of one to replace the wing bound vorticity. Holme[12] discusses the placement and use of multiple lifting lines in the steady-state case. An extension of his work would be required for the oscillating airfoil. It is to be noted that the employment of multiple lifting lines enables the study of shifts in the local chordwise centers of pressure from the forward quarter-chord point.

Also of interest as an extension to the present work is the deduction of convenient computational procedures for use with the M.R.I. model. For the steady-state case, Diederich[13] shows how the flow about a wing of completely arbitrary plan form can be constructed from a series of small-span unswept horseshoe patterns placed side by side. The use of this technique appears well suited for the present purposes and affords substantial advantages in reducing the amount of basic tabulations required for a design-office method. Through this approach, wings with nonstraight quarter-chord lines can be handled with the same facility as unswept or straight-swept wings.

References

[1] Weissinger, J., *The Lift Distribution of Swept-Back Wings*, Nat. Adv. Comm. Aero. Tech. Memo. No. 1120, March, 1947. (Translation from the original German source.)

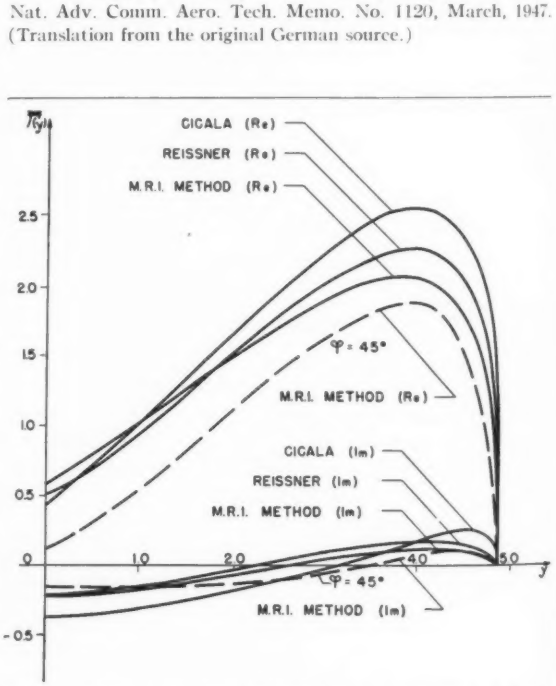

FIG. 6. Bound circulation distribution for symmetrical linear twist (A.R. = 5.0, $k = 1/3$).

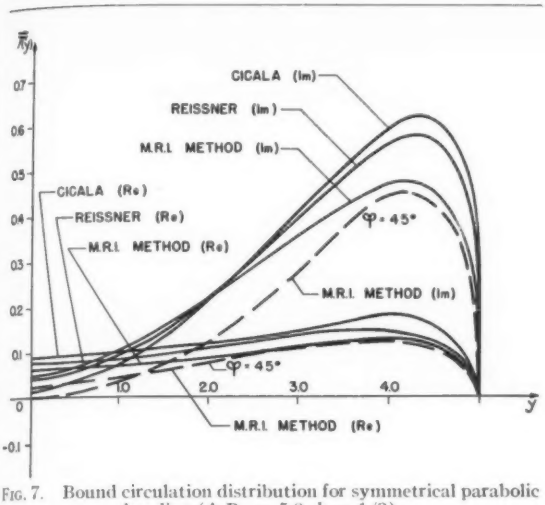

FIG. 7. Bound circulation distribution for symmetrical parabolic bending (A.R. = 5.0, k = 1/3).

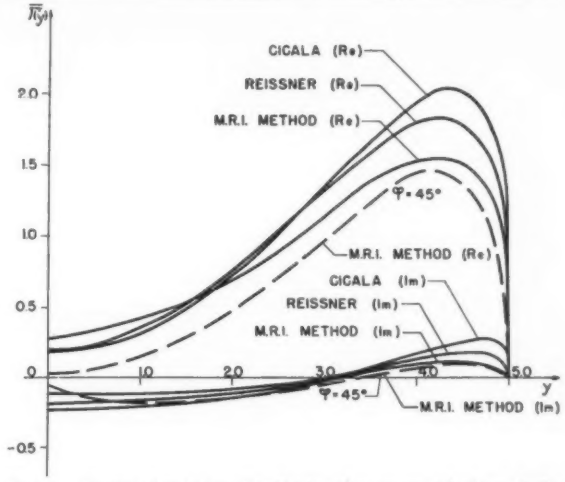

FIG. 8. Bound circulation distribution for symmetrical parabolic twist (A.R. = 5.0, k = 1/3).

[2] Cicala, P., *Comparison of Theory with Experiment in the Phenomenon of Wing Flutter*, Nat. Adv. Comm. Aero. Tech. Memo. No. 887, February, 1949. (Translation from the original Italian source.)

[3] Reissner, E., *Effect of Finite Span on the Airload Distributions for Oscillating Wings. I—Aerodynamic Theory of Oscillating Wings of Finite Span*, Nat. Adv. Comm. Aero. Tech. Note No. 1194, March, 1947.

[4] Reissner, E., and Stevens, J. E., *Effect of Finite Span on the Airload Distribution for Oscillating Wings. II—Methods of Calculation and Examples of Application*, Nat. Adv. Comm. Aero. Tech. Note No. 1195, October, 1947.

[5] Durand, W. F., et al., *Aerodynamic Theory*, Durand Reprinting Committee, California Institute of Technology, January, 1943; Vol. II, Div. E III, Sec. 27, p. 149.

[6] Wasserman, L. S., *Aspect Ratio Corrections in Flutter Calculations*, Wright Air Development Command, Memo. Rep. No. MCREXA5-4595-8-5, Dayton, Ohio, August 26, 1948.

[7] Reissner, Eric, *Note on the Theory of Lifting Surfaces*, Reprinted from the Proceedings of the National Academy of Sciences, Vol. 35, No. 4, pp. 208–215, April, 1949.

[8] Lawrence, H. R., *The Lift Distribution on Low Aspect Ratio Wings at Subsonic Speeds*, Journal of the Aeronautical Sciences, Vol. 18, No. 10, pp. 683–695, October, 1951.

[9] Flax, A. H., and Lawrence, H. R., *The Aerodynamics of Low-Aspect-Ratio Wings and Wing-Body Combinations*, Proceedings, Third Anglo-American Aeronautical Conference, 1951.

[10] Reissner, Eric, *Investigation of Oscillating Lifting Surfaces of Finite Span in Incompressible Flow*, Technical Report for Air Research and Development Command, October 30, 1951.

[11] Lawrence, H. R., and Gerber, E. H., *The Aerodynamic Forces on Low-Aspect-Ratio Wings Oscillating in an Incompressible Flow*, Cornell Aeronautical Laboratory, Inc., Report No. AF-781-A-1, January, 1952.

[12] Holme, Olof A. M., *On the Approximate Solution of the Lifting Surface Problem with the Aid of Discrete Vortices*, Division of Aeronautics, Royal Institute of Technology, Stockholm 26, March 29, 1949.

[13] Diederich, F. W., *Charts and Tables for Use in Calculations of Downwash of Wings of Arbitrary Plan Form*, N.A.C.A. T.N. No. 2353, May, 1951.

Changes of Address

Since the Post Office Department does not as a rule forward magazines to forwarding addresses, it is important that the Institute be notified of changes in address 30 days in advance of publishing date to ensure receipt of every issue of the JOURNAL and REVIEW.

Notices should be printed legibly and sent directly to:

Institute of the Aeronautical Sciences, Inc.

2 East 64th Street, New York 21, New York

On the Temperature Distribution Along a Semi-Infinite Sweat-Cooled Plate*

NATHAN NESS†

Polytechnic Institute of Brooklyn

ABSTRACT

A theoretical investigation of the temperature distribution along a semi-infinite porous flat plate under the condition of uniform injection from the bottom of the plate is made.

A heat-balance differential equation of the second order, including a term containing the physical parameters of the plate, is derived and is employed in conjunction with the well-known Prandtl boundary-layer equations of continuity, momentum, and energy for a solution of the problem.

The temperature distribution along the plate is obtained for the respective cases of thermal conductivity not equal to, and equal to, zero. Results show that the inclusion of the thermal conductivity term in the heat-balance equation eliminates the infinite temperature gradient at the leading edge.

Other results when thermal conductivity is considered are: (a) The boundary conditions at the leading edge—i.e., the ratio of wall to free-stream temperature and the axial temperature gradient there—may not be chosen arbitrarily but are related mathematically to each other; (b) the ratio of thermal to velocity boundary-layer thickness is less than unity at the leading edge for Prandtl Numbers greater than 0.35 and is equal to unity at an infinite distance downstream; and (c) at an infinite distance downstream, the wall temperature approaches the coolant temperature.

NOMENCLATURE

x = distance along the plate measured from the leading edge
y = distance normal to the plate
u = velocity component parallel to plate
v = velocity component normal to plate
ρ = mass fluid density
μ = coefficient of viscosity
ν = μ/ρ, kinematic viscosity
c_p = coefficient of specific heat at constant pressure
P = $\mu c_p/k_g$, Prandtl Number
l = distance between coolant reservoir and porous plate
h = thickness of porous plate
k_g = coefficient of heat conduction of the hot fluid
k_m = coefficient of heat conduction of the plate
T = temperature, deg. abs.
T_c = temperature of the coolant
α = $(1/hT_w)\int_h T\,dy$, a constant limited to $0 < \alpha < 1$ for injection cooling
r = constant ratio of porous to total plate cross-sectional area
δ = boundary-layer thickness
λ_v = $v_w\delta_v/(6\nu)$, nondimensional velocity boundary-layer thickness
λ_t = $Pv_w\delta_t/(6\nu)$, nondimensional thermal boundary-layer thickness
ξ = $(v_w/u_1)^2(u_1x/\nu)$, nondimensional length along the plate
η = y/δ, nondimensional distance normal to the plate
L = finite length of plate
K = $\alpha(u_1h/\nu)(v_w/u_1)^2[(1 - r)(k_m/k_g) + r]$, a constant
C = $-1/(210K)$, a constant
τ = $1 - T_w/T_1$
J = $\delta_t/\delta_v = \lambda_t/(P\lambda_v)$, boundary-layer thickness ratio

F is defined by Eq. (13). Prime $\equiv d/d\xi$; double prime $\equiv d^2/d\xi^2$.

Subscripts

w = hot surface of the plate
0 = leading edge of plate
∞ = infinite distance downstream along the plate
v = velocity boundary layer
t = thermal boundary layer
1 = local values at the outer edge of the boundary layer

INTRODUCTION

THE PROBLEM OF DETERMINING the temperature distribution along a semi-infinite porous flat plate, subjected to a high-temperature gas flow on one side and cooled by means of cold fluid injection from the other side of the wall, is considered. This method of decreasing wall temperatures is known as "sweat-cooling."

The fluid dynamic equations considered are those that are valid in the velocity and thermal boundary layers. These equations are the well-known Prandtl boundary-layer equations of continuity, momentum, and energy. The wall temperature is introduced as a dependent variable through the derivation of a heat-balance differential equation. This equation is of the second order; the second-order term (which is multiplied by a factor containing the physical parameters of the plate) arises from a consideration of the thermal conductivity along the plate and appears not to have been treated previously in the literature.

The assumptions made in this investigation are: (1) The fluid is incompressible; (2) the flow is entirely laminar; and (3) the hot fluid flowing along the wall and the coolant flowing through the pores are the same.

In the solution of the laminar boundary-layer equations, the momentum and energy equations are reduced

Received November 15, 1951. Revised and received May 7, 1952.

* Doctoral dissertation at the Polytechnic Institute of Brooklyn based on work conducted under the auspices of Project Squid, jointly sponsored by the Office of Naval Research and the Office of Air Research under contract N6-ori-98, Task Order 2, NR-220-039. The author's sincere gratitude goes to his dissertation adviser, Prof. Morris Morduchow, for his many invaluable suggestions, and to Prof. Shao Wen Yuan for suggesting the topic and initiating the investigation.

† Research Group Leader, Department of Aeronautical Engineering and Applied Mechanics.

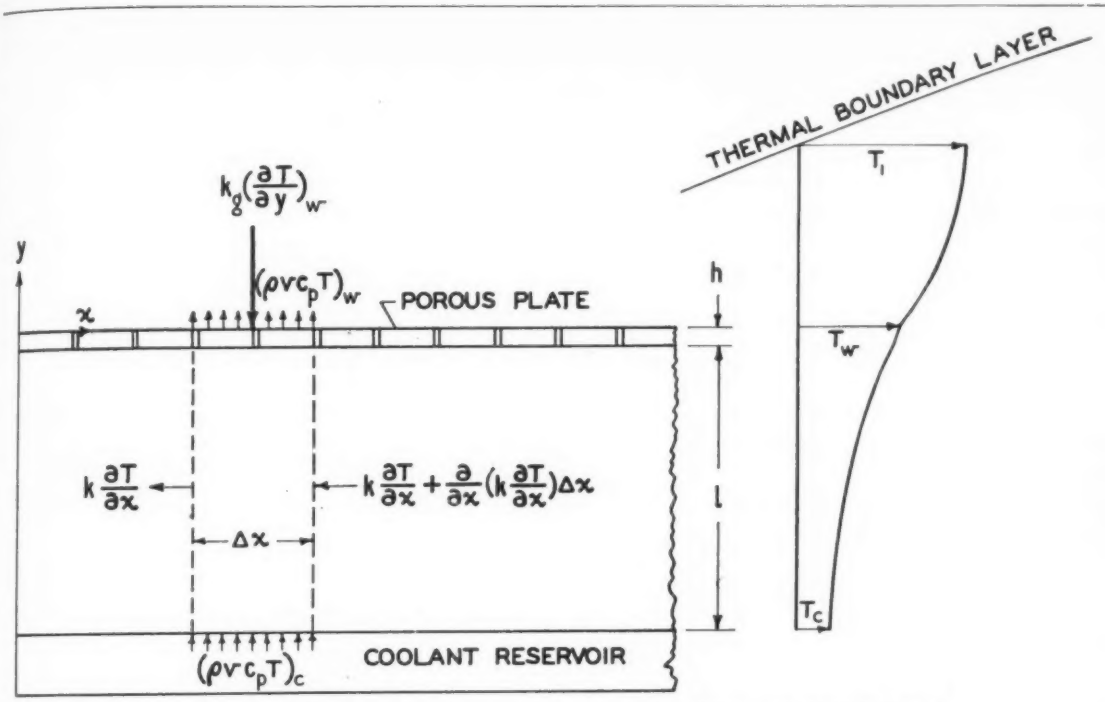

FIG. 1 DERIVATION OF HEAT BALANCE EQUATION

to the von Kármán integral form. Velocity and temperature boundary-layer profiles as polynomials of the fourth degree are assumed. The assumption of incompressibility is found to imply that the momentum equation is not coupled with the energy equation; therefore, the substitution of the velocity boundary-layer profile into the momentum integral equation permits the determination of the velocity boundary-layer thickness without the use of the energy or heat-balance equations.

The temperature distribution along the plate and the thermal boundary-layer thickness are calculated, first with the thermal conductivity term included in the heat-balance equation and then with the thermal conductivity term neglected. For the first case, the temperature distribution and the thermal boundary-layer thickness are obtained by the numerical solution of two simultaneous first-order nonlinear ordinary differential equations, which result from a combination of the heat-balance and energy equations, and from the energy equation itself. For the second case, a combination of the simplified heat-balance equation (i.e., the heat-balance equation with plate thermal conductivity neglected) and the energy equation results in an algebraic equation that is solved graphically for the thermal boundary-layer thickness. The substitution, then, of the thermal boundary-layer thickness into the simplified heat-balance equation gives the wall temperature.

Basic Equations

The laminar incompressible two-dimensional boundary-layer equations for flow over a flat plate parallel to the stream are:

The equation of conservation of momentum:

$$u(\partial u/\partial x) + v(\partial u/\partial y) = \nu(\partial^2 u/\partial y^2) \qquad (1)$$

The equation of the conservation of energy:

$$u(\partial T/\partial x) + v(\partial T/\partial y) = (\nu/P)(\partial^2 T/\partial y^2) \qquad (2)$$

The equation of continuity:

$$(\partial u/\partial x) + (\partial v/\partial y) = 0 \qquad (3)$$

It is assumed here that the viscosity and thermal coefficients are constant; moreover, the term representing the viscous dissipation—namely, $(\nu/c_p)(\partial u/\partial y)^2$—has been omitted because of the assumption of incompressibility.

The wall temperature is introduced as a variable by considering the heat balance of an element [of length Δx, of unit width, and of height $(h + l)$] of the system in Fig. 1. In the region between the porous plate and the coolant reservoir, it is assumed that $\partial T/\partial x$ is negligible and that the coolant is in one-dimensional flow normal to the plate. Furthermore, experimental results have shown[1] that the difference between the temperature of the cooling medium entering the pores and the temperature of the wall decreases to a negligible amount within an extremely thin layer inside the wall

The resulting heat-balance equation is, then,

$$k_q(\partial T/\partial y)_w + \alpha h[(1 - r)k_m + rk_q](d^2T_w/dx^2) = (\rho v)_w c_p(T_w - T_e) \quad (4)$$

where $\alpha = (1/hT_w)\int_h T\,dy$, a constant limited to $0 < \alpha < 1$ for injection cooling; r is the constant ratio of porous to total plate cross-sectional area; and the subscript w refers to conditions at the hot surface of the plate. It should be noted that no assumption of incompressibility has been made in the derivation of Eq. (4), although k_m and c_p have been assumed constant.

The first term of Eq. (4) represents the heat transferred from the hot fluid to the plate; the second term, which contains the physical parameters of the plate, is the heat transmitted along the plate; while the term on the right side of the equation is the heat absorbed by the coolant in its flow from the coolant reservoir to the hot surface of the plate.

Solution of the Basic Equations

A solution of Eqs. (1) to (4) is obtained by the Kármán-Pohlhausen method of reducing the momentum and energy equations to integral form and assuming velocity and temperature profiles as polynomials in y of the fourth degree.

Integrating Eq. (1) between the limits $y = 0$ and $y = \delta_v$, utilizing the equation of continuity and satisfying the following boundary conditions: at $y = 0$,

$$u = 0, \quad v = v_w \quad \text{(a constant)}$$

at $y = \delta_v$,

$$u = u_1, \quad v = v(\delta_v), \quad \partial u/\partial y = 0$$

one obtains

$$(d/dx)\int_0^{\delta_v} u^2\,dy - u_1(d/dx)\int_0^{\delta_v} u\,dy + v_w u_1 = -\nu(\partial u/\partial y)_w \quad (5)$$

A polynomial of the fourth degree as an approximation to the velocity boundary-layer profile satisfying the following boundary conditions: at $y = 0$,

$$u = 0, v = v_w, \quad v_w(\partial u/\partial y)_w = \nu(\partial^2 u/\partial y^2)_w$$

at $y = \delta_v$,

yields

$$u = u_1, \quad \partial u/\partial y = \partial^2 u/\partial y^2 = 0$$

$$\frac{u}{u_1} = \frac{2}{1 + \lambda_v}\eta_v + \frac{6\lambda_v}{1 + \lambda_v}\eta_v^2 - \frac{2 + 8\lambda_v}{1 + \lambda_v}\eta_v^3 + \frac{1 + 3\lambda_v}{1 + \lambda_v}\eta_v^4 \quad (6)$$

where $\eta_v = y/\delta_v$; $\lambda_v = v_w\delta_v/(6\nu)$; and δ_v and λ_v are the dimensional and nondimensional velocity boundary-layer thicknesses, respectively

The substitution of Eq. (6) into Eq. (5) results in

$$d\xi = \frac{2\lambda_v(36\lambda_v^3 + 108\lambda_v^2 + 119\lambda_v + 37)}{35(1 + \lambda_v)^2(3\lambda_v^2 + 3\lambda_v + 1)}\,d\lambda_v \quad (7)$$

where $\xi = (v_w/u_1)^2(u_1x/\nu)$ is a nondimensional length. Direct integration of Eq. (7), with the use of the initial condition $\xi = 0$, $\lambda_v = 0$, gives λ_v implicitly as a function of ξ.

$$\xi = \frac{2}{35}\left[12\lambda_v - \frac{10}{1 + \lambda_v} + \frac{9}{2}\ln\frac{(1 + \lambda_v)^2}{(3\lambda_v^2 + 3\lambda_v + 1)} - \frac{35\sqrt{3}}{3}\tan^{-1}\sqrt{3}(2\lambda_v + 1) + \frac{35\sqrt{3}}{3}\tan^{-1}\sqrt{3} + 10\right] \quad (8)$$

The integral form of the energy equation is obtained by integrating Eq. (2), which contains the velocity component u and the temperature T, across the greater (i.e., velocity or thermal) boundary-layer thickness. An assumption that the thermal boundary-layer thickness is greater than the velocity boundary-layer thickness, for the Prandtl Numbers considered in this paper, can be shown to lead to contradictory results; therefore, Eq. (2) is integrated between the limits $y = 0$ and $y = \delta_v$. Use of the equation of continuity and the following boundary conditions: at $y = 0$,

$$u = 0, \quad v = v_w, \quad T = T_w(x)$$

at $y = \delta_v$,

$$u = u_1, \quad v = v(\delta_v), \quad T = T_1, \quad \partial T/\partial y = 0$$

yields

$$(d/dx)\int_0^{\delta_v} uT\,dy - T_1(d/dx)\int_0^{\delta_v} u\,dy + v_w(T_1 - T_w) = -(\nu/P)(\partial T/\partial y)_w \tag{9}$$

A polynomial of the fourth degree as an approximation to the thermal boundary-layer profile satisfying the following boundary conditions: at $y = 0$,

$$T = T_w(x), \quad v_w(\partial T/\partial y)_w = (\nu/P)(\partial^2 T/\partial y^2)_w$$

at $y = \delta_t$,

$$T = T_1, \quad \partial T/\partial y = \partial^2 T/\partial y^2 = 0$$

results in

$$\frac{T}{T_1} = \frac{T_w}{T_1} + \left(1 - \frac{T_w}{T_1}\right)\frac{2}{1+\lambda_t}\eta_t + \left(1 - \frac{T_w}{T_1}\right)\frac{6\lambda_t}{1+\lambda_t}\eta_t^2 - \left(1 - \frac{T_w}{T_1}\right)\frac{2+8\lambda_t}{1+\lambda_t}\eta_t^3 + \left(1 - \frac{T_w}{T_1}\right)\frac{1+3\lambda_t}{1+\lambda_t}\eta_t^4 \tag{10}$$

where $\eta_t = y/\delta_t$; $\lambda_t = Pv_w\delta_t/(6\nu)$; and δ_t and λ_t are the dimensional and nondimensional thermal boundary-layer thicknesses, respectively.

Substituting Eqs. (6) and (10) into Eq. (9) and introducing ξ gives the energy equation in the following form:

$$(\tau F)' = 70P\tau(1 + 3\lambda_t + 3\lambda_t^2)/\lambda_t(1 + \lambda_t) \tag{11}$$

where

$$\tau = 1 - (T_w/T_1) \tag{12}$$

$$F = J^2\lambda_t[P(168 - 27J^2 + 7J^3) + (180 + 252P - 108J + 21J^2 - 45PJ^2 + 12PJ^3)\lambda_t + (288 - 180J + 36J^2)\lambda_t^2]/(1 + \lambda_t)(PJ + \lambda_t) \tag{13}$$

$$J = \delta_t/\delta_v = \lambda_t/P\lambda_v \tag{14}$$

The heat-balance equation [Eq. (4)], with the use of Eq. (10), when nondimensionalized and solved for τ, becomes

$$\tau = 3\lambda_t(1 + \lambda_t)\{[1 - (T_c/T_1)] + (K/P)\tau''\}/(1 + 3\lambda_t + 3\lambda_t^2) \tag{15}$$

where

$$K = \alpha(u_1h/\nu)(v_w/u_1)^3[(1 - r)(k_m/k_g) + r]$$

a constant.

The substitution of Eq. (15) into the right-hand side (only) of Eq. (11) results in an equation that may be immediately integrated once with respect to ξ. Use of the initial condition $\xi = 0$, $\lambda_t = 0$ gives the integrated expression in the following form:

$$\tau' + CF\tau = \tau_0' - (P/K)[1 - (T_c/T_1)]\xi \tag{16}$$

where the subscript 0 refers to conditions at $\xi = 0$. Eq. (16) replaces the original heat-balance equation [Eq. (15)]. If $F = F(\xi)$ is known, Eq. (16) is an ordinary first-order linear differential equation whose solution, with the initial condition $\xi = 0$, $\tau = \tau_0$, is

$$\tau = \left(\tau_0 + \int_0^{\xi}\{\tau_0' - (P/K)[1 - (T_c/T_1)]\xi\}e^{C\int_0^{\xi} F\,d\xi}\,d\xi\right)\Big/ e^{C\int_0^{\xi} F\,d\xi} \tag{17}$$

From a consideration of Eqs. (8), (13), and (14), it can be shown (assuming J_∞ finite) that the denominator of Eq. (17) is equal to zero at $\xi = \infty$. Therefore, in order to enforce the condition that τ_∞ be finite, it is necessary that the numerator of Eq. (17) vanish at $\xi = \infty$. Thus,

$$\tau_0 = \int_0^{\infty}\left\{(P/K)[1 - (T_c/T_1)]\xi - \tau_0'\right\}e^{C\int_0^{\xi} F\,d\xi}\,d\xi \tag{18}$$

Eq. (18) shows that the boundary conditions for temperature and temperature gradient at the leading edge of the plate—namely, τ_0 and τ_0'—are related to each other mathematically and cannot both be arbitrarily chosen.

From Eqs. (8), (11), and (14) at $\xi = \infty$, one obtains $J_\infty = 1$—i.e., the velocity and thermal boundary-layer thicknesses are equal. The application of L'Hôspital's rule to Eq. (17) at infinity then gives

$$\tau_\infty \equiv [1 - (T_w/T_1)]_\infty = 1 - (T_c/T_1)$$

Thus, the reasonable physical result is obtained that the wall temperature approaches the coolant temperature at infinity.

The thermal boundary-layer thickness and the temperature distribution along the plate are obtained by the numerical solution of two simultaneous first-order nonlinear ordinary differential equations. One of these equations is the replaced heat-balance equation [Eq. (16)]. The other is obtained by differentiating the energy equation [Eq. (11)].

$$(\lambda_t^2)' = \frac{2(1 + \lambda_t)(PJ + \lambda_t)^2}{J^2\Theta}\left[70P(1 + 3\lambda_t + 3\lambda_t^2) + \frac{PJ^3\Phi\lambda_t\lambda_v'}{(1 + \lambda_t)(PJ + \lambda_t)^2} - \frac{J^2\lambda_t^2\Psi\tau'}{\tau(PJ + \lambda_t)}\right] \tag{19}$$

where

$$\Psi(\lambda_t,J) = P(168 - 27J^2 + 7J^3) + (180 + 252P - 108J + 21J^2 - 45PJ^2 + 12PJ^3)\lambda_t + (288 - 180J + 36J^2)\lambda_t^2$$

$$\Theta(\lambda_t,J) = [336P^2J - 108P^2J^3 + 35P^2J^4] + [336P + (540P + 924P^2)J - 540PJ^2 + (140P - 306P^2)J^3 + 100P^2J^4]\lambda_t + [(540 + 924P) + (-432 + 1{,}512P + 504P^2)J + (105 - 1{,}530P)J^2 + (400P - 180P^2)J^3 + 60P^2J^4]\lambda_t^2 + [(1{,}512 + 504P) + (-1{,}224 + 864P)J + (300 - 900P)J^2 + 240PJ^3]\lambda_t^3 + [864 - 720J + 180J^2]\lambda_t^4$$

$$\Phi(\lambda_t,J) = [168P^2J - 81P^2J^3 + 28P^2J^4] + [336P + (180P + 420P^2)J - 324PJ^2 + (98P - 216P^2)J^3 + 76P^2J^4]\lambda_t + [(360 + 840P) + (-324 + 468P + 252P^2)J + (84 - 864P)J^2 + (266P - 135P^2)J^3 + 48P^2J^4]\lambda_t^2 + [(936 + 504P) + (-864 + 288P)J + (228 - 540P)J^2 + 168PJ^3]\lambda_t^3 + [576 - 540J + 144J^2]\lambda_t^4$$

The numerical solution starts at the leading edge; therefore, $(\lambda_t^2)_0'$ must be determined. From Eqs. (7) and (19), assuming J_0' finite, it is found that

$$(\lambda_t^2)_0' = (35/37)P^2J_0^2 \tag{20}$$

where J_0 depends on the boundary conditions τ_0 and τ_0'. Reference to Eq. (18) indicates that three different combinations of τ_0 and τ_0' are possible: (a) $\tau_0 = 0$, $\tau_0' \neq 0$; (b) $\tau_0 \neq 0$, $\tau_0' = 0$; and (c) $\tau_0 \neq 0$, $\tau_0' \neq 0$. However, the condition $\tau_0 = 0$ appears to imply physically that the thermal boundary-layer thickness is zero at the leading edge [i.e., $(\lambda_t)_0 = 0$].

From a consideration of Eqs. (7), (11), and (16), there results the following equation for J_0 in case (a):*

$$J_0^3(7J_0^3 - 27J_0^2 + 168) - [148/(3P)] = 0 \tag{21}$$

Solution of the Problem Neglecting Plate Thermal Conductivity

When plate thermal conductivity is neglected, the original heat-balance equation [Eq. (15)] assumes a simplified form,

$$\tau = 3[1 - (T_c/T_1)]\lambda_t(1 + \lambda_t)/(1 + 3\lambda_t + 3\lambda_t^2) \tag{22}$$

The elimination of τ from Eq. (11) results in an expression that can be immediately integrated with respect to ξ. Use of the initial condition $\xi = 0$, $\lambda_t = 0$ gives

$$\{J^2\lambda_t^2[P(168 - 27J^2 + 7J^3) + (180 + 252P - 108J + 21J^2 - 45PJ^2 + 12PJ^3)\lambda_t + (288 - 180J + 36J^2)\lambda_t^2]/(1 + 3\lambda_t + 3\lambda_t^2)(PJ + \lambda_t)\} - 70P\xi = 0 \tag{23}$$

* For cases (b) and (c) one would find $J_0^3(7J_0^3 - 27J_0^2 + 168) - (148/P) = 0$.

The solution of the algebraic equation is obtained graphically. A value of λ_v is specified thereby, from Eq. (8), giving the corresponding ξ. Then a graph of Eq. (23) vs. λ_t for arbitrarily assumed values of λ_t will indicate the correct λ_t for the value of λ_v specified. Recourse to Eq. (22) yields the corresponding wall temperature.

At the leading edge, the equation defining J_0 is obtained from Eqs. (7) and (23) and is

$$J_0^3(7J_0^3 - 27J_0^2 + 168) - (74/P) = 0 \tag{24}$$

Also, at the leading edge, as $(\lambda_t)_0 = 0$, Eq. (22) indicates that $\tau_0 = 0$, while, from a consideration of Eqs.

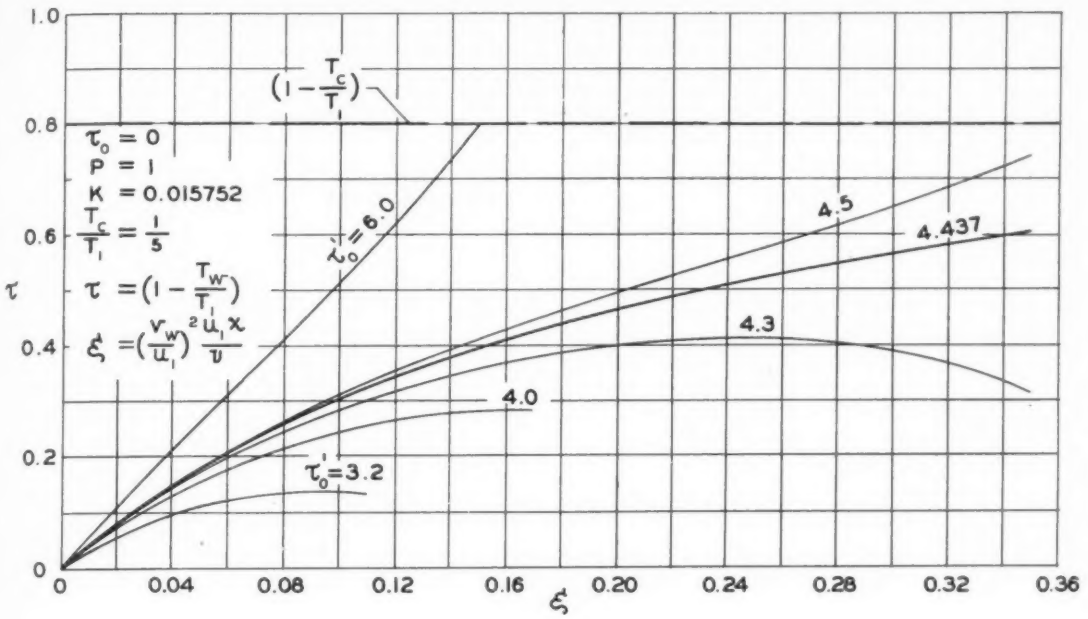

FIG. 2 DETERMINATION OF τ_0' FOR $\frac{v_w}{u_1} = 0.001$

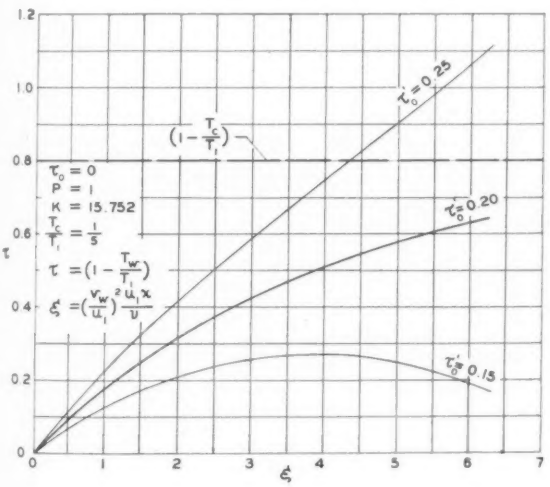

FIG. 3 DETERMINATION OF τ_0' FOR $\frac{v_w}{u_1} = 0.01$

(7) and (22) and use of the conditions that J_0 and J_0' be finite, it is found that $\tau_0' = \infty$.

This infinite temperature gradient at the leading edge of the plate, when axial plate thermal conductivity is neglected, is in agreement with results obtained by previous investigators—e.g., Grootenhuis and Moore[2] and Yuan.[3] Grootenhuis and Moore, however, considered thermal conductivity across the plate. Their results give the axial temperature distribution for various injection ratios but with an infinite gradient at the leading edge. Yuan neglected wall thermal conductivity entirely and assumed that the wall temperature is constant. His results give an "average" wall temperature for varying lengths of plate. For example, for a sweat-cooled plate of length L whose free-stream Reynolds Number $(u_1 L/\nu) = 200{,}000$, Yuan's method states that T_w/T_1 will be constant all along the plate and will be equal to 0.616 when $v_w/u_1 = 0.001$ and $P = 1$ (see Fig. 5).

At infinity, from Eq. (22), $\tau_\infty = 1 - (T_c/T_1)$ while, from Eqs. (8) and (23), $J_\infty = 1$. These results are identical to those obtained for the complete heat-balance equation and indicate that results at infinity are independent of wall thermal conductivity.

Numerical Solution of the Problem

When wall thermal conductivity is neglected, the simplified heat-balance equation gives $\tau_0 = 0$, $\tau_0' \neq 0$. Therefore, a solution of the general problem will be obtained for case (a)—i.e., $\tau_0 = 0$, $\tau_0' \neq 0$—so that the effect of axial thermal conductivity on the wall temperature distribution may be determined.

Physical data assumed are $P = 1$, $T_c/T_1 = 1/5$, $v_w/u_1 = 0.001$ and 0.01, $r = 1/4$, $h = 1/4$ in., $u_1 = 100$ ft. per sec., $\nu = 1/6{,}000$ sq.ft. per sec., $\alpha = 1/2$, $k_m/k_g = 3{,}360$. For these values, $K = 0.015752$ and 15.752 for $v_w/u_1 = 0.001$ and 0.01, respectively.

To calculate the temperature distribution along the plate, it is necessary that τ_0' be uniquely determined. Eq. (18) defines τ_0' in terms of F, but $F(\xi)$ cannot be

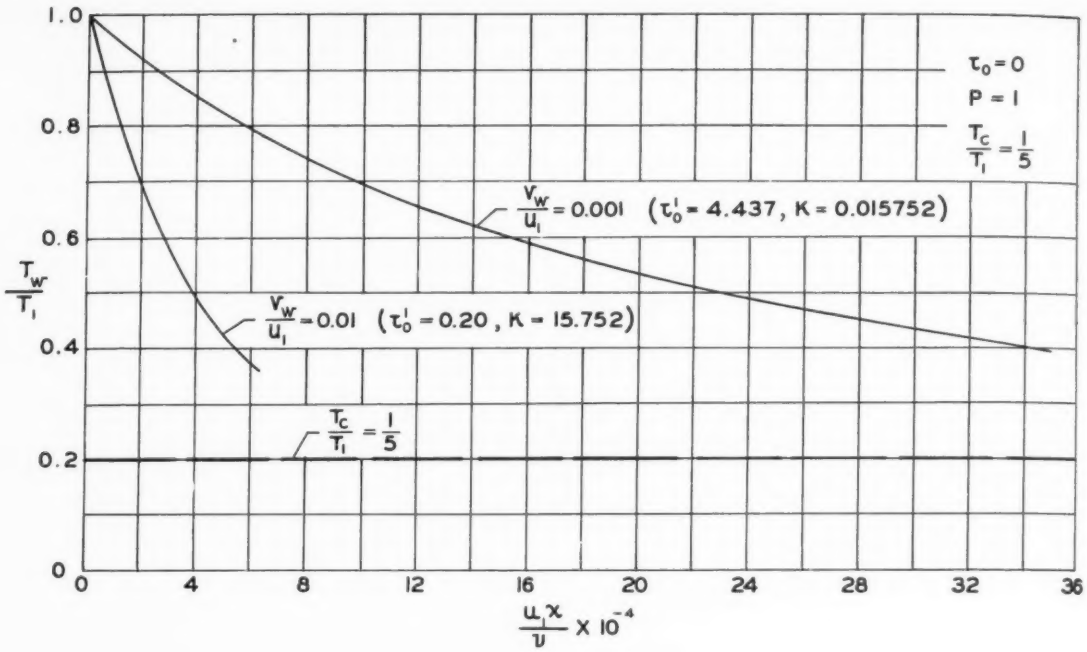

FIG. 4 TEMPERATURE DISTRIBUTION ALONG POROUS PLATE
THERMAL CONDUCTIVITY OF PLATE MATERIAL CONSIDERED

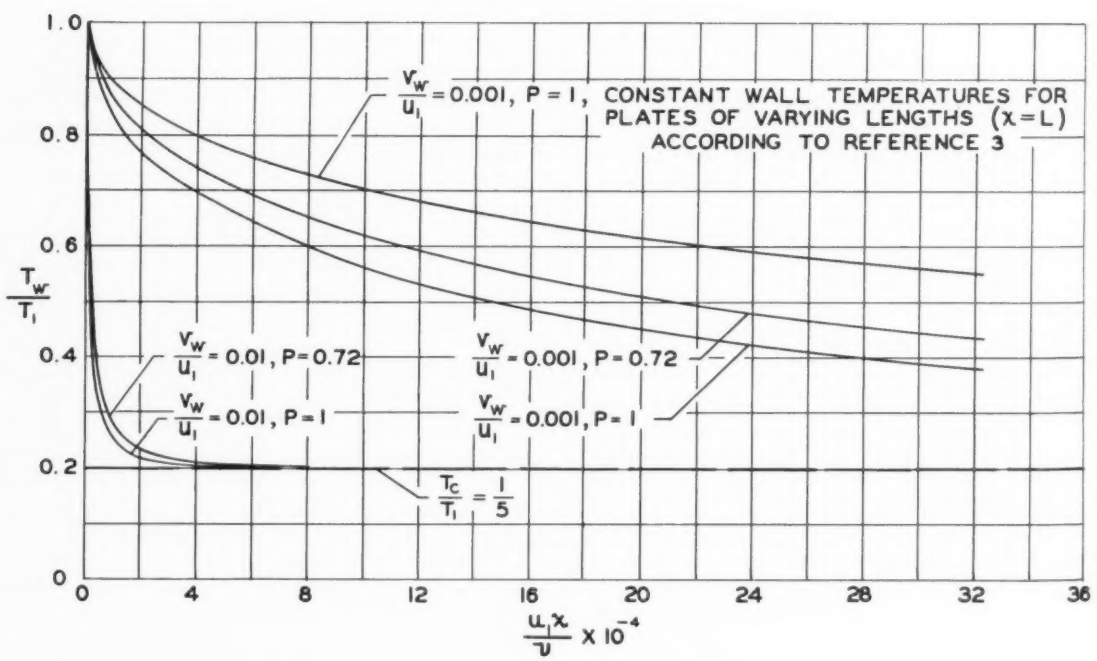
1.0
0.8
0.6
0.4
0.2
0
$\frac{T_w}{T_1}$
$\frac{V_w}{u_1} = 0.001$, $P = 1$, CONSTANT WALL TEMPERATURES FOR PLATES OF VARYING LENGTHS $(x = L)$ ACCORDING TO REFERENCE 3
$\frac{V_w}{u_1} = 0.01$, $P = 0.72$
$\frac{V_w}{u_1} = 0.01$, $P = 1$
$\frac{V_w}{u_1} = 0.001$, $P = 0.72$
$\frac{V_w}{u_1} = 0.001$, $P = 1$
$\frac{T_c}{T_1} = \frac{1}{5}$
0 4 8 12 16 20 24 28 32 36
$\frac{u_1 x}{\nu} \times 10^{-4}$

FIG. 5 TEMPERATURE DISTRIBUTION ALONG POROUS PLATE
THERMAL CONDUCTIVITY OF PLATE MATERIAL NOT CONSIDERED

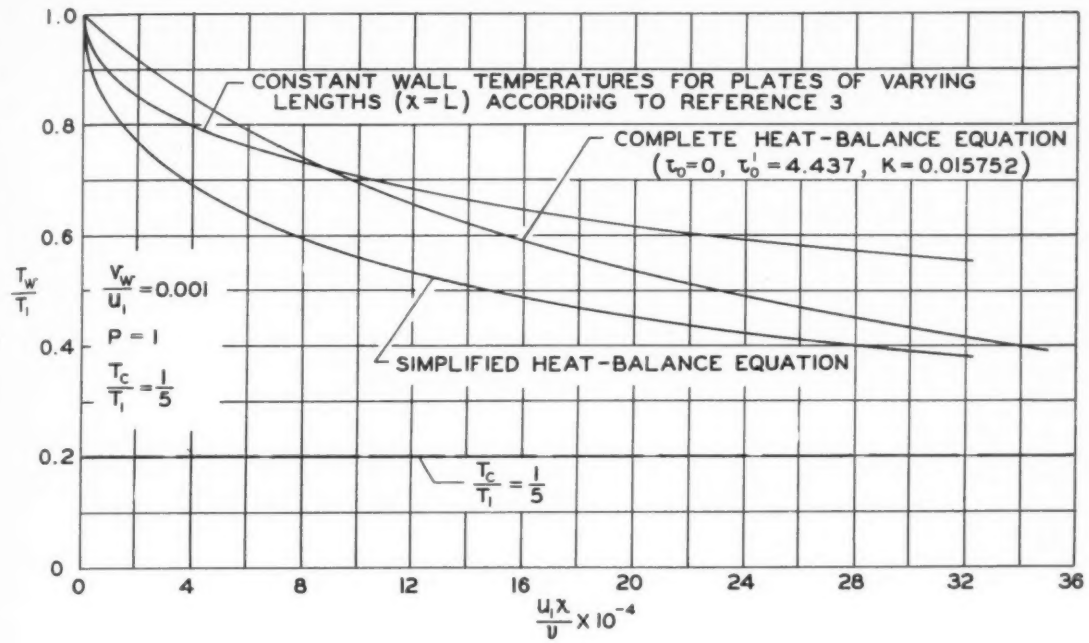

FIG. 6 TEMPERATURE DISTRIBUTION RESULTING FROM VARIOUS HEAT-BALANCE EQUATIONS

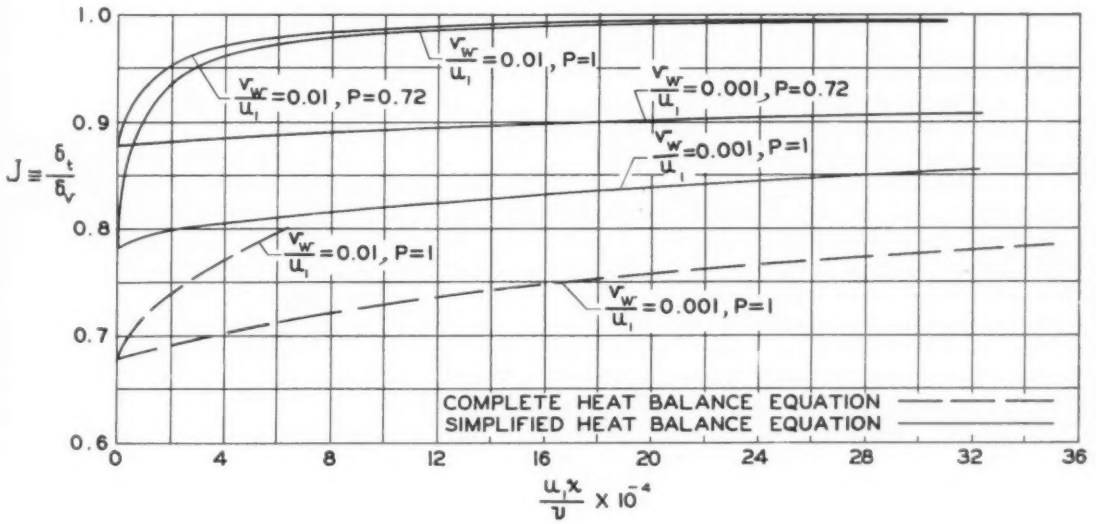

FIG. 7 DISTRIBUTION OF BOUNDARY LAYER THICKNESS RATIO ALONG THE PLATE

obtained until τ_0' is uniquely determined. Therefore, as Eq. (18) cannot be used to evaluate τ_0', arbitrary values must be assumed until a physically possible axial temperature distribution—i.e., approaching the coolant temperature in the downstream direction—is obtained. It can be shown from the numerical calculations that, at any value of ξ, τ is a linear function of τ_0'. This useful result implies that the numerical solution of the differential equations [Eqs. (16) and (19)] need be applied to only two arbitrarily chosen values of τ_0'. Solutions for other values of τ_0' are then obtained by linear interpolation (see Figs. 2 and 3).

The numerical solution is begun at the leading edge. At this point $\lambda_t = 0$, $\lambda_v = 0$ and for case (a), $\tau_0 = 0$, while τ_0' as determined by the above procedure is 4.437 for $v_w/u_1 = 0.001$ and 0.20 for $v_w/u_1 = 0.01$; moreover, from Eq. (21), $J_0 = 0.67877$ for $P = 1$. The increments of ξ used are $\Delta\xi = 0.02$ and 0.2 for $v_w/u_1 = 0.001$ and 0.01, respectively.

Solutions for the simplified heat-balance equation are obtained for $P = 0.72$ and 1 and for $v_w/u_1 = 0.001$ and 0.01. From Eq. (24), $J_0 = 0.878$ and 0.782 for $P = 0.72$ and 1, respectively.

Conclusions

The inclusion of the axial wall thermal conductivity eliminates the infinite temperature gradient at the leading edge of the plate. With wall thermal conductivity considered, the reasonable assumption that the wall temperature at an infinite distance downstream be finite results in a mathematical relationship between the boundary conditions at the leading edge of the plate. Three possible combinations for the boundary conditions at the leading edge exist. For the case considered in this investigation—i.e., the wall-free-stream temperature ratio equal to unity and the temperature gradient not equal to zero—the boundary-layer thickness ratio is less than unity at the leading edge for Prandtl Numbers greater than 0.35 and is equal to unity at an infinite distance downstream; furthermore, at an infinite distance downstream the wall temperature approaches the coolant temperature.

When wall thermal conductivity is neglected, the resulting simplified heat-balance equation gives a wall-free-stream temperature ratio of unity and an infinite temperature gradient at the leading edge. The boundary-layer thickness ratio is less than unity at the leading edge for Prandtl Numbers greater than $^1/_2$. The inclusion or omission of wall thermal conductivity does not affect conditions at infinity since, in both analyses (i.e., complete or simplified heat-balance equation), the boundary-layer thickness ratio is equal to unity and the wall temperature is equal to the coolant temperature at an infinite distance downstream.

Many of the above results are illustrated in the figures. Fig. 4 shows the finite temperature gradient at the leading edge when wall thermal conductivity is considered. The figure also indicates the greater cooling effect of a higher fluid injection ratio; for example, a wall-free-stream temperature ratio of 1/2 will be obtained in approximately one-sixth the distance for the injection ratio of 0.01 as compared with 0.001.

Fig. 5 illustrates the infinite temperature gradient at the leading edge when the plate thermal conductivity is not considered and readily indicates, for the higher fluid injection ratio, the asymptotic tendency of the temperature distribution.

Fig. 6 presents a comparison of the temperature distribution resulting from the use of various heat-balance equations. For the range of local Reynolds Numbers considered and for the physical data assumed for the plate, the complete heat-balance equation indicates a consistently higher wall temperature than the simplified heat-balance equation.

Fig. 7 presents the distribution of the boundary-layer thickness ratio along the plate. It will be noted that at the leading edge the boundary-layer thickness ratio is larger for the simplified heat-balance equation; also, the asymptotic tendency of the boundary-layer thickness ratio is evident from the results of the simplified heat-balance equation for the higher fluid injection ratio. It is interesting to observe that the velocity boundary-layer thickness is here greater than the thermal boundary-layer thickness—contrary to results usually obtained.[4] This is due to the inclusion of the second-order heat-balance differential equation [Eq. (4)], in conjunction with the variable temperature along the plate, into the analysis.

References

[1] Weinbaum, S., and Wheeler, H. L., Jr., *Heat Transfer in Sweat Cooled Porous Metals*, Jet Propulsion Lab., California Institute of Technology, Pasadena, Calif., Progress Report No. 1-58, April, 1947.

[2] Grootenhuis, P., and Moore, N. P. W., *Some Observations on the Mechanism of Sweat Cooling*, 7th International Congress of Applied Mechanics, London, 1948.

[3] Yuan, S. W., *A Theoretical Investigation of the Temperature Field in the Laminar Boundary Layer on a Porous Flat Plate with Fluid Injection*, U.S. Navy, Project Squid, Technical Report No. 4, September, 1947.

[4] Goldstein, S., *Modern Developments in Fluid Dynamics*, Vol. II; Oxford University Press, 1938.

The Aerodynamic Forces on Low Aspect Ratio Wings Oscillating in an Incompressible Flow

H. R. LAWRENCE* AND E. H. GERBER†

Cornell Aeronautical Laboratory, Inc.

SUMMARY

A method for calculating the aerodynamic forces acting on a harmonically oscillating low aspect ratio wing in incompressible flow is presented for the class of plan forms with straight trailing edges. The aerodynamic lift and moment resulting from oscillatory vertical translation and rotation are computed for rectangular and triangular wings of aspect ratios ranging from 0 to 4 with reduced frequencies from zero to unity. The aerodynamic forces arising from the harmonic rotation of 25, 37, and 50 per cent chord trailing-edge flaps are computed for rectangular wings of aspect ratios 1 and 2 for the zero to unity reduced frequency range. The results are shown to be in accord with the Garrick theory for plan forms of very low aspect ratio and with the infinite aspect ratio theory for rectangular wings. In the limiting case of zero frequency, the results reduce to the steady-state solutions of reference 9. A rapid method for solving the integral equation is developed for cases where the steady-state solution has been expressed in matrix form.

INTRODUCTION

THE DEVELOPMENT OF METHODS for calculating the aerodynamic forces acting on an oscillating wing of finite span in an inviscid incompressible flow has occupied the attention of numerous investigators. Theoretical developments and calculations for high aspect ratio wings have been presented by Cicala,[1] Borbely,[2] Küssner,[3] Jones,[4] Reissner,[5] and others. An extension of the Jones low aspect ratio theory[6] to nonstationary flow was presented recently by Garrick.[7] The oscillating wing of circular plan form was treated by Schade and Krienes[8] by a natural extension of the known steady-state solution. However, the writers have been unable to find any reference to the subject of nonsteady flow for low aspect ratio wings (say, aspect ratio from 1 to 3) with straight trailing edges.

The starting point for the present investigation is the exact two-variable integral equation for an oscillating lifting surface in a linearized incompressible flow. An approximate single variable integral equation for low aspect ratio wings with straight trailing edges in steady flow was obtained from this two-variable integral equation in reference 9. Solutions of this single-variable integral equation have been shown to agree with wind-tunnel test data for small angles of attack. The two-variable integral equation for an oscillating wing will be simplified by using the same type of approximation as in reference 9 to obtain a single-variable integral equation for an oscillating wing.

As in the stationary case, the result will be applicable only to wings with straight trailing edges. The integral equation will be solved by an extension of the method of reference 9.

Received March 6, 1952.

* Assistant Head, Aerodynamics Research Department.

† Associate Research Physicist.

LIST OF SYMBOLS

x, y, z	= Cartesian coordinates of the point of observation
ξ, η	= Cartesian coordinates of source point
U	= free-stream velocity
ω	= frequency of oscillation
k	= $\omega c/U$ reduced frequency
$2b$	= wing span
$2\beta(x)$	= local wing span
$2c$	= wing chord
ρ	= free-stream density
A.R.	= aspect ratio
$\phi(x, y)$	= perturbation velocity potential on the upper surface of the airfoil
$u(x, y)$	= $\phi_x(x, y)$
$z = h(x, y)$	= equation of the mean camber surface of the airfoil at maximum displacement
$-w(x, y)$	= $ikh(x, y) + h_x(x, y)$ = local slope of airfoil in stream direction
dL/dS	= lift per unit area [see Eq. (3)]
dL/dx	= lift per unit chord [see Eq. (13)]
$f(x)$	= [see Eq. (4)]
$g(x)$	= [see Eq. (11)]
$2\rho U^2 m'(x)$	= rolling moment per unit chord [see Eq. (17)]
$2\rho U^2 e'(x)$	= rolling moment for extremely low aspect ratio wing [see Eq. (16)]
$g_s(x)$	= [see Eq. (20)]
$\mu(k)$	= [see Eq. (21)]
$S^*(x, \beta)$, $R(x, \beta)$, $P(x, k, b)$	= [see Eqs. (23), (24), and (25)]
G_r	= [see Eqs. (26) and (27)]
$\bar{F}$	= [see Eq. (27)]; the $\bar{F}$ are the F of reference 9
$M(x, k, b)$, $N(k, b)$	= [see Eqs. (44) and (45)]
F, G, H, T, A	= matrices defined by Eqs. (32)
Q, J	= matrices defined by Eq. (34)

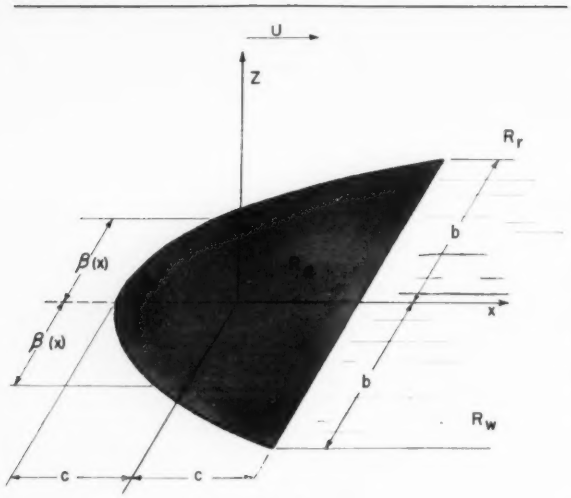

FIG. 1.

$L_h = \frac{1}{2b}\int_{-b}^{b} L_h'\,dy$†

$M_h = \frac{1}{2b}\int_{-b}^{b} M_h'\,dy$†

$L_\alpha = \frac{1}{2b}\int_{-b}^{b} L_\alpha'\,dy$†

$B(x, k)$ = [see Eq. (47)]

Ci, Si = cosine and sine integrals (see reference 14)

Subscripts x, y, or z denote partial differentiation with respect to x, y, or z.

(I) The Integral Equation for a Lifting Surface in Unsteady Flow

Determination of the aerodynamic forces acting on a wing of finite span oscillating in an incompressible linearized flow has been clearly and rigorously formulated as the solution of an integral equation by Reissner.[5] A slight modification of the Reissner result will be used as the basis for further development.

Consider a thin wing oscillating harmonically about the plane $z = 0$ in a free stream of velocity U directed along the positive x axis. Here, x, y, z are a left-handed set of Cartesian coordinates with the y axis spanwise and the z axis normal to the wing, as illustrated in Fig. 1. The z coordinate of the mean camber surface is given at any instant by the real part of the expression $h(x, y)e^{i\omega t}$. On the plane $z = 0^+$, the vertical perturbation velocity $U\phi_z(x, y)$ may be expressed in terms of $Uu(x, y)$, the streamwise perturbation velocity, as follows:[9]

$$\phi_z(x, y) = -\frac{1}{2\pi}\frac{\partial}{\partial y}\int_\infty\int \frac{d\xi\, d\eta u(\xi, \eta)}{y - \eta}\left(1 + \frac{r}{x - \xi}\right) \tag{1}$$

where $r = \sqrt{(x - \xi)^2 + (y - \eta)^2}$ and the integration is taken over the entire plane $z = 0$. It will be noted that Eq. (1) is applicable to the case of a wing with swept leading edge.

Boundary conditions on the plane $z = 0^+$ are given in Eqs. (49), (54), and (55) of reference 5 as follows:

$$\begin{aligned} \phi_z(x, y) &= ikh(x, y) + h_x(x, y) && \text{on } R_a \\ \phi(x, y) &= 0 && \text{on } R_r \\ \phi(x, y) &= \phi(1, y)e^{-ik(x-1)} && \text{on } R_w \end{aligned}$$

where the regions R_a, R_w, and R_r represent, respectively, the airfoil, the wake, and the remainder of the plane $z = 0$ (see Fig. 1). Upon substituting these boundary conditions in Eq. (1) with the following definition for $w(x, y)$, there results the equation

$$w(x, y) = \frac{1}{2\pi}\frac{\partial}{\partial y}\int_{-1}^{1} d\xi \int_{-\beta(\xi)}^{\beta(\xi)} \frac{d\eta u(\xi, \eta)}{y - \eta}\left(1 + \frac{r}{x - \xi}\right) - \frac{ik}{2\pi}\frac{\partial}{\partial y}\int_1^\infty d\xi \int_{-b}^{b} \frac{d\eta\phi(1, \eta)e^{-ik(\xi-1)}}{y - \eta}\left(1 + \frac{r}{x - \xi}\right) \tag{2}$$

where

$$-w(x, y) = ikh(x, y) + h_x(x, y) \tag{2.1}$$

The lift per unit area is given by the expression[9]

$$dL/dS = 2\rho U^2(\phi_x + ik\phi) \tag{3}$$

where ϕ and ϕ_x are evaluated on the $z = 0^+$ plane. The Kutta condition is satisfied if the lift per unit area vanishes at the trailing edge $x = 1$. Eqs. (2) and (3) and the Kutta condition represent a convenient mathematical formulation of the problem.

(II) Development of an Approximate Integral Equation in One Variable

A single-variable integral equation will be obtained from the two-variable integral equation [Eq. (2)] by the same process as that used in reference 9. For a symmetric spanwise lift distribution, the integral Eq. (2) is multi-

† The aerodynamic force coefficients per unit span L_h', M_h', L_α', etc., are defined as in *A.A.F. T.R. 4798*.

plied by a weighting factor $\sqrt{\beta^2(x) - y^2}$ and integrated over the span. It will be observed that no assumption has been made regarding the spanwise lift distribution. The integral equation is to be satisfied on the average in the spanwise direction, and the weighting factor merely determines the relative importance assigned to various spanwise locations. The weighting factor $\sqrt{\beta^2 - y^2}$ was shown by Flax[20] to be consistent with the variational approach to wing theory and leads to an exact result in the limiting case of low aspect ratio.

With the definition

$$f(x) = \int_{-\beta(x)}^{\beta(x)} dy\, w(x, y)\, \sqrt{\beta^2(x) - y^2} \tag{4}$$

the following result is obtained:

$$f(x) = \frac{1}{2\pi} \int_{-\beta(x)}^{\beta(x)} dy\, \sqrt{\beta^2(x) - y^2}\, \frac{\partial}{\partial y} \int_{-1}^{1} d\xi \int_{-\beta(\xi)}^{\beta(\xi)} \frac{d\eta u(\xi, \eta)}{y - \eta} \left(1 + \frac{r}{x - \xi}\right) - \frac{ik}{2\pi} \int_{-\beta(x)}^{\beta(x)} dy\, \sqrt{\beta^2(x) - y^2}\, \frac{\partial}{\partial y} \int_{1}^{\infty} d\xi e^{-ik(\xi - 1)} \int_{-b}^{b} \frac{d\eta \phi(1, \eta)}{y - \eta} \left(1 + \frac{r}{x - \xi}\right)$$

After integrating by parts with respect to y and interchanging orders of integration, the above equation may be written in the form

$$f(x) = \frac{1}{2\pi} \int_{-1}^{1} d\xi \int_{-\beta(\xi)}^{\beta(\xi)} d\eta u(\xi, \eta) J_s - \frac{ik}{2\pi} \int_{1}^{\infty} d\xi e^{-ik(\xi - 1)} \int_{-b}^{b} d\eta \phi(1, \eta) J_u \tag{5}$$

where J_s and J_u are defined as follows:

$$J_s = \int_{-\beta(x)}^{\beta(x)} \frac{dyy}{(y - \eta)\sqrt{\beta^2(x) - y^2}} \left(1 + \frac{r}{x - \xi}\right); \quad -\beta(\xi) < \eta < \beta(\xi) \tag{6}$$

$$J_u = \int_{-\beta(x)}^{\beta(x)} \frac{dyy}{(y - \eta)\sqrt{\beta^2(x) - y^2}} \left(1 + \frac{r}{x - \xi}\right); \quad -b < \eta < b \tag{7}$$

The integral J_s may be approximated by the expression[9]

$$J_s = \frac{\pi}{2}\left(1 + \frac{|x - \xi|}{x - \xi}\right) + \frac{\pi}{2}\left(1 + \frac{\sqrt{(x - \xi)^2 + \beta^2(x)}}{x - \xi}\right) \tag{8}$$

The result of using this approximation is an integral equation for low aspect ratio wings in steady flow. This theory is known to be in good agreement with experiment for a sufficiently small range of angle of attack. By making use of this same approximation, the integral equation for unsteady flow will reduce to this known steady-state solution as the frequency goes to zero. Since the integral defined as J_u in Eq. (7) is of the same form as J_s defined in Eq. (6), it seems reasonable to use the approximation

$$J_u = \frac{\pi}{2}\left(1 + \frac{|x - \xi|}{x - \xi}\right) + \frac{\pi}{2}\left(1 + \frac{\sqrt{(x - \xi)^2 + b^2}}{x - \xi}\right) \tag{9}$$

Upon substituting the values of J_s and J_u given by Eqs. (8) and (9) in Eq. (5), the following equation is obtained:

$$f(x) = \frac{1}{4} \int_{-1}^{1} d\xi \int_{-\beta(\xi)}^{\beta(\xi)} d\eta u(\xi, \eta) \left[1 + \frac{|x - \xi|}{x - \xi} + 1 + \frac{\sqrt{(x - \xi)^2 + \beta^2(x)}}{x - \xi}\right] - \frac{ik}{4} \int_{1}^{\infty} d\xi e^{-ik(\xi - 1)} \int_{-b}^{b} d\eta \phi(1, \eta) \left[1 + \frac{|x - \xi|}{x - \xi} + 1 + \frac{\sqrt{(x - \xi)^2 + b^2}}{x - \xi}\right] \tag{10}$$

By making use of the definition

$$g(x) = \int_{-\beta(x)}^{\beta(x)} dy \phi(x, y) \tag{11}$$

Eq. (10) may be simplified to the form

$$f(x) = \frac{1}{2} g(x) + \frac{1}{4} \int_{-1}^{1} d\xi g'(\xi) \left[1 + \frac{\sqrt{(x - \xi)^2 + \beta^2(x)}}{x - \xi}\right] - \frac{ik}{4} g(1) \int_{1}^{\infty} d\xi e^{-ik(\xi - 1)} \left[1 + \frac{\sqrt{(x - \xi)^2 + b^2}}{x - \xi}\right] \tag{12}$$

The aerodynamic forces may be expressed in terms of the function $g(x)$ by integrating Eq. (3) across the span.

$$\int_{-\beta(x)}^{\beta(x)} dy \frac{dL}{dS} = \frac{dL}{dx} = 2\rho U^2 (g'(x) + ikg(x)) \tag{13}$$

where dL/dx represents the lift per unit chord. The Kutta condition can no longer be satisfied at all points along the trailing edge. However, an integrated Kutta condition may still be imposed. The total lift per unit chord will be required to vanish at the trailing edge or

$$g'(1) + ikg(1) = 0 \tag{14}$$

Eqs. (4), (12), (13), and (14) represent the mathematical formulation of an approximate theory for oscillating low aspect ratio wings with symmetric lift distribution.

(III) The Single-Variable Equation for an Antisymmetric Lift Distribution

If the function $h(x, y)$ is antisymmetric in y, the lift per unit area will also be antisymmetric and the function $g(x)$ will be identically zero. However, by multiplying Eq. (2) by the weighting factor $-(1/2)y\sqrt{\beta^2(x) - y^2}$, integrating over the span, and approximating the integral on the right-hand side as in Section (II), there results the following equation:

$$e(x) = \frac{1}{2}m(x) + \frac{1}{4}\int_{-1}^{1} d\xi m'(\xi)\left[1 + \frac{\sqrt{(x-\xi)^2 + \beta^2(x)}}{x-\xi}\right] - \frac{ik}{4}m(1)\int_{1}^{\infty} d\xi e^{-ik(\xi-1)}\left[1 + \frac{\sqrt{(x-\xi)^2 + b^2}}{x-\xi}\right] \tag{15}$$

where the functions $e(x)$ and $m(x)$ are defined as follows:

$$e(x) = -\frac{1}{2}\int_{-\beta(x)}^{\beta(x)} dyyw(x, y)\sqrt{\beta^2(x) - y^2} \tag{16}$$

$$m(x) = \int_{-\beta(x)}^{\beta(x)} dyy\phi(x, y) \tag{17}$$

The Kutta condition is satisfied approximately as a weighted average by the expression

$$m'(x) + ikm(x) = 0 \tag{18}$$

TABLE I

AERODYNAMIC COEFFICIENTS FOR RECTANGULAR WINGS

AR	k	L_h	M_h	L_α	M_α
.25	.25	.216 - .4991	.109 + .1861	-1.888 - 1.5521	.856 - .9401
.25	.50	.219 - .2491	.110 + .0961i	-..389-- .7811	.301 - .4691
.25	1.00	.218 - .1241	.109 + .0467i	-..0155- .3891	.158 - .2351
.50	.125	.367 - 1.9681	.197 + .5161	-15.570 - 5.4511	4.547 - 3.1481
.50	.25	.372 - .9831	.189 + .2731	-3.750 - 2.7461	1.270 - 1.5831
.50	.50	.375 - .4901	.190 + .1371	- .795 - 1.3771	.450 - .7921
.50	1.00	.376 - .2441	.189 + .0681	- .056 - .6881	.245 - .3961
1.00	.125	.530 - 3.7021	.292 + .6141	-29.384 - 8.5541	5.162 - 4.6941
1.00	.25	.542 - 1.8411	.294 + .3041	-7.117 - 4.3171	1.468 - 2.3511
1.00	.50	.551 - .9091	.291 + .1501	-1.560 - 2.1621	.550 - 1.1731
1.00	1.00	.563 - .4461	.290 + .0746i	- .173 - 1.0831	.322 - .5861
2.00	.125	.513 - 6.2001	.396 + .4981	-49.485 -10.8131	4.302 - 6.1321
2.00	.25	.560 - 3.0301	.392 + .2501	-11.951 - 5.5181	1.314 - 3.0551
2.00	.50	.630 - 1.4491	.384 + .1191	-2.655 - 2.8271	.547 - 1.5171
2.00	1.00	.698 - .6861	.380 + .0572i	- .369 - 1.4401	.363 - .7581
4.00	.125	.064 - 8.8371	.460 + .3361	-71.102 - 9.6851	3.050 - 7.0771
4.00	.25	.301 - 4.1521	.451 + .1581	-16.763 - 5.5081	.991 - 3.5161
4.00	.50	.570 - 1.8871	.434 + .0721	-3.652 - 3.0991	.483 - 1.7281
4.00	1.00	.755 - .8661	.436 + .0342i	- .549 - 1.6541	.371 - .8691

The functions $e(x)$ and $m(x)$ may be interpreted through the defining Eqs. (16) and (17). Thus, $2\rho U^2 e'(x)$ represents the rolling moment per unit chord for a wing of extremely low aspect ratio and $2\rho U^2 m'(x)$ represents the corresponding quantity for a wing of low aspect ratio. It will be noted that Eq. (15) becomes identical with Eq. (12) when $f(x)$ and $g(x)$ are substituted for $e(x)$ and $m(x)$. Hence, most of the numerical labor required to solve Eq. (12) need not be repeated in solving Eq. (15). For the case of vanishing frequency, the integral Eq. (15) reduces to the steady-state integral Eq. (47) of reference 9. A comparison of calculated results with test data for the steady state[9] appears to show satisfactory agreement.

(IV) Solution of the Integral Equation

The integral Eq. (12) will be solved by expanding $g(x)$ in a series of N terms, with N arbitrary constants. A collocation at N points will be used to determine the arbitrary constants.

A series expansion of $g(x)$ which satisfies the Kutta-Joukowsky condition and vanishes at the leading edge is

$$g(x) = g_s(x) - \mu(k)g_s(1)(1 + x) \tag{19}$$

where $g_s(x)$ is a point function defined as the series:[9]

$$g_s(\theta) = (\pi - \theta)(A_0 + A_1) + \sum_{r=1}^{N-1}(A_{r-1} - A_{r+1})\frac{\sin r\theta}{r} \tag{20}$$

The angle θ was introduced by the substitution $x = \cos\theta$. The function $\mu(k)$ is defined as:

$$\mu(k) = \frac{ik}{2ik + 1} = \frac{2k^2 + ik}{4k^2 + 1} \tag{21}$$

TABLE II

AERODYNAMIC COEFFICIENTS FOR TRIANGULAR WINGS

R	k	L_h	M_h	L_α	M_α
.50	.25	.134 - .8904	.126 - .5781	-3.437 - 1.7911	-2.578 - 1.7331
.50	.50	.135 - .4441	.126 - .3391	- .765 - .8981	- .543 - .8661
.50	1.00	.136 - .2221	.127 - .1691	- .097 - .4491	- .0335- .4321
1.00	.125	.205 - 3.2221	.194 - 2.2791	-25.609 - 6.0191	-18.038 - 5.5551
1.00	.25	.214 - 1.6081	.200 - 1.1401	-6.256 - 3.0421	-4.357 - 2.8001
1.00	.50	.219 - .8001	.199 - .5681	-1.116 - 1.5251	- .935 - 1.3971
1.00	1.00	.221 - .3951	.199 - .2821	- .208 - .7591	- .0798- .6951
2.00	.125	.264 - 5.4731	.271 - 3.4551	-43.641 - 9.0821	-27.385 - 8.0691
2.00	.25	.264 - 2.7181	.274 - 1.7271	-10.702 - 4.5961	-6.651 - 4.0431
2.00	.50	.279 - 1.3341	.270 - .8591	-2.480 - 2.2951	-1.464 - 2.0081
2.00	1.00	.303 - .6421	.274 - .4191	- .422 - 1.1381	- .160 - .9951
4.00	.125	.0481- 8.4891	.357 - 4.5701	-68.097 -11.0151	-36.242 -10.5231
4.00	.25	.116 - 4.1351	.339 - 2.2941	-16.636 - 5.6431	-8.876 - 5.1981
4.00	.50	.221 - 1.9561	.328 - 1.1381	-3.877 - 2.8911	-1.995 - 2.5591
4.00	1.00	.332 - .8941	.331 - .5461	- .722 - 1.4521	- .256 - 1.2581

TABLE III

AERODYNAMIC COEFFICIENTS FOR RECTANGULAR WINGS OF ASPECT RATIO 1 WITH FLAPS

% Chord Flap	k	L_h	M_h	L_β	M_β
25	.125	.0886- 2.7581	.119 - 1.9921	-22.057 - 1.6961	-15.911 - 1.8691
25	.25	.0982- 1.3711	.120 - .9971	-5.476 - .8841	- 3.966 - .9401
25	.50	.105 - .6771	.118 - .5001	-1.342 - .4521	- .978 - .4661
25	1.00	.114 - .3321	.117 - .2501	- .316 - .2321	- .230 - .2321
37	.125	.155 - 3.1581	.180 - 1.8481	-25.216 - 2.9931	-11.720 - 2.8021
37	.25	.166 - 1.5701	.181 - .9261	-6.231 - 1.5361	-3.636 - 1.4071
37	.50	.174 - .7551	.179 - .4641	-1.496 - .7771	- .864 - .7001
37	1.00	.184 - .3801	.178 - .2331	- .320 - .3951	- .169 - .3491
50	.125	.246 - 3.3421	.227 - 1.3041	-26.649 - 4.5341	-10.322 - 3.6531
50	.25	.258 - 1.6621	.228 - .6541	-6.554 - 2.3071	-2.502 - 1.8341
50	.50	.266 - .8201	.226 - .3281	-1.542 - 1.1611	- .546 - .9131
50	1.00	.276 - .4021	.225 - .1651	- .295 - .5851	- .0549- .4561

TABLE IV

AERODYNAMIC COEFFICIENTS FOR RECTANGULAR WINGS OF ASPECT RATIO 2 WITH FLAPS

% Chord Flap	k	L_h	M_h	L_β	M_β
25	.125	-.00304- 4.1711	.153 - 2.4401	-33.397 - 1.4071	-19.489 - 2.3071
25	.25	..0288 - 2.0381	.151 - 1.2241	-8.171 - .8141	-4.868 - 1.1451
25	.50	.0763 - .9741	.146 - .6351	-1.954 - .4871	-1.204 - .5651
25	1.00	.122 - .4611	.143 - .3091	- .450 - .2801	- .284 - .2801
37	.125	.0626 - 4.9001	.230 - 2.3361	-39.217 - 3.1141	-18.608 - 3.4861
37	.25	.100 - 2.3941	.227 - 1.1731	-9.573 - 1.6771	-4.609 - 1.7351
37	.50	.156 - 1.1451	.222 - .5901	-2.257 - .9221	-1.101 - .8591
37	1.00	.209 - .5421	.218 - .2971	- .480 - .4981	- .220 - .4271
50	.125	.170 - 5.3151	.293 - 1.7171	-42.522 - 5.2421	-13.592 - 4.5961
50	.25	.211 - 2.6121	.290 - .8641	-10.418 - 2.7391	-3.313 - 2.2891
50	.50	.271 - 1.2421	.284 - .4361	-2.410 - 1.4491	- .735 - 1.1361
50	1.00	.329 - .5881	.280 - .2201	- .472 - .7581	- .0861- .5661

TABLE V

VALUES OF THE FUNCTION $R(x,\beta)$

$$R(x,\beta) = 4 + 2x - \sqrt{(x-1)^2+\beta^2(x)} + \sqrt{(x+1)^2+\beta^2(x)} + \beta \sinh^{-1}\left|\frac{\beta}{x-1}\right| - \beta \sinh^{-1}\left|\frac{\beta}{x+1}\right|$$

This function was evaluated only for the values of β necessary for the rectangular and triangular planforms considered.

x	$\sqrt{3}/2$	1/2	0	-1/2	$-\sqrt{3}/2$
β	$R(x,\beta)$	$R(x,\beta)$	$R(x,\beta)$	$R(x,\beta)$	$R(x,\beta)$
.01675			4.00000		.53492
.03349					.53202
.06250				1.99740	
.06698					.51977
.12500				1.98966	
.13397					.47811
.18750		6.02306			
.23325	7.62278				
.25000	7.64326	6.04132		1.95950	.35674
.37500		6.08829			
.46651	7.96944				
.50000	8.02718	6.15094		1.84901	-.02718
.75000		6.31083			
.93302	8.87945				
1.00000	9.01170	6.50324		1.49676	-1.01170
1.50000		6.94579			
1.86603	11.06452				
2.00000	11.39528	7.42548		.57452	-3.39528
4.00000	16.47678	9.30688	4.00000	-1.30688	-8.47678

Upon substitution of the expansion (19) for $g(x)$ in the integral Eq. (12), the resulting equation can be reduced to the form

$$f(x) = S^*(x,\beta) - (1/4)\mu(k)g_s(1)[R(x,\beta) + P(x,b,k)] \quad (22)$$

where the functions $S^*(x,\beta)$, $R(x,\beta)$, and $P(x,b,k)$ are defined as follows:

$$S^*(x,\beta) = \frac{1}{2}g_s(x) + \frac{1}{4}\int_{-1}^{1} g_s'(\xi)\left[1 + \frac{\sqrt{(x-\xi)^2+\beta^2(x)}}{(x-\xi)}\right] \quad (23)$$

$$R(x,\beta) = 2(1+x) + \int_{-1}^{1} d\xi\left[1 + \frac{\sqrt{(x-\xi)^2+\beta^2(x)}}{(x-\xi)}\right] \quad (24)$$

$$P(x,b,k) = \int_{1}^{\infty} e^{-ik(\xi-1)}\left[1 + \frac{\sqrt{(x-\xi)^2+b^2}}{(x-\xi)}\right] \quad (25)$$

Eq. (22) will be solved by a collocation method, at N points given by $x_n = \cos(n\pi/N)$.

The right-hand side of Eq. (23) is identical in form to the right-hand side of Eq. (43) of reference 9. In this reference, it is shown that, after substitution of a series of the form of Eq. (20) into Eq. (23), the latter can be written as

TABLE VI

VALUES OF THE INTEGRAL M(x,b,k)

$$M(x,b,k) = \int_{x}^{x+\infty} dt\, e^{-ikt}\left\{1 + \frac{kb}{t} - \frac{[t^2 + k^2b^2]}{t}\right\}$$

$$M(x,b,k) = M^*(p,q) = \int_{p}^{\infty} dt\, e^{-it}\left\{1 + \frac{q}{t} - \frac{[t^2 + q^2]}{t}\right\}$$

where p = k(1-x) and q = kb. For convenience the integral is tabulated as a function of the two variables p and q, rather than the three variables, x, b, and k.

REAL PART

P \ q	.2	.4	.6	.8	1.0	1.2	1.4	1.6	1.8	2.0
.2	.1538	.1746	.1824	.1864	.1888	.1904	.1916	.1925	.1932	.1937
.4	.2439	.3025	.3285	.3428	.3517	.3578	.3623	.3656	.3682	.3703
.6	.3011	.3940	.4406	.4680	.4858	.4982	.5073	.5142	.5197	.5240
.8	.3389	.4585	.5234	.5637	.5906	.6098	.6241	.6351	.6439	.6509
1.0	.3637	.5022	.5811	.6323	.6673	.6928	.7119	.7268	.7388	.7485
1.2	.3787	.5295	.6184	.6770	.7180	.7483	.7713	.7894	.8040	.8160
1.4	.3864	.5436	.6378	.7007	.7453	.7785	.8039	.8240	.8403	.8537
1.6	.3882	.5470	.6425	.7065	.7520	.7859	.8120	.8327	.8494	.8632
1.8	.3854	.5417	.6350	.6972	.7411	.7737	.7986	.8182	.8340	.8470
2.0	.3790	.5296	.6179	.6756	.7156	.7448	.7667	.7838	.7974	.8084
2.2	.3699	.5122	.5931	.6444	.6784	.7026	.7199	.7330	.7430	.7509
2.4	.3588	.4911	.5629	.6060	.6327	.6502	.6617	.6695	.6748	.6786
2.6	.3465	.4675	.5290	.5628	.5811	.5908	.5956	.5972	.5968	.5955
2.8	.3336	.4428	.4933	.5172	.5266	.5276	.5247	.5195	.5130	.5060
3.0	.3207	.4179	.4573	.4710	.4710	.4632	.4525	.4402	.4270	.4139
3.2	.3083	.3938	.4224	.4260	.4168	.4004	.3818	.3622	.3423	.3231
3.4	.2967	.3714	.3898	.3839	.3662	.3433	.3151	.2885	.2621	.2370
3.6	.2863	.3512	.3605	.3459	.3203	.2878	.2547	.2216	.1892	.1585
3.8	.2774	.3339	.3353	.3132	.2805	.2416	.2025	.1635	.1258	.00011
4.0	.2701	.3198	.3146	.2865	.2480	.2036	.1595	.1157	.07352	.03369

P \ q	2.2	2.4	2.6	2.8	3.0	3.2	3.4	3.6	3.8	4.0
.2	.1942	.1946	.1949	.1951	.1952	.1956	.1958	.1959	.1961	.1962
.4	.3720	.3735	.3747	.3757	.3766	.3774	.3782	.3788	.3793	.3798
.6	.5277	.5307	.5333	.5355	.5374	.5392	.5406	.5419	.5431	.5442
.8	.6568	.6616	.6659	.6695	.6726	.6754	.6778	.6800	.6819	.6837
1.0	.7566	.7633	.7692	.7743	.7786	.7825	.7859	.7889	.7916	.7941
1.2	.8259	.8343	.8415	.8478	.8532	.8580	.8622	.8660	.8694	.8725
1.4	.8648	.8742	.8824	.8895	.8956	.9010	.9059	.9102	.9140	.9175
1.6	.8747	.8844	.8929	.9002	.9065	.9121	.9171	.9215	.9255	.9292
1.8	.8579	.8670	.8749	.8817	.8876	.8929	.8976	.9017	.9053	.9088
2.0	.8176	.8250	.8315	.8371	.8419	.8461	.8499	.8532	.8561	.8588
2.2	.7571	.7621	.7664	.7700	.7729	.7755	.7778	.7797	.7813	.7829
2.4	.6809	.6826	.6838	.6846	.6851	.6854	.6855	.6856	.6855	.6854
2.6	.5933	.5908	.5883	.5857	.5830	.5805	.5780	.5758	.5734	.5714
2.8	.4986	.4934	.4846	.4780	.4718	.4660	.4605	.4554	.4505	.4461
3.0	.4010	.3887	.3773	.3665	.3563	.3470	.3381	.3300	.3222	.3152
3.2	.3046	.2871	.2708	.2556	.2414	.2282	.2159	.2045	.1937	.1839
3.4	.2129	.1903	.1694	.1497	.1314	.1145	.09868	.08405	.07082	.05757
3.6	.1292	.1018	.07640	.05256	.03041	.00990	-.00929	-.02704	-.04319	-.05918
3.8	.05617	.02143	-.00499	-.03260	-.05826	-.08205	-.1043	-.1249	-.1437	-.1622
4.0	-.00416	-.03956	-.07240	-.1032	-.1319	-.1585	-.1833	-.2064	-.2276	-.2483

IMAGINARY PART

P \ q	.2	.4	.6	.8	1.0	1.2	1.4	1.6	1.8	2.0
.2	.01405	.01673	.01776	.01829	.01861	.01883	.01899	.01911	.01920	.01927
.4	.04120	.05566	.06246	.06627	.06868	.07033	.07153	.07245	.07315	.07372
.6	.07206	.1052	.1233	.1317	.1416	.1467	.1505	.1534	.1557	.1575
.8	.1037	.1591	.1927	.2119	.2296	.2405	.2486	.2550	.2601	.2642
1.0	.1346	.2139	.2654	.2981	.3259	.3447	.3590	.3703	.3795	.3870
1.2	.1641	.2672	.3377	.3854	.4251	.4534	.4754	.4929	.5073	.5192
1.4	.1911	.3175	.4071	.4702	.5228	.5616	.5922	.6170	.6375	.6545
1.6	.2163	.3638	.4715	.5499	.6154	.6650	.7048	.7375	.7646	.7873
1.8	.2382	.4050	.5294	.6223	.7002	.7605	.8095	.8500	.8839	.9126
2.0	.2571	.4406	.5800	.6858	.7752	.8453	.9030	.9510	.9916	1.0261
2.2	.2728	.4704	.6224	.7393	.8387	.9177	.9832	1.0381	1.0847	1.1246
2.4	.2852	.4941	.6561	.7821	.8901	.9764	1.0481	1.1092	1.1611	1.2057
2.6	.2944	.5117	.6817	.8147	.9287	1.0209	1.0980	1.1634	1.2195	1.2678
2.8	.3005	.5235	.6986	.8363	.9545	1.0508	1.1315	1.2001	1.2592	1.3102
3.0	.3037	.5296	.7075	.8478	.9683	1.0668	1.1494	1.2198	1.2805	1.3330
3.2	.3042	.5307	.7090	.8497	.9706	1.0694	1.1521	1.2231	1.2841	1.3368
3.4	.3024	.5271	.7038	.8430	.9625	1.0600	1.1418	1.2113	1.2713	1.3231
3.6	.2985	.5196	.6929	.8288	.9454	1.0401	1.1192	1.1863	1.2441	1.2938
3.8	.2930	.5088	.6772	.8084	.9206	1.0112	1.0867	1.1501	1.2045	1.2511
4.0	.2861	.4955	.6577	.7831	.8898	.9754	1.0460	1.1049	1.1551	1.1977

P \ q	2.2	2.4	2.6	2.8	3.0	3.2	3.4	3.6	3.8	4.0
.2	.01933	.01938	.01942	.01946	.01949	.01952	.01954	.01956	.01958	.01960
.4	.07419	.07458	.07491	.07520	.07545	.07567	.07586	.07602	.07618	.07632
.6	.1590	.1603	.1614	.1624	.1632	.1639	.1645	.1650	.1656	.1660
.8	.2676	.2704	.2730	.2751	.2769	.2786	.2800	.2812	.2824	.2834
1.0	.3932	.3984	.4030	.4069	.4103	.4133	.4160	.4183	.4204	.4224
1.2	.5291	.5375	.5448	.5511	.5566	.5611	.5658	.5697	.5730	.5763
1.4	.6689	.6810	.6917	.7010	.7091	.7162	.7227	.7284	.7334	.7382
1.6	.8067	.8230	.8375	.8501	.8612	.8710	.8799	.8877	.8947	.9012
1.8	.9372	.9581	.9766	.9928	1.0070	1.0197	1.0311	1.0413	1.0504	1.0589
2.0	1.0558	1.0813	1.1039	1.1237	1.1412	1.1568	1.1709	1.1835	1.1948	1.2053
2.2	1.1592	1.1890	1.2151	1.2386	1.2593	1.2777	1.2943	1.3092	1.3227	1.3352
2.4	1.2446	1.2781	1.3080	1.3343	1.3578	1.3787	1.3977	1.4147	1.4301	1.4441
2.6	1.3101	1.3468	1.3794	1.4082	1.4340	1.4571	1.4781	1.4968	1.5139	1.5297
2.8	1.3550	1.3939	1.4285	1.4592	1.4867	1.5113	1.5337	1.5538	1.5721	1.5890
3.0	1.3791	1.4192	1.4550	1.4868	1.5152	1.5408	1.5639	1.5848	1.6038	1.6213
3.2	1.3832	1.4235	1.4595	1.4914	1.5201	1.5458	1.5691	1.5900	1.6092	1.6268
3.4	1.3686	1.4081	1.4434	1.4746	1.5026	1.5276	1.5504	1.5708	1.5895	1.6067
3.6	1.3373	1.3750	1.4086	1.4383	1.4648	1.4885	1.5100	1.5293	1.5469	1.5630
3.8	1.2917	1.3268	1.3578	1.3851	1.4095	1.4311	1.4507	1.4682	1.4841	1.4987
4.0	1.2346	1.2662	1.2940	1.3183	1.3398	1.3588	1.3759	1.3911	1.4048	1.4173

$$\frac{4}{\pi} S^*(x, \beta) = G_0A_0 + \sum_{r=1}^{N-1} G_rA_r \tag{26}$$

where the G are defined as follows:

$$\left.\begin{aligned} G_0(\theta) &= \bar{F}_1(\theta) - \bar{F}_0(\theta) \\ G_r(\theta) &= \bar{F}_{r+1}(\theta) - \bar{F}_{r-1}(\theta) \end{aligned}\right\} \tag{27}$$

In the above-mentioned reference, the $\bar{F}$ are defined and a method for calculating them is also outlined.

After performing the integration indicated in Eq. (24), $R(x, \beta)$ becomes

$$R(x, \beta) = 4 + 2x - \sqrt{(x-1)^2 + \beta^2(x)} + \sqrt{(x+1)^2 + \beta^2(x)} + \beta \sinh^{-1}\left|\frac{\beta}{x-1}\right| - \beta \sinh^{-1}\left|\frac{\beta}{x+1}\right| \tag{28}$$

The function $R(x, \beta)$ has been evaluated for some special cases, and the results can be found in Table V.

The integral (25) is evaluated in Appendix (1); the result is

$$P(x, b, k) = be^{ik(1-x)}\left(N(b, k) - \frac{M(x, b, k)}{kb} + Ci[k(1-x)] + i\left\{\frac{\pi}{2} - Si[k(1-x)]\right\}\right) \tag{29}$$

where $M(x, b, k)$ and $N(b, k)$ are integrals defined in Appendix (1). $M(x, b, k)$ and the function $P(x, b, k)$ are tabulated in Tables VI and VII. For $\theta = 0$ ($x = 1$), Eq. (20) yields

$$g_s(x)|_{x=1} = \pi(A_0 + A_1) \tag{30}$$

Substituting Eqs. (26) and (30) into Eq. (22) for $x_n = \cos(n\pi/N)$, we have

$$\frac{4}{\pi} f(x_n) = G_{0n}A_0 + \sum_{r=1}^{N-1} G_{rn}A_r - \mu(k)(A_0 + A_1)[R(x_n, \beta_n) + P(x_n, b, k)] \tag{31}$$

This set of N simultaneous equations will give $A_0, A_1, \ldots A_{n-1}$. With these A_r, the series expansion (19) satisfies exactly the original integral equation at the N points x_n. The G_{rn} are evaluated by the method outlined in reference 9; $R(x, \beta)$ and $P(x, b, k)$ are evaluated by substituting in Eqs. (28) and (29).

For ($x = 1$) the functions $R(x, \beta)$ and $P(x, b, k)$ become infinite; however, their sum is finite, and an expression for this sum is calculated in Appendix (2).

Eq. (31) can be written as a matrix equation

$$F = (G + H)A = TA \tag{32}$$

where the matrices F, G, H, and A are defined as follows:

$$F = (4/\pi)\{f(x_0), f(x_1), f(x_2), f(x_3), f(x_4), f(x_5)\} \tag{32-1}$$

$$A = \{A_0, A_1, A_2, A_3, A_4, A_5\} \tag{32-2}$$

G and H are square matrices, with

$$\left.\begin{aligned} G_{0n} &= \bar{F}_1(\theta_n) - \bar{F}_0(\theta_n) \\ G_{rn} &= \bar{F}_{r+1}(\theta_n) - \bar{F}_{r-1}(\theta_n) \end{aligned}\right\} \tag{32-3}$$

$$\left.\begin{aligned} H_{0n} = H_{1n} &= -\mu(k)\{R[x_n, \beta(x_n)] + P(x_n, b, k)\} \\ H_{2n} = H_{3n} &= H_{4n} = H_{5n} = 0 \end{aligned}\right\} \tag{32-4}$$

where $x_n = \cos\theta_n$ and $\theta_n = n\pi/N$.

The braces $\{\ \}$ in F and A indicate column matrices.

(V) Solution of the Matrix Equation

For numerical calculations, a six-point collocation method was used, with the trailing edge as one of the collocation points. As will be seen in Section (X), the results obtained by this method for the case of infinite aspect ratio are satisfactory.

Premultiplying Eq. (32) by T^{-1}, we have

$$T^{-1}F = A \tag{33}$$

and defining new matrices Q and J

$$T^{-1} = (G + H)^{-1} = (I + G^{-1}H)^{-1}G^{-1} = (I + Q)^{-1}G^{-1} = J^{-1}G^{-1} \tag{34}$$

Direct inversion of T (a 6 by 6 matrix with complex elements) may be avoided by calculating the inverses of G and J. The elements of the matrix G are real, and J may be inverted by the following procedure.

The matrix $J = I + Q$ is of the form

$$J = \left[\begin{array}{cc:cccc} 1+Q_0 & Q_0 & 0 & 0 & 0 & 0 \\ Q_1 & 1+Q_1 & 0 & 0 & 0 & 0 \\ \hdashline Q_2 & Q_2 & 1 & 0 & 0 & 0 \\ Q_3 & Q_3 & 0 & 1 & 0 & 0 \\ Q_4 & Q_4 & 0 & 0 & 1 & 0 \\ Q_5 & Q_5 & 0 & 0 & 0 & 1 \end{array}\right]$$

J can be partitioned along the dotted lines into four submatrices

$$J = \begin{pmatrix} J_{11} & 0 \\ J_{21} & I \end{pmatrix}$$

The inverse of J is

$$J^{-1} = \begin{bmatrix} J_{11}^{-1} & 0 \\ -J_{21}J_{11}^{-1} & I \end{bmatrix} \tag{35}$$

where

TABLE VII

VALUES OF THE INTEGRAL $P(x,b,k)$

$$P(x,b,k) = \frac{e^{-ik(1-x)}}{k}\int_{k(1-x)}^{\infty} dt\, e^{-it}\left\{1 - \frac{\sqrt{t^2 + k^2b^2}}{t}\right\}$$

$$P(x,b,k) = P^*(p,q) = \frac{e^{ip}}{k}\int_0^{\infty} dt\, e^{-it}\left\{1 - \frac{\sqrt{t^2+q^2}}{t}\right\}$$

where $p = k(1-x)$ and $q = kb$. For convenience, the integral is tabulated as a function of the two variables p and q, rather than the three variables x, b and k

REAL PART

p \ q	.2	.4	.6	1	2	4
.2	-.3532	-.6030	-.7696	-.9698	-1.1684	-1.2593
.4	-.1513	-.2830	-.3859	-.5278	- .6893	- .7723
.6	-.08481	-.1645	-.2317	-.3339	- .4648	- .5400
.8	-.05396	-.1069	-.1531	-.2282	- .3344	- .4024
1.0	-.03701	-.07455	-.1078	-.1641	- .2506	- .3119
1.2	-.02674	-.05448	-.07926	-.1224	- .1933	- .2485
1.4	-.01986	-.04119	-.06038	-.09502	- .1524	- .2020
1.6	-.01570	-.03223	-.04713	-.07376	- .1223	- .1668
1.8	-.01229	-.02557	-.03750	-.05901	- .09966	- .1397
2.0	-.01013	-.02042	-.03045	-.04789	- .08218	- .1183
2.2	-.008534	-.01677	-.02506	-.03947	- .06855	- .1011

IMAGINARY PART

p \ q	.2	.4	.6	1	2	4
.2	.1258	.2380	.3325	.4807	.7048	.8958
.4	.07968	.1555	.2238	.3381	.5263	.6999
.6	.05708	.1124	.1640	.2542	.4132	.5710
.8	.04376	.08578	.1264	.1989	.3343	.4778
1.0	.03434	.06795	.1006	.1601	.2764	.4069
1.2	.02864	.05525	.08213	.1318	.2324	.3513
1.4	.02372	.04566	.06826	.1103	.1979	.3064
1.6	.02025	.03827	.05752	.09359	.1706	.2696
1.8	.01746	.03259	.04924	.08040	.1485	.2391
2.0	.01516	.02804	.04234	.06980	.1304	.2134
2.2	.01308	.02440	.03696	.06119	.1154	.1916

$$J_{11}^{-1} = \begin{bmatrix} 1+Q_1 & -Q_0 \\ -Q_1 & 1+Q_0 \end{bmatrix} \frac{1}{1+Q_0+Q_1} \tag{36}$$

The inversion of J has been reduced to a substitution into Eq. (36) and to the multiplication of J_{21} by J_{11}^{-1}, or that of a 4 by 2 matrix by a 2 by 2 matrix. The inversion of G is equivalent to solving the steady-state problem. In most cases, this problem will have been solved prior to the consideration of the nonsteady case. Its availability will reduce considerably the amount of work required to compute the inverse of T.

It will be observed that the matrix G depends only on the plan form, while the matrix J depends both on the plan form and on the frequency of oscillations. Hence, for a given wing, it will be necessary to calculate G^{-1} only once, while J^{-1} will have to be calculated for each frequency. For different camber surfaces G^{-1} and J^{-1} do not change; hence, the solutions require only the multiplication of T^{-1} by a new F matrix.

(VI) Calculation of Air Forces

The superscript T refers to translatory oscillations; R, to rotational oscillations; and F, to wings with flaps.

For translatory oscillations of the wing, F^T may be taken as $F_n^T = \beta^2(x_n)/b^2$, and if the A satisfy Eq. (33), the lift and moment coefficients L_h and M_h are

$$L_h = -(2i\text{A.R.}/k)[(A_0^T + A_1^T)(1 + ik)(1 - 2\mu) + (ik/2)(A_0^T - A_2^T)] \tag{37}$$

$$M_h = -\frac{i\text{A.R.}}{k}\left\{(A_0^T + A_1^T)[(1-2\mu)(1+ik) + 2ik\left(\frac{1}{4} - \frac{2}{3}\mu\right)\right] + \frac{1}{2}(A_0^T - A_2^T)(ik - 2) + \frac{ik}{4}(A_1^T - A_3^T)\Big\} \tag{38}$$

For rotational oscillations about the wing quarter chord, $F_n^R = [\beta^2(x_n)/b^2]x_n$. The lift and moment coefficients L_α and M_α are

$$L_\alpha = \left(\frac{1}{2} - \frac{i}{k}\right) L_h - \frac{2i}{k}\,\text{A.R.}\left[(A_0^R + A_1^R)(1 + ik)(1 - 2\mu) + \frac{ik}{2}(A_0^R - A_2^R)\right] \tag{39}$$

$$M_\alpha = \left(\frac{1}{2} - \frac{i}{k}\right) M_h - \frac{i}{k}\,\text{A.R.}\left\{(A_0^R + A_1^R)\left[(1 + ik)(1 - 2\mu) + 2ik\left(\frac{1}{4} - \frac{2}{3}\mu\right)\right] + \frac{1}{2}(A_0^R - A_2^R)(ik - 2) + \frac{ik}{4}(A_1^R - A_3^R)\right. \tag{40}$$

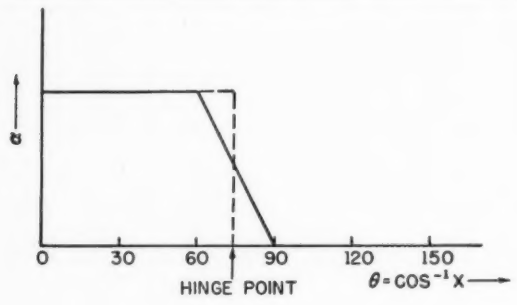

DIAGRAM 1.

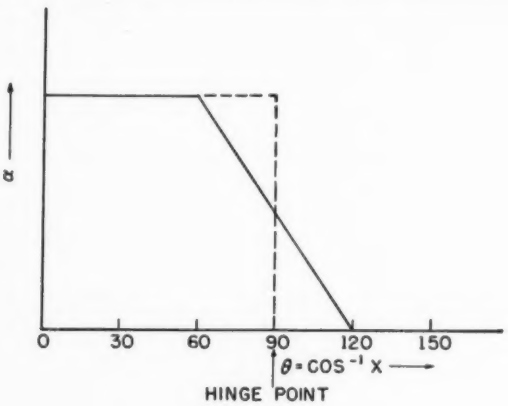

DIAGRAM 2.

For the case of wings with flaps, an approximate procedure will be employed. A clue to this procedure may be obtained by consideration of the Prandtl lifting-line equation. This equation has been solved approximately for cases where the angle of attack distribution is discontinuous by choosing the hinge point either at a collocation point or midway between two collocation points.[12] The results of such approximate calculations are found to be sufficiently accurate for most engineering calculations. A similar procedure will be employed herein.

Let a denote the position of the hinge point with respect to the mid-chord point. a must either be given by $a = \cos(n\pi/N)$ or $a = \cos[(2n + 1)/2N]\pi$. For other values of a, the lift and moment coefficients may be obtained from the ones corresponding to the above a by interpolation.

Case (I)

The hinge point is midway between two collocation points. F_n^{TF} will then have the following values:

$$F_n^{TF} = \beta^2(x_n)/b^2 \quad (x_n > a)$$
$$F_n^{TF} = 0 \quad (x_n < a)$$

In Diagram 1, the hinge point is located at $\theta = 75°$ (this corresponds to a 37 per cent flap). The solid line indicates the approximate value of the angle of attack, while the dotted line indicates the correct value.

Case (II)

The hinge point is located at one of the collocation points. F_n^{TF} will then be

$$F_n^{TF} = \beta^2(x_n/b^2) \quad (x_n > a)$$
$$F_n^{TF} = \frac{1}{2}\frac{\beta^2(x_n)}{b_2} \quad (x_n = a)$$
$$F_n^{TF} = 0 \quad (x_n < a)$$

In Diagram 2, the hinge point is located at $\theta = 90°$. This corresponds to a 50 per cent flap.

The lift and moment coefficients L_z and M_z can be obtained by substituting A^{TF} for A^T in Eqs. (37) and (38).

For rotational oscillations about the hinge point, Case (I)

$$F_n^{RF} = [\beta^2(x_n)/b^2]x_n \quad (x_n > a)$$
$$F_n^{RF} = 0 \quad (x_n < a)$$

Case (II), $F_n^{RF} = [\beta^2(x_n)/b^2]x_n \quad (x_n > a)$

$$F_n^{RF} = \frac{1}{2}\frac{\beta^2(x_n)}{b^2} \quad (x_n = a)$$
$$F_n^{RF} = 0 \quad (x_n < a)$$

The coefficients L_β and M_β can be calculated by substituting in

$$L_\beta = -\left(a + \frac{i}{k}\right) L_z - \frac{2i}{k}\,\text{A.R.}\left[(A_0^{TR} + A_1^{TR})(1 + ik)(1 - 2\mu) + \frac{ik}{2}(A_0^{TR} - A_2^{TR})\right] \tag{41}$$

$$M_\beta = -\left(a + \frac{i}{k}\right)M_z - \frac{i}{k}\,\text{A.R.}\left\{(A_0^{TR} + A_1^{TR})\left[(1-2\mu)(1+ik) + 2ik\left(\frac{1}{4} - \frac{2}{3}\mu\right)\right] + \frac{1}{2}(A_0^{TR} - A_2^{TR})(ik-2) + \frac{ik}{4}(A_1^{TR} - A_3^{TR})\right\} \quad (42)$$

(VII) Comparison of Results with Limiting Cases

It can be shown (for method, see reference 9) that the integral equation approaches a correct limiting form in the following cases: (1) as k approaches 0, or steady-state case;[9] (2) as the aspect ratio approaches 0, the limit being the extended Jones theory;[7] and (3) as the aspect ratio approaches ∞, the two-dimensional result[11] is reproduced for rectangular wings.

The results, obtained by solving the integral equation by the method presented in the preceding sections, agree with the limiting cases, as shown below. This indicates that the proposed method of solution of the integral equation is a satisfactory approximation.

(VIII) Results for Very Low Aspect Ratio Wings

The Jones theory, extended to nonsteady forces, yields for the lift and moment coefficients:

(1) Of rectangular wings:

$$L_h = \text{A.R.}[1 - (i/2k)], \qquad M_h = (\text{A.R.}/2)[1 + (i/2k)]$$

$$L_\alpha = \frac{\text{A.R.}}{2}\left(1 - \frac{1}{k^2} - \frac{7i}{2k}\right), \qquad M_\alpha = \frac{\text{A.R.}}{2}\left(\frac{7}{6} + \frac{1}{2k^2} - \frac{9i}{4k}\right)$$

(2) Of triangular wings:

$$L_h = \text{A.R.}[(1/3) - (i/2k)], \qquad M_h = \text{A.R.}[(1/3) - (5i/12k)]$$

$$L_\alpha = \frac{\text{A.R.}}{2}\left[\frac{13}{6} - i\left(\frac{1}{k} - \frac{2k}{3}\right)\right], \qquad M_\alpha = \frac{\text{A.R.}}{8}\left(-\frac{46}{15} + \frac{10}{3k^2} + \frac{9i}{k}\right)$$

These results would be represented on the plots of L and M by straight lines, tangent at the origin to the results of the present theory.

(IX) Results for Infinite Aspect Ratio

In Appendix (3) it is shown that the limit of Eq. (31) when b becomes infinite is

$$\lim_{b\to\infty}\frac{4}{\pi}f(x) = A_0 + 2\sum_{r=1}^{N-1} A_r x_r - \mu(k)(A_0 + A_1)B_r(x_r k) \quad (43)$$

The function B is defined in Appendix (3). The matrix G^{-1} for infinite aspect ratio can be obtained analytically from the orthogonal properties of finite trigonometric series and

$$G^{-1} = \frac{1}{12}\begin{bmatrix} 0 & 4 & 0 & 4 & 0 & 4 \\ 2 & (\sqrt{3}-2) & 3 & -2 & 1 & (-2-\sqrt{3}) \\ 0 & 3 & -3 & 0 & -3 & 3 \\ 2 & -2 & 0 & -2 & 4 & -2 \\ 0 & 1 & -3 & 4 & -3 & 1 \\ 2 & (-\sqrt{3}-2) & 3 & -2 & 1 & \sqrt{3}-2 \end{bmatrix}$$

The results for $k = 2$ are given in the Table (A) for two-dimensional profiles with 50 per cent chord flap.

Table (A)

	Real Part		Imaginary Part	
	Two-dimensional theory[11]	Present theory	Two-dimensional theory[11]	Present theory
L_h	0.9423	0.946	−0.5129	−0.510
M_h	0.5000	0.500	0	0.002
L_α	0.1858	0.191	−0.98405	−0.983
M_α	0.3750	0.376	−0.5000	−0.498
L_z	0.45278	0.456	−0.41971	−0.414
M_z	0.35610	0.349	−0.15916	−0.154
L_β	−0.03048	−0.040	−0.51788	−0.514
M_β	0.08903	0.084	−0.35610	−0.355

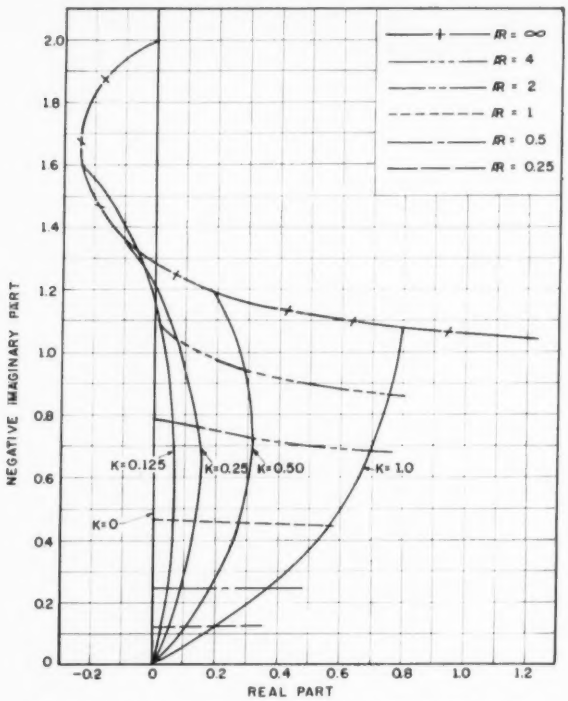

FIG. 2. Vector representation of kL_h for rectangular wings.

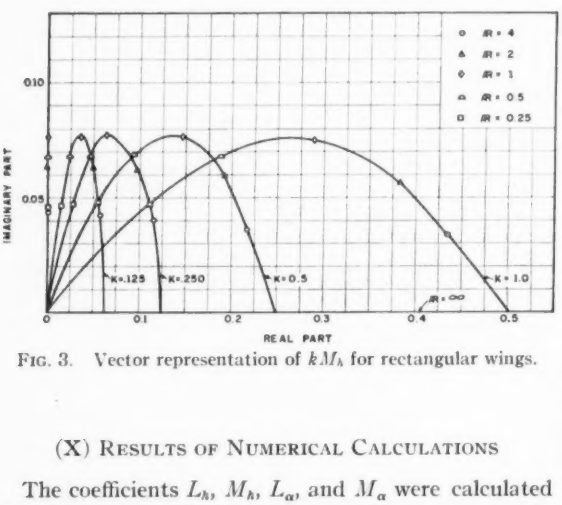

FIG. 3. Vector representation of kM_h for rectangular wings.

(X) Results of Numerical Calculations

The coefficients L_h, M_h, L_α, and M_α were calculated for rectangular and triangular wings for an aspect ratio ranging from 0 to 4 and for reduced frequencies from zero to unity. The results are tabulated in Tables I and II, and they are plotted on Figs. 2, 3, 4, and 5.

Lines joining points with the same aspect ratio or with the same frequency of oscillation were drawn.

The results of the steady-state theory of reference 9 (limit of the present theory) were included, and it is seen that the aspect ratio lines terminate smoothly at the correct values.

For the infinite aspect ratio case, the coefficients L and M were calculated for several frequencies of oscillation. As seen from Table (A), the agreement with the corresponding values of reference 11 is satisfactory. Hence, the results of reference 11 were used in plotting the graphs. The constant frequency lines terminate at the expected points on the infinite aspect ratio lines.

In these graphs, the Garrick[7] theory gives straight lines through the origin. In all cases considered, they are tangent at the origin to the curves representing the present results.

The coefficients L_z, M_z, L_β, and M_β were calculated for rectangular wings of aspect ratio 1 and 2, with 25, 37, and 50 per cent chord flaps. The results can be found in Tables III and IV.

(XI) Comparison with High Aspect Ratio Theories

The present theory will be compared with Reissner's theory,[13] since the latter is probably the most accurate of the high aspect ratio theories. For simplicity, only total lift coefficients will be considered.

In Fig. 6, the values of kL_h predicted by both theories for rectangular wings of aspect ratio 3 were plotted. It will be observed that whereas the real parts agree, the imaginary parts differ by about 15 per cent. In Fig. 7, the values of k^2L_α for the same configuration were plotted; in this case the imaginary parts agree, while the real parts differ by 15 per cent. Since the Reissner theory is an extension of the Prandtl theory

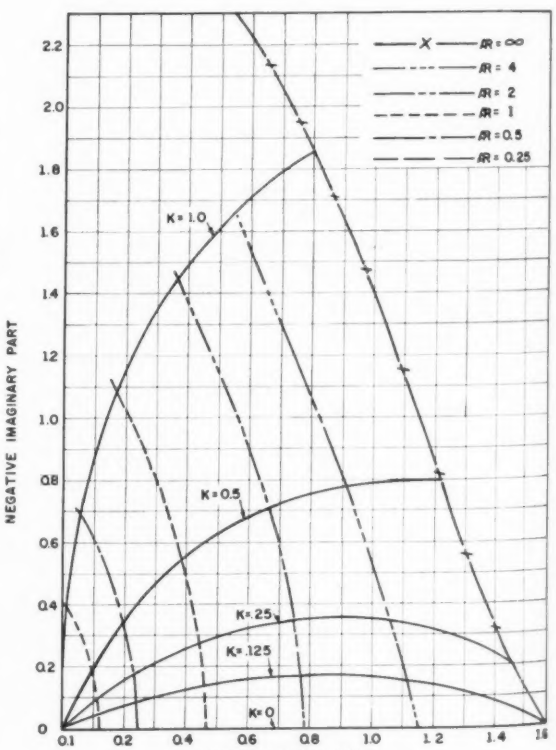

FIG. 4. Vector representation of k^2L_α for rectangular wings.

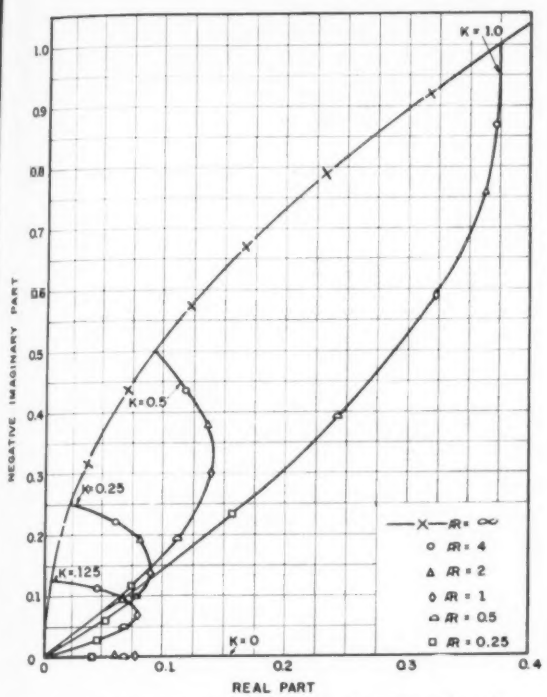

FIG. 5. Vector representation of k^2M_α for rectangular wings.

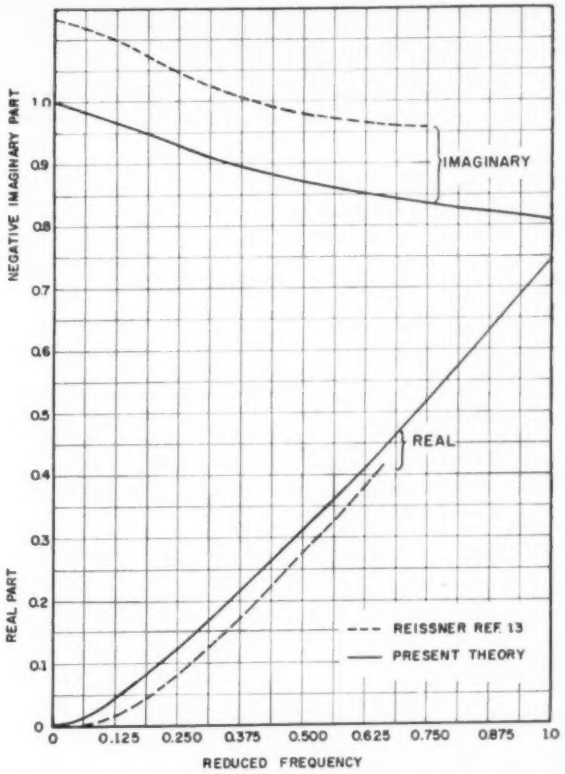

FIG. 6. Theoretical predictions of kL_h for a rectangular wing of aspect ratio 3.

whereas the present theory is an extension of reference 9 and since these steady-state solutions differ by 15 per cent, the disagreement noted above is not surprising.

(XII) LIMITS OF VALIDITY

The present theory is applicable to swept wings for all useful frequencies of oscillation, but it is restricted to straight trailing edges and to aspect ratios less than 4.

Since the present theory agrees with the theory of reference 9 for low k, with the Garrick results for low aspect ratio and with the two-dimensional results for A.R. $= \infty$ and for $k < 2.5$, there is good reason to believe that satisfactory values are predicted by it for (1) the wing lift and moment coefficients and (2) the chordwise lift distribution.

REFERENCES

[1] Cicala, P., *Sul moto non stazionario di un' ala di allungamento finito*, Rendiconti R. Accad. Naz. Lincei, Vol. 25, Ser. 6a, No. 3-4, pp. 97–102, August, 1937.

[2] Borbely, V., *Über einen Grenzfall der instationären räumlichen Tragflügelströmung*. Z.F.A.M.M., Bd. 18, Heft 6, pp. 319–342, December, 1938.

[3] Küssner, H. G., *General Airfoil Theory*, N.A.C.A. T.M. No. 979, 1941.

[4] Jones, R. T., *The Unsteady Lift of a Wing of Finite Aspect Ratio*, N.A.C.A. T.R. No. 681, 1940.

[5] Reissner, Eric, *On the General Theory of Thin Airfoils for Non-Uniform Motion*, N.A.C.A. T.N. No. 946, 1944.

(*Continued on following page*)

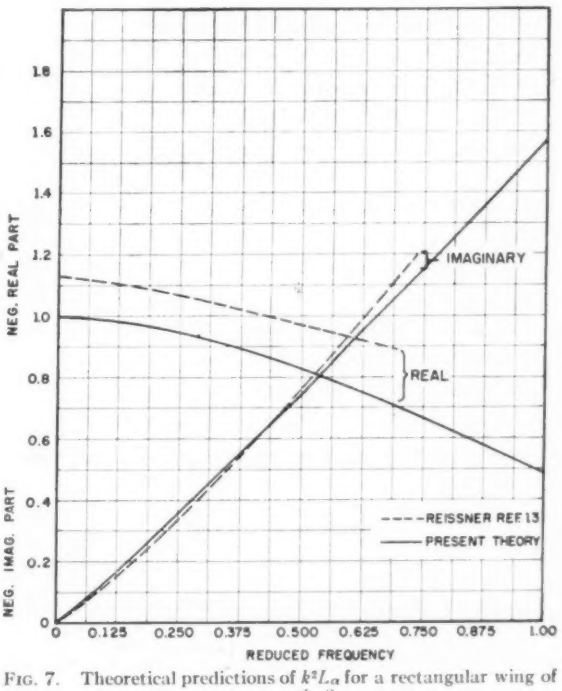

FIG. 7. Theoretical predictions of k^2L_α for a rectangular wing of aspect ratio 3.

[6] Jones, R. T., *Properties of Low-Aspect-Ratio Pointed Wings at Speeds Below and Above the Speed of Sound*, N.A.C.A. T.N. No. 1032, 1946.

[7] Garrick, I. E., *Some Research on High Speed Flutter*, Proceedings of the Third Anglo-American Aeronautical Conference, Appendix B; R.Ae.S.-I.A.S. 1951.

[8] Schade, Th., and Krienes, K., *The Oscillating Circular Airfoil on the Basis of Potential Theory*, N.A.C.A. T.M. No. 1098, February, 1947.

[9] Lawrence, H. R., *The Lift Distribution of Low-Aspect-Ratio Wings at Subsonic Speeds*, Journal of the Aeronautical Sciences, Vol. 18, No. 10, pp. 683–695, October, 1951.

[10] Flax, A. H., and Lawrence, H. R., *The Aerodynamics of Low-Aspect-Ratio Wings and Wing-Body Combinations*, Proceedings of the Third Anglo-American Aeronautical Conference; R.Ae.S.-I.A.S., 1951.

[11] Smilg, B., and Wasserman, L., *Application of Three-Dimensional Flutter Theory to Aircraft Structures*, A.A.F. T.R. 4798, July, 1942.

[12] Pearson, H. A., *Span Load Distribution for Tapered Wings with Partial-Span Flaps*, N.A.C.A. T.R. No. 585, 1937.

[13] Reissner, Eric, *The Effect of Finite Span on the Airload Distributions for Oscillating Wings; I—Aerodynamic Theory of the Oscillating Wing of Finite Span*, N.A.C.A. T.N. No. 1194, March, 1947. Reissner, Eric, and Stevens, John E., *II—Methods of Calculation and Examples of Applications*, N.A.C.A. T.N. No. 1195, October, 1947.

[14] Jahnke, E., and Emde, F., *Tables of Functions with Formulae and Curves*, Dover Publications, 1943.

[15] Biot, M. A., and Boehnlein, C. T., *Aerodynamic Theory of the Oscillating Wing of Finite Span*, GALCIT Report 5 to U.S.A.-A.F., 1942.

[16] Chiarulli, P., *Oscillating Wings of Finite Aspect Ratio*, TR-102, AC 49/9-100, A.M.C., U.S.A.F., 1949.

[17] Prandtl, L., *Recent Work on Airfoil Theory*, N.A.C.A. T.M. No. 962, 1940.

[18] Cicala, P., *Present State of Development in Non-Steady Motion of a Lifting Surface*, N.A.C.A. T.M. No. 1277, October, 1951. (Translated from *Lo Stato Attule delle Ricerche sul Moto Instazionzrio di Una Superficie Portanle*, Estralto da L'Aeroticnica, Vol. XXI-N.9-10, September-October, 1941.

[19] Sears, William R., *A Contribution to the Airfoil Theory for Non-Uniform Motion*, Proceedings of Fifth International Congress of Applied Mechanics, pp. 483–487, 1938.

[20] Flax, A. H., *General Reverse Flow and Variational Theorems in Lifting-Surface Theory*, Cornell Aeronautical Laboratory Report 34, May, 1951.

[21] Lomax, Harvard, and Heaslet, Max, *Linearized Lifting-Surface Theory for Swept-Back Wings with Slender Planforms*, N.A.C.A. T.N. No. 1992, December, 1949.

Appendix (1)

Evaluation of the Integral (25)

$$P(x, k, b) = \int_1^\infty d\xi e^{-ik(\xi - 1)} \left[1 + \frac{\sqrt{(x - \xi)^2 + b^2}}{(x - \xi)}\right] \tag{25}$$

After making the following change in variable, $\xi = x + (t/k)$, P can be written as

$$P(x, k, b) = \frac{e^{ik(1 - x)}}{k} \int_{k(1 - x)}^\infty dt e^{-it} \left(1 - \frac{\sqrt{t^2 + k^2b^2}}{t}\right)$$

Adding and subtracting kb/t,

$$P(x, k, b) = \frac{e^{ik(1 - x)}}{k} \int_{k(1 - x)}^\infty dt e^{-it} \left(1 + \frac{kb - \sqrt{t^2 + k^2b^2}}{t} - \frac{kb}{t}\right) =$$

$$be^{ik(1 - x)} \left(N, (b, k) - \frac{M}{kb}(x, b, k) + Ci\,[k(1 - x)] + i\left\{\frac{\pi}{2} - Si\,[k(1 - x)]\right\}\right)$$

where $N(k, b)$ is defined in reference 13 as the integral

$$N(k, b) = \int_0^\infty dt e^{-it} \left(\frac{1}{kb} + \frac{1}{t} - \frac{\sqrt{t^2 + k^2b^2}}{kbt}\right) \tag{44}$$

and $M(x, k, b)$ will be defined as

$$M(x, b, k) = \int_0^{k(1 - x)} dt e^{-it} \left(1 + \frac{kb}{t} - \frac{\sqrt{t^2 + k^2b^2}}{t}\right) \tag{45}$$

Ci and Si are the sine and cosine integrals of reference (14).

Appendix (2)

Evaluation of $R(1, \beta) + P(1, k, b)$

As x approaches 1, $R(x, \beta)$ approaches the following limit:

$$\lim_{x \to 1} R(x, \beta) = 6 - b + \sqrt{4 + b^2} + b \log \left|\frac{b + \sqrt{(x - 1)^2 + b^2}}{x - 1}\right| - b \sinh^{-1} \left|\frac{b}{2}\right|$$

while $P(x, k, b)$ approaches

$$\lim_{x \to 1} P(x, k, b) = b\left[N(k, b) - \log \frac{1}{\gamma(1 - x)k} + \frac{i\pi}{2} \right]$$

since $Ci\ x \underset{x \to 0}{\longrightarrow} - \log \frac{1}{\gamma x}$ with $\gamma = 1.78107$ (see Reference 14),

$$\lim_{x \to 1} \left[R(1, \beta) + P(1, k, b) \right] = \left[6 - b + \sqrt{4 + b^2} - b \sinh^{-1} \left| \frac{b}{2} \right| + bN(kb) + b \log 2\gamma bk + i \frac{\pi}{2} b \right]$$

Appendix (3)

Limit of Eq. (31) When the Aspect Ratio Becomes Infinite

We have

$$\lim_{\beta \to \infty} \frac{4}{\pi} S_n^*(x, \beta) = \beta A_0 + 2 \sum_{r=1}^{N-1} \cos\left(\frac{rn\pi}{N}\right) \beta A_r$$

$$\lim_{\beta \to \infty} R(x_n, \beta) = \beta \log \left[(x_n + 1)/(x_n - 1) \right]$$

$$\lim_{b \to \infty} P(x_n, k, b) = be^{ik(1-x)} \left\{ Ci\ k(1 - x) + i \left[\frac{\pi}{2} - \mathrm{Si}\ k(1 - x) \right] \right\}$$

Combining these expressions ($\beta \to b$),

$$\lim_{b \to \infty} \frac{4}{\pi} f_n(x, b) = b\left[A_0 + 2 \sum_{r=1}^{N-1} A_r \cos r\theta - \mu(k)(A_0 + A_1) B_n(x_n k) \right] \tag{46}$$

where $B(x, k)$ is defined as

$$B(x, k) = \log \left| \frac{x + 1}{x - 1} \right| + e^{ik(1-x)} \left\{ Ci\ k(1 - x) + i \left[\frac{\pi}{2} - Si\ k(1 - x) \right] \right\} \tag{47}$$

For $x = 1$,

$$\lim_{b \to \infty} \frac{4}{\pi} f(1, b) = b\left[A_0 + 2 \sum_{r=1}^{N-1} A_r - \mu(k)(A_0 + A_1) \left(\log 2\gamma k + i \frac{\pi}{4} \right) \right] \tag{48}$$

In Eqs. (46) and (48), let bA_n be replaced by A_n'. In the expressions for the L and M coefficients, we must now substitute A_n'/b; however, for a rectangular wing A.R. $= b$, and b cancels out.

For a rectangular wing of infinite aspect ratio, it is only necessary to calculate the A' and substitute them for the A in the expressions for L and M, taking the aspect ratio as 1.

Readers' Forum

BRIEF REPORTS of investigations in the aeronautical sciences and discussions of papers published in the JOURNAL are presented in this special department. Publication will be completed as soon as possible after receipt of the material. The Editorial Committee does not hold itself responsible for the opinions expressed by the correspondents. Contributions should not exceed 800 words in length.

The Study of Compressible Flow Through Cascades Using a Linear Pressure-Volume Relationship

David C. Prince, Jr.
General Electric Company, West Lynn, Mass.
July 14, 1952

A CONSIDERABLE AMOUNT OF EFFORT has been put into the study of compressible flows through cascades by approximating the relationship between pressure and specific volume by a straight line. In particular, the work of Lin[1] and of Costello[2,3] may be mentioned. The relations established by Costello appear to allow a relatively simple physical interpretation if a slight revision in form is made.

It is convenient to make use of a hodograph velocity parameter ω, such that

$$\omega = \ln \frac{q/(a_1\sqrt{1 - M_1^2})}{1 + \sqrt{1 + q^2/[a_1^2(1 - M_1^2)]}} \tag{1}$$

where q is the local velocity and a_1 and M_1 are the sound velocity and Mach number at a reference point in the flow, where the straight-line pressure-volume relation is taken tangent to the true isentrope. For decelerating cascades, the reference point is frequently the undisturbed condition upstream from the cascade.

Using this definition, a suitably defined velocity potential, such that

$$q/(a_1\sqrt{1 - M_1^2}) = |\nabla\phi| \tag{2}$$

and a stream function,

$$q/(a_1\sqrt{1 - M_1^2}) = (1/\sqrt{1 - M^2})\,|\nabla\psi| \tag{3}$$

satisfy Cauchy-Riemann equations in the hodograph parameters ω and $(-\lambda)$, where λ is the angle made by the flow with a reference direction such as the normal to the cascade axis. It follows, of course, that $(\phi + i\psi)$ is an analytic function of $(\omega - i\lambda)$. $(\phi + i\psi)$ and $(\omega - i\lambda)$ can also be expressed, if desired, as analytic functions of some other parameter $\xi + i\eta$, such as position in the picture plane used by Weinig[4] and others.

The position variable in the physical plane $(x + iy)$ may be obtained from ϕ, ψ, ω, and λ by the transformation

$$dx + idy = \frac{1}{2}\left[\frac{d\phi + id\psi}{e^{\omega - i\lambda}} - e^{\omega + i\lambda}\,(d\phi - id\psi)\right] \tag{4}$$

which is analogous to Eq. (11.51) of reference 5.

The flow through a cascade must satisfy continuity and lead to closed airfoils. The continuity condition,

$$\rho_1 q_1 \cos\lambda_1 = \rho_2 q_2 \cos\lambda_2 \tag{5}$$

(where the subscript 1 refers to upstream conditions, subscript 2 refers to downstream conditions, and ρ is the density) leads to

VARIATION OF HODOGRAPH WITH MACH NUMBER
APPLICATION OF KARMAN-TSIEN METHOD TO CASCADES

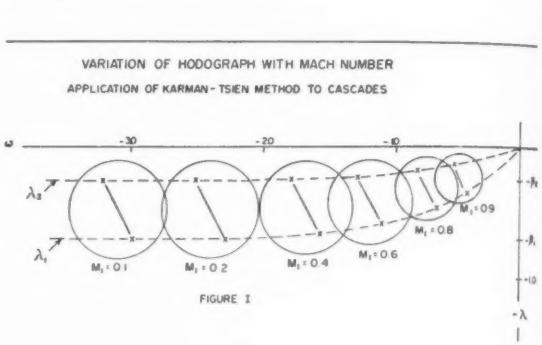

FIGURE I

$$\cos\lambda_1/\cosh\omega_1 = \cos\lambda_2/\cosh\omega_2 \tag{6}$$

which means that the downstream velocity vector cannot be chosen independently of the upstream vector. The closure condition is to be satisfied by integrating Eq. (4) across the flow between a pair of adjacent airfoils along paths upstream and downstream from the cascade. The result of such integrations will be paths parallel to the cascade axis if the complex velocity potential $(\phi + i\psi)$ as a function of the complex hodograph variable $(\omega - i\lambda)$ has a logarithmic singularity at the upstream condition with an angle β_1 representing the ratio of vortex strength to source strength, such that

$$\tan\beta_1 = -\tan\lambda_1/\tanh\omega_1 \tag{7}$$

and a corresponding downstream condition with

$$\tan\beta_2 = -\tan\lambda_2/\tanh\omega_2 \tag{8}$$

These paths of integration upstream and downstream from the cascade will be the same length if the source and sink strengths of the logarithmic singularities are adjusted so that

$$\cos\beta_1/\sinh\omega_1 = \cos\beta_2/\sinh\omega_2 \tag{9}$$

Eqs. (6), (7), (8), and (9) provide the basis for comparing cascade performance at different Mach Numbers. For extremely low Mach Numbers, $\tanh\omega$ approaches -1, so that λ_1 approaches β_1 and λ_2 approaches β_2. In other words, β_1 and β_2 are the upstream and downstream flow angles for an incompressible cascade with which the compressible cascade may be compared. This suggests that the proper basis for comparison between cascades is the possession of identical, or at least geometrically similar, hodographs. Actually, geometric similarity is as much as can be specified. Fig. I shows the manner in which geometrically similar hodographs vary as the reference Mach Number is varied. The functional relationship between complex velocity potential and complex hodograph parameter is varied only by translation and scale and by a slight rotation (0.3° from $M_1 = 0$ to $M_1 = 1.0$). Eqs. (6), (7), (8), and (9) are satisfied for all conditions, with β_1 and β_2 held fixed. These particular hodographs are circles with diameter one and one-half times the hodograph distance

between upstream and downstream conditions and are symmetrically placed.

The nature of the relationship between complex hodograph parameter and complex velocity potential shows that similar velocity variations will occur at similar points in the complex velocity potential field when the latter has been determined in the physical plane. As the Mach Number is increased, the upstream and downstream flow angles, the stagger, and the stream deflection all decrease. The camber angle of the airfoils, given by the diameter of the hodograph circle, also decreases. The cascade solidity will decrease at the same time, since the potential gradient at any point in the physical plane is greater than the stream-function gradient and since the ratio between the two increases with increasing Mach Number.

The comparison between cascades at different Mach Numbers described here is for airfoils with cusp ends. Comparison for airfoils with rounded leading edges is possible only if the edge effect is neglected, since the relationships among angles really imply that the included angle of the leading edge will decrease along with the other flow angles in the field.

The relations obtained here appear to imply those obtained by Woolard[6] using the Prandtl-Glauert approach when the limiting case of small stream deflections is considered.

References

[1] Lin, C. C., *On the Subsonic Flow Through Circular and Straight Lattices of Airfoils*, Journal of Mathematics and Physics, July, 1949.

[2] Costello, G. R., *Methods of Designing Cascade Blades with Prescribed Velocity Distributions in Compressible Potential Flows*, N.A.C.A. Report No. 978, 1950.

[3] Costello, G. R., Cummings, R. L., and Sinnette, J. T., Jr., *Detailed Computational Procedure for Design of Cascade Blades with Prescribed Velocity Distributions in Compressible Potential Flows*, N.A.C.A. T.N. No. 2281, February, 1951.

[4] Weinig, F., *Die Stromung um die Schaufeln von Turbomaschinen;* J. A. Barth, Leipzig, 1935.

[5] Liepmann, H. W., and Puckett, A. E., *Introduction to Aerodynamics of a Compressible Fluid;* John Wiley & Sons, Inc., New York, 1947.

[6] Woolard, H. W., *A Note on the Subsonic Compressible Flow About Airfoils in a Cascade*, Journal of the Aeronautical Sciences, Vol. 17, No. 6, pp. 379–381, June, 1950.

A New Mechanical Analogy for the Flow of Compressible Fluid

Nobuo Inoue

Faculty of Engineering, Doshisha University, Kyoto, Japan

July 25, 1952

CONSIDER A STATICALLY DETERMINATE STATE OF STRESS in a perfectly plastic material. For plane plastic flow parallel to the x, y plane, the state of stress at a point is completely defined when the normal and shearing stresses σ_x, σ_y, and τ_{xy} are known. For the determination of these three functions of x and y, we have the equations of equilibrium

$$\frac{\partial \sigma_x}{\partial x} + \frac{\partial \tau_{xy}}{\partial y} = 0, \quad \frac{\partial \tau_{xy}}{\partial x} + \frac{\partial \sigma_y}{\partial y} = 0 \tag{1}$$

and the yield condition

$$\tau = \tau(\sigma) \tag{2}$$

where $\sigma = (\sigma_1 + \sigma_2)/2$, $\tau = (\sigma_1 - \sigma_2)/2$, with the algebraically greater and smaller principal stresses σ_1 and σ_2. In addition, the three components of stress can be expressed, with the mean principal stress σ and the angle α_1 which the first principal direction makes with the x-axis, as follows:

$$\left.\begin{aligned} \sigma_x &= \sigma + \tau(\sigma)\cos 2\alpha_1 \\ \sigma_y &= \sigma - \tau(\sigma)\cos 2\alpha_1 \\ \tau_{xy} &= \tau(\sigma)\sin 2\alpha_1 \end{aligned}\right\} \tag{3}$$

Now we make the state of stress correspond to the flow of nonviscous compressible fluid by the following relations:

$$\frac{dq}{q} = -\frac{1-\tau'}{2\tau}\,d\tau, \quad \frac{d\rho}{\rho} = \frac{d\sigma}{\tau}, \quad \theta = \alpha_2 \tag{4}$$

(when $\tau' < 1$), or

$$\frac{dq}{q} = \frac{1+\tau'}{2\tau}\,d\tau, \quad \frac{d\rho}{\rho} = -\frac{d\sigma}{\tau}, \quad \theta = \alpha_2 \tag{4'}$$

(when $\tau' > -1$), where q, θ are the polar coordinates of the fluid-velocity vector in the hodograph plane, α_2 is the angle that the second principal direction makes with the x-axis, and $\tau' = d\tau/d\sigma$. Then it will be seen, after some calculations, that the equations of equilibrium [Eq. (1)] become the equations of continuity and irrotationality

$$\left.\begin{aligned} \frac{\partial}{\partial x}(\rho u) + \frac{\partial}{\partial y}(\rho v) &= 0 \\ \partial v/\partial x &= \partial u/\partial y \end{aligned}\right\} \tag{5}$$

if the yield condition [Eq. (2)] satisfies the differential equation

$$\tau\frac{d^2\tau}{d\sigma^2} + \left(\frac{d\tau}{d\sigma}\right)^2 - (\gamma+1)\frac{d\tau}{d\sigma} + \gamma = 0 \tag{6}$$

when the equation of velocity-stress correspondence, Eq. (4), is used, or

$$\tau\frac{d^2\tau}{d\sigma^2} + \left(\frac{d\tau}{d\sigma}\right)^2 + (\gamma+1)\frac{d\tau}{d\sigma} + \gamma = 0 \tag{6'}$$

when the equation of velocity-stress correspondence, Eq. (4'), is used, γ being the adiabatic exponent of the fluid.

Therefore, the two-dimensional steady irrotational flow of the fluid can be wholly replaced by the statically determinate two-dimensional state of stress in the perfectly plastic material, stream lines and equipotential lines of the former corresponding to isostatics of the latter and Mach lines to slip lines when the fluid flow is supersonic. The shock front in supersonic flow of the fluid becomes equivalent to the stress-discontinuity surface in the perfectly plastic material, and the jump conditions at the shock front (which have been obtained by the conservation of mass, momentum, and energy in passing through it) yield the continuity of the normal and shearing stresses acting in the stress-discontinuity surface when translated into the terminology of the plasticity by Eq. (4) or (4'), the normal stress transmitted across a surface element normal to the stress-discontinuity surface being left discontinuous.

The yield condition of the perfectly plastic material, the state of stress of which yields the flow of the nonviscous compressible fluid, can be obtained by solving the differential equation, Eq. (6) or (6'), which becomes, by once integrating,

$$\tau^{-1}p\,|1-\gamma p|^{-\gamma/(\gamma-1)}\,|1-p|^{1/(\gamma-1)} = \text{constant} \tag{7}$$

or

$$\tau^{-1}p\,|1+p|^{-\gamma/(\gamma-1)}\,|1+p|^{1/\gamma-1} = \text{constant} \tag{7'}$$

respectively, and in Fig. 1 there is shown an example of the solutions that have been solved so as to coincide on both σ- and τ-axes with the yield condition in "plane stress" according to M. I. Huber and H. Hencky's theory of constant elastic strain energy of distortion.[1] The astonishing resemblance between these two yield conditions observed in Fig. 1 and, still further, the more precise coincidence that will be seen when the comparison is restricted locally indicate the possibility of the study of the compressible-fluid flow by the plastic deformation of the ductile metals at normal temperature which are considered to obey the above-mentioned theory of strength. Since it is well known that the slip lines are sometimes visible on the surface of the material subjected to plastic flow without any artifice, in other cases they can be brought out by etching; while the isostatics are frequently observed as lines of fracture on the surface of the mate-

FIG. 1. Yield conditions. ————Nonviscous compressible fluid [Eq. (7) for $\sigma \geq 0$ and Eq. (7′) for $\sigma \leq 0$]. - - - - Theory of constant elastic strain energy of distortion (Ellipse).

rial failed by cleavage, we can see various types of the fluid flow by simply pressing the ductile metals in such a way as we like. Although we have confined ourselves so far particularly to the plane problem, the analogy can be extended to the axially symmetric flow. However, its detailed discussions will be reported elsewhere.

When the perfectly plastic material to be used for the analogy does not obey the yield condition satisfying Eq. (7) or (7′), we are to deal with a kind of hypothetical-fluid flow, the pressure-density relation of which is determined by the yield condition of the material considered. Concerning the flow of several kinds of hypothetical fluids which have been introduced to represent the states of stress of the perfectly plastic materials obeying the well-known yield conditions proposed so far, reference should be made to my previous papers.[2–4]

REFERENCES

[1] Nádai, A., *Theory of Flow and Fracture of Solids*, 2nd Ed., Vol. 1, pp. 209–211; McGraw-Hill Book Company, Inc., New York, 1950.

[2] Inoue, N., *Application of the Theory of Supersonic Flow to the Two-Dimensional Isostatical Problem in the Theory of Plasticity*, Journal of the Physical Society of Japan, Vol. 6, No. 6, pp. 460–465, November-December, 1951.

[3] Inoue, N., *On Some Hypothetical Gases*, Journal of the Physical Society of Japan, Vol. 7, No. 1, pp. 119–121, January-February, 1952.

[4] Inoue, N., *Mechanics of Perfectly Plastic and Pulverulent Bodies Studied as a Kind of Gasdynamics*, Doshisha Engineering Review, Vol. 2, No. 2, pp. 85–108, March, 1952 (in Japanese).

Reciprocity Relations in Wing-Body Systems

W. M. Bleakney and G. K. Morikawa*
Research and Development Laboratories, Hughes Aircraft Company, Culver City, Calif.
June 20, 1952

GENERAL RECIPROCITY RELATIONS (reverse-flow theorems) in linearized inviscid flow theory, analogous to the well-known Maxwell's reciprocal theorems, have recently been discussed by several authors—notably, Ursell and Ward,[1] Jones,[2] Flax,[3] and Heaslet and Spreiter.[4] However, with the exception of reference 4, to our knowledge the published discussions have been unnecessarily confined to planar systems, possibly because of difficulty in prescribing reasonable boundary conditions for finite nonplanar systems. We wish to emphasize that, for a large class of practical wing-body systems, the body can be represented as an infinitely long cylinder (or quasi-cylinder) with the body axis nominally in the free-stream direction; in reference 4 the body is apparently restricted to zero angle of attack. Since sufficient background literature exists—e.g., the above references—an heuristic presentation is given here.

Consider an infinitely long cylindrical body with the body axis (x-axis) nominally in the free-stream direction and finite-area planar or curved surfaces (called wings) arbitrarily distributed in the finite space, attached or unattached to the body, but nominally parallel to the body axis. Let $\alpha_B^{(1)}$ and $\alpha_B^{(2)}$ denote arbitrary angle of attack distributions of the body axis for forward and reverse flows respectively. Then, if

$$\alpha_B^{(1)} = \alpha_B^{(2)} = 0 \tag{1}$$

at $x = \pm\infty$,† the integral reciprocity relation, first demonstrated in reference 1 for planar systems, is valid

$$\iint_S [\varphi_x^{(1)}\, \varphi_n^{(2)} + \varphi_x^{(2)}\, \varphi_n^{(1)}]\, dS = 0 \tag{2}$$

where the area of integration S includes both body and wing surfaces. $\varphi^{(1)}$ and $\varphi^{(2)}$ are the perturbation velocity potentials for the forward and reverse flows, respectively, and the subscripts x and n denote differentiations in the x-direction and surface normal direction n, respectively. Further, conditions (1) can be replaced by

$$\left.\begin{aligned} \alpha_B^{(1)}|_{x=-\infty} &= \alpha_B^{(1)}|_{x=+\infty} \\ \alpha_B^{(2)}|_{x=-\infty} &= \alpha_B^{(2)}|_{x=+\infty} \end{aligned}\right\} \tag{3}$$

This is evident since the difference between the boundary value problem given by conditions (3) and that given by conditions (1) is the lifting (or antisymmetric) problem where the body is at constant angle of attack $\alpha_B^{(1)}$ (constant $\alpha_B^{(2)}$ for the reverse flow) and the wings have zero angle of attack. This lifting problem is further reducible to two problems: one, in which the body is at zero angle of attack having wings with apparent twist (body upwash) and, two, in which the body *alone* is at constant $\alpha_B^{(1)}$ (constant $\alpha_B^{(2)}$ for the reverse flow). The first lifting problem satisfies conditions (1) and the second lifting problem satisfies Eq. (2) identically.

We give several interesting consequences of this extension for lifting wing-body and wing-body-tail systems, where "lift" is used to mean cross-wind force in the plane of the angle of attack; "sideforce" is the cross-wind force at right angles to lift; "component angle of attack" is the angle of rotation of a component, such as a section of body with attached wings, from zero incidence with the free stream; "system angle of attack" is the corresponding angle for the entire wing-body system; and "local angle of attack" is the angle of incidence of an element of surface area to the free stream.

(1) For a cylindrical body with wings and with nose and base beyond the range of wing interference, the magnitude of the lift on a component due to angle of attack of that component is unchanged by flow reversal, provided nose and base are interchanged at the same time.

(2) With the same limitations on wings and body, the sideforce on a component per unit component angle of attack in any plane is equal to the sideforce on the component in reversed flow per unit component angle of attack at right angles to that plane. It may be shown independently of Eq. (1), from symmetry considerations alone, that this relationship holds without flow reversal if the configuration and the component possess a common plane of symmetry.

(3) The "components" in (1) and (2) may be the entire system.

(4) Subject to the same limitations on wings and body, the magnitude of the interference lift from any pair of components is unchanged by flow reversal.

(5) The wing portion of the lift $L_W^{(1)}$ for a wing-body system where the body is at α and wing at zero angle of attack is equal to the body portion of the lift $L_B^{(2)}$ for the same wing-body system in reverse flow where the body is at zero angle of attack and the wing has the component angle of attack α in the same plane.

(6) It follows immediately from (5) that the total lift $L^{(2)}$ for the wing-body system where the wing is at α and body at zero angle of attack can be expressed as

$$L^{(2)} \equiv L_B^{(2)} + L_W^{(2)} = L_W^{(1)} + L_W^{(2)} \tag{4}$$

* Now with Office of Naval Research, Mathematical Sciences Division.

† Actually the conditions can be $\alpha_B^{(1)} = 0$ at $x = -\infty$ and $\alpha_B^{(2)} = 0$ at $x = +\infty$, but we see no advantage gained by these weakened conditions.

Usually, better approximations are available for the wing portion of the lift of wing-body systems.

(7) The spanwise lift distribution on the wing of a wing-body system where both body and wing are at a system angle of attack α is equal to the spanwise lift-influence function (cf. reference 5) for the same wing-body system in reverse flow where both body and wing are at zero angle of attack, excepting an infinitesimal chordwise strip on the wing which has a component angle of attack α in the same plane. If the wing is plane and normal to the angle of attack plane, the component angle of attack becomes the local angle of attack.

References

[1] Ursell, F., and Ward, G. N., *On Some General Theorems in the Linearized Theory of Compressible Flow*, Quarterly Journal of Mechanics and Applied Mathematics, Vol. III, Pt. 3, September, 1950.

[2] Jones, R. T., *The Minimum Drag of Thin Wings in Frictionless Flow*, Journal of the Aeronautical Sciences, Vol. 18, No. 2, p. 75, February, 1951.

[3] Flax, A. H., *Reverse-Flow and Variational Theorems for Lifting Surfaces in Non-Stationary Compressible Flow*, Cornell Aeronautical Laboratory Report, CAL-42, February, 1952.

[4] Heaslet, M. A., and Spreiter, J. R., *Reciprocity Relations in Aerodynamics*, N.A.C.A. T.N., No. 2700, May, 1952.

[5] Morikawa, G. K., and Puckett, A. E., *Equivalence of the Spanwise Lift Distribution to the Lift-Influence Function for Slender Wings and Wing-Bodies*, Readers' Forum, Journal of the Aeronautical Sciences, Vol. 18, No. 7, p. 503, July, 1951.

On the Kirchhoff Solution for an Oscillating Wing in Subsonic Compressible Flow

John W. Miles

Associate Professor of Engineering, University of California at Los Angeles

August 1, 1952

In a recent report,[1] Timman has applied Kirchhoff's method to the boundary value problem for a two-dimensional airfoil executing a high-frequency ($k \gg 1$) oscillation in a subsonic compressible flow. It is our opinion that, since he fails to include the Kutta condition in his formulation, his end results are incomplete. Fortunately, this omission is easily remedied along the lines indicated below.

In the interests of brevity, we shall follow Timman's notation and simply state the boundary-value problem to be considered. Let $\exp(iMkx)\psi$ be the velocity potential, where M is the Mach Number and k is a reduced frequency parameter (but not the usual U.S. definition). Then ψ satisfies the wave equation

$$\psi_{xx} + \psi_{yy} + k^2\psi = 0 \tag{1}$$

to which a solution is to be found subject to the boundary conditions

$$\psi_y = e^{-iMkx}\, w(x), \qquad |x| < a,\ y = 0^+ \tag{2}$$

$$\psi = 0, \qquad x < -a,\ y = 0^+ \tag{3}$$

$$\psi_x + (ik/M)\psi = 0, \qquad x \geq a,\ y = 0^+ \tag{4}$$

corresponding to a prescribed downwash (w) at the wing, continuity of the potential forward of the wing and continuity of the pressure across the wake. The (strong) Kutta condition is prescribed by invoking Eq. (4) at $x = a$ (the trailing edge), as well as for $x > a$ (the wake).

The classical diffraction problem differs from that defined by Eqs. (1)–(4) only in having the simpler boundary condition $\psi = 0$ for $x > a$. The Kirchhoff approximation then replaces the boundary condition $\psi = 0$ by $\psi_y = 0$ on $y = 0$, $|x| > a$. It appears to the writer that this approximation may be expected to have the same (frequency) régime of validity in the airfoil problem only if an eigensolution is added to cancel the singularity exhibited by the pressure at the trailing edge, thereby satisfying (in the weak sense) the Kutta condition.

In order to obtain the required eigensolution, we write

$$\psi(x,y) = \psi_T(x,y) + \int_{-a}^{x} \exp\,[(ik/M)\,(\xi - x)]\ \chi(\xi,y)\,dy \tag{5}$$

where ψ_T is Timman's solution, and χ is a solution to Eq. (1) satisfying the boundary conditions

$$\chi_y = 0, \qquad x \neq a,\ y = 0 \tag{6}$$

$$\psi_x + (ik/M)\psi = \psi_{Tx} + (ik/M)\psi_T + \chi \neq \infty, \qquad x = a,\ y = 0 \tag{7}$$

The requirement (6) implies that, since ψ_T satisfies Eq. (2), it remains satisfied by Eq. (5), while Eq. (7) is the (weak) Kutta condition.

The required solution for χ is evidently a source at $x = a$ and is given by

$$\chi = CH_0^{(2)}[k|(x-a)^2 + y^2|^{1/2}] \tag{8}$$

Substituting Eq. (8) in Eq. (7) and thereby determining the constant C, we find that the pressure jump corresponding to χ is given by

$$\left(\frac{p_+ - p_-}{\rho}\right)_x = iV(1 - M^2)^{-1/2}\, w(a) \exp\,[ivt + iMk(x-a)]\ H_0^{(2)}[k(a-x)] \tag{9}$$

and just cancels the corresponding term in Timman's result [Eq. (4.1), reference 1].

It should be remarked that the end solution for the pressure, obtained by adding Eq. (9) to Timman's result, still does not give zero pressure at the trailing edge (strong Kutta condition), as would be the case for the exact solution. This is due to the fact that the Kirchhoff approximation does not satisfy the boundary conditions for $|x| > a$. Nevertheless, it would appear that the suggested modification of Timman's solution furnishes a logical extension of the Kirchhoff approximation to the airfoil problem.

Reference

[1] Timman, R., *Approximate Theory of the Oscillating Wing in Compressible Subsonic Flow for High Frequencies*, Rep. F-99, Nationaal Luchtvaartlaboratorium, 1951.

Experiments with Large Pitot Tubes in a Narrow Supersonic Wake

N. H. Johannesen and W. A. Mair

Fluid Motion Laboratory, University of Manchester, England

July 25, 1952

Introduction

At low air speeds, the behavior of a pitot tube in a transverse total-pressure gradient was investigated by Young and Maas[1] in 1936. They found that the point at which the total pressure was effectively measured was displaced toward the region of higher velocity. For a number of widely different conditions, this displacement was equal to $0.18D$, where D is the external diameter of the pitot tube.

In the course of an investigation of two-dimensional *supersonic* wakes, experiments were made to investigate the effect of the finite size of the pitot tube. In other investigations, the effect of varying the tube diameter has been found to be small, but only relatively small diameters have been considered. The present experiments were extended to include large tube diameters and showed that at supersonic speeds there is hardly any effect of the kind found by Young and Maas.

TABLE 1

Tube	External Diameter, D, In.	Internal Diameter, d, In.	D/d
A	0.036	0.026	1.4
B	0.095	0.068	1.4
C	0.375	0.268	1.4
D	0.720	0.515	1.4
E	0.095	0.015	6.3
F	0.720	0.030	24

EXPERIMENTS

The experiments were made in a small intermittent supersonic tunnel with working section 4 by 5 in., free-stream Mach Number 1.96, and Reynolds Number 3.3×10^6 per in. A wedge of 20° apex angle with $^3/_4$-in. chord was set at zero incidence, and its wake was traversed with pitot and static tubes at a distance 2.5 in. downstream of the trailing edge. The static pressure was sensibly constant across the wake. The diameters of the pitot tubes are given in Table 1.

In Figs. 1 and 2, the dimensionless ratio P/H of pitot pressure to free-stream stagnation pressure is plotted against distance y across the wake. The condition of symmetry was taken into account in drawing the curves.

The curves for Tubes B and E are not shown in the figures, but they both coincided with the curve for Tube A.

The slight differences in the levels of the curves outside the wakes are of the same order of magnitude as the day-to-day variations of Mach Number in the tunnel (about $^1/_4$ per cent). The pressures near the edge of the wake were rather unsteady, and average readings were used. It will be seen that the curves have *maximums* just outside the wakes. This is because the stream lines in these regions have passed through the fan-shaped foot of the shock wave behind the trailing edge, where the compression is more efficient than in the single shock wave further away from the wake.

DISCUSSION OF RESULTS

Fig. 1 shows that, for a constant value of the ratio D/d (= 1.4), variations of external diameter up to about 0.4 in. have a negligible effect on the apparent width of the wake. However, when D is about 0.7 in., the wake profile is considerably distorted. These tube diameters should be compared with the actual width of the wake (about 0.1 in.). The difference in the peak values of P/H at the center of the wake for Tubes A and C is perhaps not significant and may be caused by a small change in free-stream Mach Number.

Fig. 2 shows a comparison between Tubes A and F, having approximately the same internal diameter but with external diameters differing by a factor of 20. The curves show that the effect of variation of D, with constant d, is small indeed. (In this case, also, the difference in the peak values at the center of the wake may not be significant.)

Comparison of Tubes D (Fig. 1) and F (Fig. 2) shows that for large values of D the internal diameter is of major importance. As already mentioned, the curves for Tubes B and E did not show any significant difference; thus, the effect of varying d is negligible for small values of D.

The results may be summarized as follows. For values of D up to about 0.4 in. (i.e., about four times the wake width), the effects of variation of D and d are hardly detectable. With a tube having an external diameter as large as 0.7 in., the wake profile is considerably distorted if the internal hole is correspondingly large (D/d = 1.4), but with a small internal hole even this large tube gives almost the same wake profile as a much smaller tube. It was not possible to investigate much larger values of D without choking the tunnel.

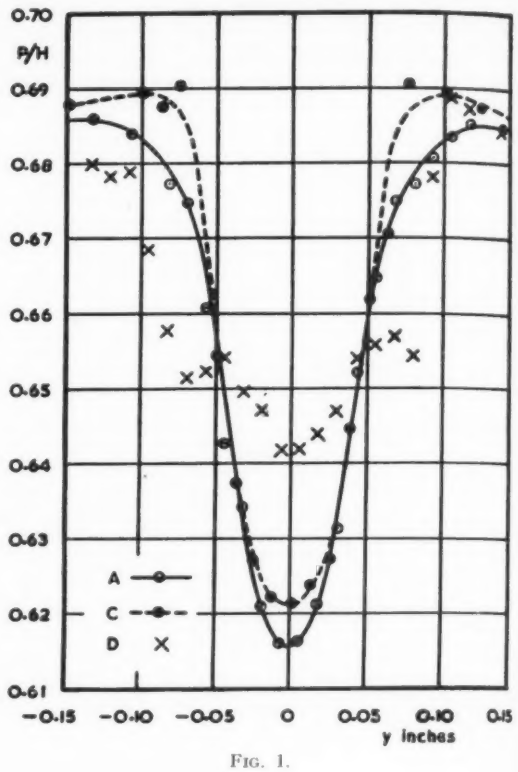

FIG. 1.

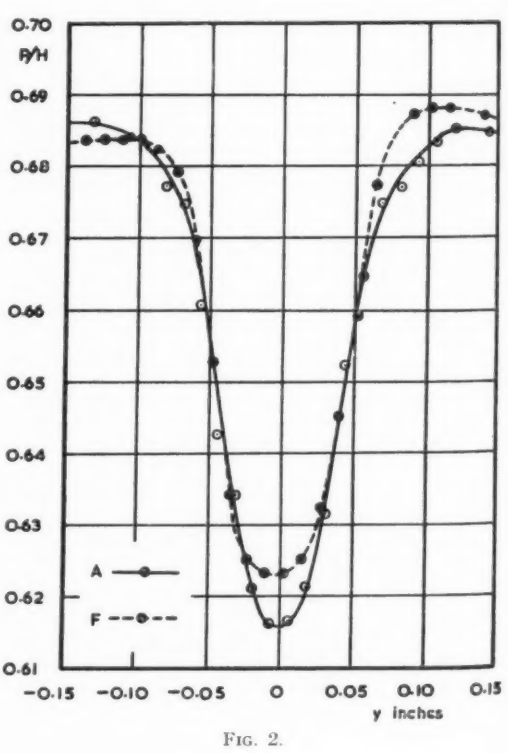

FIG. 2.

In these experiments no displacement effect as found by Young and Maas could be detected. Hence, any effect of this kind must be no larger than the scatter of the experimental points and, thus, is much less than the displacement at low speeds. If a tube as large as Tube C were used to explore a wake of this width at low speeds, the Young and Maas correction to the wake width would be of the same order as the wake width itself. (However, the correction given by Young and Maas would require modification in an extreme case such as this, where the tube diameter is much larger than the total wake width.)

Although the explanation of these results is not understood, a simple consideration of the effects of the normal shock wave in front of the pitot tube shows that the problem is quite different from the corresponding one at low speeds. Immediately behind the shock wave there must be a peak of *high* velocity at the center of the wake. At the same time there must be considerable curvature of the stream lines associated with the variations of static pressure behind the shock wave. Thus, the initial conditions for the (subsonic) flow into the mouth of the pitot tube are quite different when the free stream is supersonic.

Reference

[1] Young, A. D., and Maas, J. N., *The Behaviour of a Pitot Tube in a Transverse Total-Pressure Gradient*, Brit. A.R.C., R. & M. No. 1770, 1936.

Computing Critical Loads by Splitting the Rigidity of Composite Systems

F. Buckens
Professor of Applied Mechanics, University of Louvain, Belgium
July 18, 1952

It seems interesting, when noting Bijlaard's papers on the stability of sandwich plates,[1] to point out that the splitting considered there occurs, in fact, in two different ways. The first stage is really a splitting of rigidities; in partial system (1), the core retains its rigidity, as well as the external plates, except for its flexural rigidity, while the reverse is assumed for the partial system (2). If P_1 and P_2 are the first buckling loads of these partial systems, their sum provides an inferior limit for the first critical load of the real system,

$$P_{cr} \geq P_1 + P_2 \tag{1}$$

This is a particular case of Temple's generalization of Southwell's well-known method.[2] The second stage of splitting in the papers of reference 1 consists of dividing the "elasticity" (and not the rigidity) of the partial system (1) into two subsystems. In the first (1′), only shear elasticity of the core is considered, while in the second (1″), longitudinal elasticity of the external plates alone is taken into account (flexural rigidity of the core being neglected). Still, without rigorous proof, an analogous procedure had been used by Bijlaard in a previous paper[3] to reestablish Engesser's approximate formula for the critical load of a latticed structure.

As can be found along the lines of a general theorem given by Temple,[2] one gets the following inequality:

$$P_1^{-1} \leq P_1'^{-1} + P_1''^{-1} \tag{2}$$

when P_1' and P_1'' are the critical loads in the partial subsystems (1′) and (1″).

For example, if the differential equation takes the form

$$(d^2y/dx^2) + [Py/\alpha(x)] = 0$$

it suffices to admit that the inverse of the rigidity $\alpha(x)$ can be decomposed:

$$1/\alpha(x) = [1/\alpha'(x)] + [1/\alpha''(x)]$$

In this manner, combining Eqs. (1) and (2), one obtains

$$P_{cr} \geq (P_1'^{-1} + P_1''^{-1})^{-1} + P_2 \tag{3}$$

By virtue of Rayleigh's theorem, inferior limits (1) and (2) usually provide good approximations at the same time.

Besides including Dunkerley's formula for the decomposition of the mass in problems of natural frequencies or whirling speeds, Temple's method applies to systems whose "internal" elasticity can be subdivided into several partial systems and yields

$$\lambda_1^{-1} \leq \sum_k \lambda_{1k}^{-1} \tag{4}$$

where λ_1 and λ_{1k} represent, respectively, the fundamental eigenvalues of the real system and of the kth partial system; for instance, λ is the square of the natural frequency (ω^2) of the critical load (P).

Eq. (4) had been independently established by the author, with some more generality, by a decomposition of "influence coefficients."[4] By this method, "external elasticity"—i.e., elasticity of the boundaries—can *also* participate in the decomposition in order to form partial systems that are easier to solve. The papers in reference 4 give several examples for vibration and stability problems; more generally, when the eigenvalue problem can be put into the form of an integral equation,

$$y(x) = \lambda \int K(x, \xi) y(\xi)\, d\xi \tag{5}$$

where $K(x,\xi)$ is a symmetric kernel that characterizes the given system, if partial systems with kernels $K_k(x,\xi)$ can be derived such that

$$\sum_k K_k(x,\xi) = K(x,\xi) \tag{6}$$

then the fundamental eigenvalue λ_1 of the real system can be assigned an inferior limit of the form of Eq. (4).

References

[1] Journal of the Aeronautical Sciences, Vol. 18, Nos. 5 and 12, May and December, 1951, and references thereof.

[2] Proceedings of the London Math. Soc., II Ser., Vol. 29, 1929 (pp. 272 and 267, respectively).

[3] De Ingenieur in Nederlandsh—Indie, 6, Nr. 3, p. 46, 1939.

[4] Bulletin Techn. de l'Union des Ing. de Louvain, 1941. Publications of the International Association for Bridge and Structural Engineering, 7th Vol., p. 61, 1943–1944 (Zürich).

On Heat Transfer, Recovery Factors, and Spin for Laminar Flows*

Arthur N. Tifford and Sheng To Chu
The Ohio State University, Columbus
July 25, 1952

In March, 1950, an O.A.R.†-sponsored research program on the effect of surface pressure and temperature gradients on the characteristics of the laminar boundary layer was begun at The Ohio State University. The initial effort was directed at completing the computational coverage of the analytic results for wedges. The Computation Section of the O.A.R. at Wright-Patterson Air Force Base did the computing on their Reeves analog computers.

About 25 per cent of the computations of references 1 and 2 deal with the same values of the parameters. The two sets of function values obtained agree within 1 per cent. Thus, the two systematic computation programs conveniently supplement each other.

* Work supported by The Flight Research Laboratory, U.S.A.F.
† Office of Air Research, U.S.A.F.

TABLE 1*

TEMPERATURE RECOVERY ON INSULATED SURFACES

σ =	0.5	0.7	1.0	2.0
β	$(T_a - T_1)/(u_1^2/2gc_pJ)$			
−0.1988	0.706	0.844	1.004	1.428
−0.14	0.714	0.850	1.016	1.443
0	0.718	0.846	1.018	1.442
0.5	0.712	0.846	1.012	1.418
1.0	0.710	0.844	1.008	1.424
2.0	0.708	0.840	1.006	1.424
$\sigma^{1/2}$ =	0.707	0.837	1.000	1.414

* T_a = temperature acquired by insulated surface
T_1 = local free-stream temperature
u_1 = local free-stream velocity
c_p = specific heat at constant pressure
g, J = dimensional constants
σ = Prandtl Number
β = pressure gradient parameter

We were interested to note in the report of reference 3 that the calculated recovery factor for a separating laminar boundary layer is significantly lower than for other laminar boundary layers. In Table 1, we have reproduced our earlier analog-computed results. On the basis of these, we had concluded that Pohlhausen's square-root rule is just as valid for gas flows involving local surface pressure gradients as for the classical flow along a flat plate aligned with the gas stream. No exception was made of the separating boundary layer.

In attempting to resolve this conflict, we reviewed the numerical integration method used in reference 3. It is simply a direct application of the automatic integration method of reference 4, supplemented by the procedure, described in these pages in reference 5, for solving two-point boundary value, linear, total differential equations without recourse to trial and error. The integration procedure of reference 4, however, does not allow an *a priori* specification of the boundary value at infinity of the supplementary function, g. A study of the properties of the primary sfunction, θ, near the outer edge of the boundary layer is necesOary to determine just what that boundary value properly is. nly after it has been shown that θ approaches zero faster than $\exp(-\sigma \int_0^\eta f\, d\eta)$, as η approaches infinity, is it certain that g approaches zero there.

In studying this question, we have related the g function asymptotically to the Whittaker function.[6] The boundary value, zero, has been confirmed. We conclude that nothing is wrong with the integration method used in reference 3. The possibility always exists, however, that the coding of the problem for the machine—or the machine itself—is in error.*

As a by-product of the above study, we noticed that a differencing method of integration with a precision comparable to that of the method of reference 4, and without the disadvantage at infinity noted above, is readily obtainable. Thus, by adding and subtracting the two Taylor series,

$$\theta_n = \theta_{n-1} + e\theta_{n-1}' + (e^2/2)\,\theta_{n-1}'' + (e^3/3!)\,\theta_{n-1}''' + (e^4/4!)\theta_{n-1}'''' + \ldots$$

$$\theta_{n-2} = \theta_{n-1} - e\theta_{n-1}' + (e^2/2)\,\theta_{n-1}'' - (e^3/3!)\,\theta_{n-1}''' + (e^4/4!)\,\theta_{n-1}'''' - \ldots$$

we obtain

$$\theta_{n-1}'' = (1/e^2)\,[\theta_n - 2\theta_{n-1} + \theta_{n-2} - (e^4\theta_{n-1}''''/12) - \ldots]$$

$$\theta_{n-1}' = (1/2e)\,[\theta_n - \theta_{n-2} - (e^3/3)\theta_{n-1}''' - \ldots]$$

respectively, where e is the size of the step in the integration.

* In order to throw more light on the subject, we have performed some numerical integrations with a precision of about ½ per cent and obtained a recovery factor of 0.836 for the separating boundary layer. Thus, we check the analog computation of the O.A.R. within 1 per cent.

Substituting these equivalents for θ_{n-1}'' and θ_{n-1}' into the original second-order differential equation, we obtain a difference equation for θ_n in which the dominant extrapolation error is proportional to e^4. The application of this method to the computations of reference 1 involves no additional complication and reduces the dominant error from $[f\sigma(e^3/2)]\theta_{n-1}''$ to $[f\sigma(e^4/6)]\theta_{n-1}'''$. The improvement is wholly due to the more correct difference representation of the first derivative, θ_{n-1}'.

We should like to report here, too, one of our earlier analytic findings: As an interesting application of the order-of-magnitude argument, note that, for large values of γ, the second term in the equation

$$(1/\sigma)\theta'' + f\theta' - (2 - \beta)\gamma f'\theta = 0$$

may be neglected as compared with the third. It is now evident that the effect of large values of γ on the thermal boundary-layer function is the same as that of large Prandtl Numbers. In other words, the thermal boundary layer is thin as compared with the velocity boundary layer. Accordingly, the velocity profile within the former may be taken as linear, in general, and as parabolic in the case of a separating boundary layer.

The analytic solutions for θ are easily obtained under these circumstances. They involve modified Bessel functions of the second kind (see reference 7). The solid curve of Fig. 1 represents the universal solution for the nonseparating boundary layer for large positive values of γ. Superimposed are data obtained from the calculations of Chapman and Rubesin[8] for the case of the flat plate. It is seen that, for γ values near 10 (and larger), the Bessel function representation of the temperature profile is excellent.

Similar analyses for large negative values of γ also lead to Bessel function solutions. However, in these cases θ is found to oscillate between positive and negative values as one moves away from the surface. Furthermore, there is no well-defined thermal boundary layer. It has been concluded that the solutions for large negative values of γ are not physically realizable. It appears in fact, in contradiction to the assertions of reference 1, that, when the value of $\gamma\ (2 - \beta)$ is assumed more negative than -1, the solutions are physically unreal. In such cases the analysis would require an infinite heat source at the origin.

Another possible application of some of the computational results is the determination, by means of them, of the frictional resistance to spin of axisymmetric bodies. This extension of the analysis of reference 9 will be elaborated upon in a forthcoming U.S. Air Force Technical Report.

Fig. 1. Universal Bessel Function Representation of Thermal Boundary Layer Characteristics at Large Values of "γ"

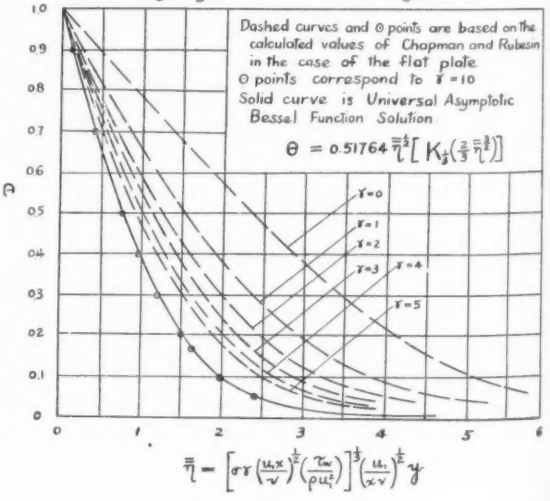
Dashed curves and θ points are based on the calculated values of Chapman and Rubesin in the case of the flat plate
θ points correspond to γ = 10
Solid curve is Universal Asymptotic Bessel Function Solution
θ = 0.51764 η̄^½ [K_⅓(⅔ η̄^{3/2})]
γ=0
γ=1
γ=2
γ=3
γ=4
γ=5
θ
η̄ = [σγ (u₁x/ν)^½ (τ_w/ρu₁²)]^⅓ (u₁/νx)^½ y

References

[1] Levy, S., *Heat Transfer to Constant-Property Laminar Boundary Layer Flows with Power-Function Free-Stream Velocity and Wall-Temperature Variation*, Journal of the Aeronautical Sciences, Vol. 19, No. 5, pp. 341–348, May, 1952.

[2] Tifford, A. N., and Chu, S. T., *Heat Transfer in Laminar Boundary Layers Subject to Surface Pressure and Temperature Distributions*, Proceedings of the Second Midwestern Conference on Fluid Mechanics (published October, 1952).

[3] Levy, S., and Seban, R. A., *Recovery Factors for the Laminar "Separation" and Stagnation Flows*, Readers' Forum, Journal of the Aeronautical Sciences, Vol. 19, No. 5, pp. 355–357, May, 1952.

[4] Feinstein, L., and Schwarzschild, M., *Automatic Integration of Linear Second Order Differential Equations by Means of Punched Card Machines*, The Review of Scientific Instruments, Vol. 12, No. 8, pp. 405–408, August, 1941.

[5] Tifford, A. N., *On the Solution of Total Differential, Boundary Value Problems*, Readers' Forum, Journal of the Aeronautical Sciences, Vol. 18, No. 1, pp. 65–66, January, 1951.

[6] Whittaker, E. T., and Watson, G. N., *Modern Analysis*, Chapt. XVI; The Macmillan Company, New York, 1946.

[7] McLachlan, N. W., *Bessel Function for Engineers*, Chapt. VII; Oxford University Press, 1941.

[8] Chapman, D. R., and Rubesin, M. W., *Temperature and Velocity Profiles in the Compressible Laminar Boundary Layer with Arbitrary Distribution of Surface Temperature*, Journal of the Aeronautical Sciences, Vol. 16, No. 9, pp. 547–565, September, 1949.

[9] Tifford, A. N., *Letter to the Editor*, Journal of the Aeronautical Sciences, Vol. 15, No. 8, pp. 280–281, May, 1948.

Remarks on "On the Flight Dynamics of Slender Special-Purpose Aircraft"

F. Niedenfuhr

Vibration and Flutter Unit, Aerophysics Laboratory, North American Aviation, Inc., Downey, Calif.

June 16, 1952

THE AUTHORS OF REFERENCE 1 consider a nonrolling aircraft and remark in a footnote: "It is not an entirely trivial matter to show the nonexistence of the roll equation because Eq. (4) shows that a roll acceleration does exist even when $p(t) \equiv 0$, and there are undoubtedly nonvanishing forces due to many of the variables that contribute to the roll torque."

Eq. (4) of the paper, when considered in detail, is seen to be in error, however. Repeating the essentials of the derivation, one has:

The velocity of a point P, located at $\bar{r}$ is

$$\bar{v} = (d\bar{r}/dt) + \bar{\omega}\bar{r} \tag{a}$$

(not $\bar{v} = \bar{\omega}\bar{r}$) so that

$$\left.\begin{aligned} v_x &= (z+\tau)q - (y+\sigma)r \\ v_y &= xr + \dot{\sigma} \\ v_z &= -xq + \dot{\tau} \end{aligned}\right\} \tag{b}$$

The angular momentum $\bar{\lambda}$, is given by

$$\bar{\lambda} = \bar{r}\, dm\, \bar{v} \tag{c}$$

so that neglecting products of vibrational displacements, one has

$$\left.\begin{aligned} \lambda_x &= \int\{(y+\sigma)(-xq+\dot{\tau}) - (z+\tau)(xr+\dot{\sigma})\}\, dm \\ \lambda_y &= \int\{(z+\tau)[(z+\tau)q - (y+\sigma)r] - x(-xq+\dot{\tau})\}\, dm \\ \lambda_z &= \int\{x(xr+\dot{\sigma}) - (y+\sigma)[(z+\tau)q - (y+\sigma)r]\}\, dm \end{aligned}\right\} \tag{d}$$

Then,

$$dL = (d\lambda_x/dt) + q\lambda_z - r\lambda_y \tag{e}$$

$$\begin{aligned} dL = \int\{&-xyq + y\ddot{r} - \sigma x\dot{q} - \dot{\sigma}xq - zx\dot{r} - z\ddot{\sigma} - \dot{\tau}xr - \\ &r x\dot{r} + qx(xr+\dot{\sigma}) - (\sigma+y)(z+\tau)q^2 + (y+\sigma)^2 rq - \\ &(z+\tau)^2 rq + (\sigma+y)(z+\tau)r^2 + rx(-xq+\dot{\tau})\}\, dm \end{aligned} \tag{f}$$

$$\begin{aligned} dL = \int\{&-x\dot{q}(y+\sigma) - x\dot{r}(z+\tau) + y\ddot{r} - z\ddot{\vartheta} + \\ &(y+\sigma)(z+\tau)(r^2-q^2) + rq[(y+\sigma)^2 - (z+\tau)^2]\}\, dm \end{aligned} \tag{g}$$

$$L = \int_l dL \tag{h}$$

The elements of dL given by Eq. (g) are seen to be the same as obtained by the authors, except for the presence of $y\ddot{r}$ and $z\ddot{\sigma}$ and the absence of $qx\dot{\sigma}$ and $rx\dot{r}$. Integration over the length of the airplane of $y\ddot{r}$ and $z\ddot{\sigma}$ is zero by the authors' Eq. (2), and $qx\dot{\sigma}$ and $rx\dot{r}$ are cancelled out completely in Eq. (f) above. For an aircraft that is truly slender and symmetrical, $C = B$, so that Eq. (4) should read

$$a_\varphi = 0 \tag{i}$$

The question of whether or not to include the roll degree of freedom remains to be examined. Roll torques do exist because of the other degrees of freedom, as the authors assert. If the rigid body coordinates, p, q, r, u, v, and w are restricted to be quantities of perturbation order (whose squares and products can be neglected) as is done in the conventional stability analysis, Eq. (4) can be written

$$a_\varphi = \dot{p} \tag{j}$$

and the gyroscopic couplings and terms involving Mathieu functions referred to in the first part of the article will all be seen to be of higher order. To the first order in small quantities, then, the equations of motion for all degrees of freedom (roll and twist included) of a flexible aircraft will be a set of linear differential equations with constant coefficients.

Reference

[1] Rosenberg, R. M., and Stoner, George, *On Flight Dynamics of Slender Special-Purpose Aircraft*, Journal of the Aeronautical Sciences, Vol. 19, No. 1, p. 29, January, 1952.

Authors' Reply

R. M. Rosenberg and George Stoner

We wish to thank Mr. Niedenfuhr for his illuminating remarks. Insofar as they pertain to Eq. (4) and the footnote of our paper they are quite correct. In particular, we agree that the acceleration term in the roll equation vanishes identically for the case considered by us. However (and Mr. Niedenfuhr agrees), roll torques due to degrees of freedom other than roll remain. In view of this, we should still have added a footnote (reflecting essentially the sense of the one published) in order to warn against ignoring an equation that appears to have nonzero members. Yet, the actual demonstration of deleting the roll equation from the system is so simple as to deserve no more attention than a remark in a footnote. Fortunately, Mr. Niedenfuhr's correct observation does not invalidate the results of our paper.

While agreement exists between the discusser and us regarding the footnote in question, we believe that a further point raised by Mr. Niedenfuhr merits more detailed examination. The terms involving "gyroscopic couplings and . . . Mathieu functions" (the latter should read "periodic coefficients") are said to be of higher order. As a matter of fact, the indicated terms are of higher order *only* when rolling displacements of perturbation magnitude are considered. If the investigation is concerned with perturbations in roll *superimposed on steady roll*—i.e., if we are searching for solutions in the neighborhood of steady-state solutions which include roll—then first-order terms with periodic coefficients do arise (on the simplified premise that the plane of vibrations remains fixed in space while the missile rolls). However, let us assume with Mr. Niedenfuhr that the terms with periodic coefficients are of higher order. We believe it to be dangerous advice to conclude that these terms may be ignored in a conventional stability analysis.

Consider, for instance, the equation

$$\ddot{x} + a^2 x = x^2 \sin bt \tag{1}$$

(a, b = constants). It will be noticed that the equation contains a

second-order term with a periodic coefficient of frequency b. If we substitute

$$x = x_0 + \xi, \qquad |\xi| << |x_0|$$

for all t, where x_0 is some value of x and ξ is a time-dependent variable in a small neighborhood of x_0, then the equation becomes

$$\ddot{\xi} + a^2\xi = (x_0^2 + 2x_0\xi) \sin bt - a^2x_0 \tag{2}$$

where higher order terms in ξ have been neglected.

Now, the related equation

$$\ddot{\xi}_0 + a^2\xi_0 = x_0^2 \sin bt - a^2x_0 \tag{3}$$

has the steady-state solution

$$\xi_0 = [x_0^2/(a^2 - b^2)] \sin bt - x_0 \tag{4}$$

Since Eq. (4) is the solution to Eq. (3), it cannot satisfy Eq. (2). Let us search for solutions to Eq. (2) of the form

$$\xi = \xi_0(t) + \eta(t) \tag{5}$$

Substitution of Eq. (5) in Eq. (2) will show that $\eta(t)$ is the solution of the Mathieu equation

$$\ddot{\eta} + (a^2 - 2x_0 \sin bt)\eta = [x_0^3/(a^2 - b^2)] \times (1 - \cos 2bt) - 2x_0^2 \sin bt \tag{6}$$

Since the solution of Eq. (1) is now

$$x(t) = x_0 + \xi_0(t) + \eta(t) \tag{7}$$

it follows that $x(t)$ is stable or unstable with $\eta(t)$. This observation does not include the possibility that $x(t)$ is also unstable with $\xi_0(t)$ for the possible case (by no means excluded) that $a = b$. Had we neglected the higher order term in Eq. (1), we should have found

$$x = A \sin (at + \varphi) \tag{8}$$

A, φ = constants, which is never unstable. Therefore, the deletion of higher order terms with periodic coefficients is not advisable in conventional stability analyses.

Lest it be thought that this conclusion depends on the implied condition $x_0 \neq 0$, we indicate a similar result that does not depend on x_0. Let it be supposed that the solution to Eq. (1) lies in the neighborhood of that to the mutilated equation which results when the second-order term of Eq. (1) is discarded. Then, the solution to the actual equation may be written as

$$x = A \sin at + \zeta(t) \tag{9}$$

and powers of ζ higher than the first may be neglected. (Difficulties arising at or near a zero of $A \sin at$ are easily overcome by a shift of the t-axis.) It can be shown without difficulty that, now, $\zeta(t)$ must satisfy the Mathieu equation

$$\ddot{\zeta} + \{a^2 - 2A[\cos (a - b)t - \cos (a + b)t]\}\zeta = (1/2)A^2\{\sin bt - (1/2)[\sin (2a + b)t - \sin (2a - b)t]\} \tag{10}$$

Again, the solution of Eq. (1) is seen to be stable or unstable with that of a Mathieu equation.

Returning to the case with the solution as given in Eq. (7), another significant difference emerges between Eqs. (7) and (8) if our concern is the general behavior of the solution in the neighborhood of x_0 rather than merely its stability. The former reveals the presence in the solution of a periodic term of frequency b having the large amplitude $x_0^2/(a^2 - b^2)$, while the latter, obtained by a "linearization" that simply ignores higher order terms, is of frequency a.

These considerations throw serious doubt on the view that the solution of a set of linear differential equations with constant coefficients reflects the behavior and stability of a flexible aircraft that is permitted to roll. These same thoughts have led us to consider a system lacking periodic coefficients altogether rather than one where their presence must be ignored if the equations are to remain tractable.

Reply to Fettis' Comments on "Aerodynamic Coefficients of an Oscillating Airfoil in Two-Dimensional Subsonic Flow"

R. Timman, A. I. van de Vooren, and J. H. Greidanus
National Aeronautical Research Institute, Amsterdam, Holland
July 22, 1952

IN THE MAY ISSUE of the JOURNAL, Fettis comments[1] on the numerical data published in the subject paper.[2] Fettis remarks that it is difficult to believe that our coefficients are more accurate than those of Dietze for the following reasons:

(1) Dietze's results have been confirmed independently by Fettis' method.

(2) The quantity $[L_h]_R = k_a'/\omega^2$ should, according to Fettis, approach the value 1 for $\omega \to \infty$, while our coefficient has 0 as limiting value.

(3) According to Fettis, the relation

$$k_a = i\omega(m_a + k_h)$$

should be satisfied, and this is not the case for our coefficients.

With regard to the first remark, it may be emphasized that both Dietze's and Fettis' results are obtained by an approximate solution of Possio's integral equation, while our coefficients have been computed by aid of an exact analytical theory. As neither Dietze nor Fettis gives exact estimates of the errors in his results, the accuracy of his coefficients remains doubtful. In fact, it is known that Dietze's iteration procedure does not converge if ω exceeds 0.7 (and $M = 0.7$), while the approximation of the kernel used in the evaluation of certain integrals may very well generate convergence to an erroneous value if ω is smaller than 0.7. The different approximation of the kernel by Fettis may have a similar effect.

Concerning the second remark, it must be noted that the asymptotic value $[L_h]_R = 1$ if $\omega = \infty$ (corresponding to the virtual mass of the airfoil) only holds in incompressible flow. In compressible flow, however, an oscillating airfoil behaves like a moving acoustic radiator, and a mathematical approximation method,[3] valid for high frequencies and based on common assumptions used in the diffraction theory of acoustic waves, confirms the fact that $[L_h]_R \to 0$ if $\omega \to \infty$. That the concept of virtual mass is essentially modified in compressible flow has also been shown by Miles[4] and Longhorn.[5] Curves of $[L_h]_R$ against $1/\omega$

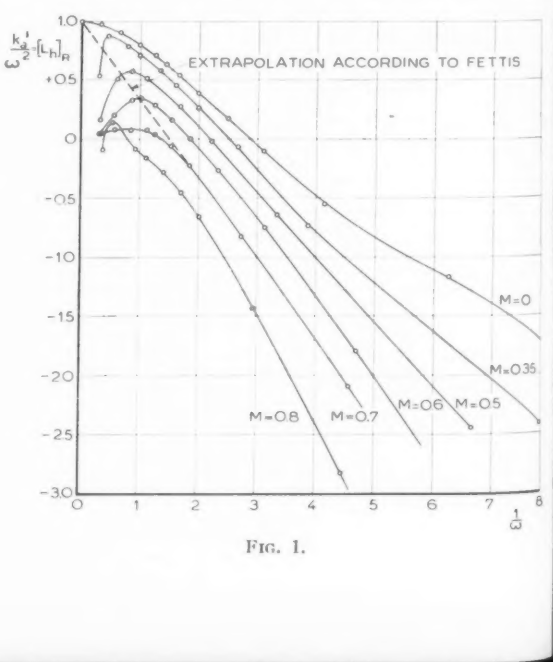

FIG. 1.

for different values of the Mach Number (Fig. 1) clearly show that $[L_h]_R \to 0$ if $\omega \to \infty$ and $M \neq 0$. The approach of the curves toward the origin is oscillatory, which is in accordance with reference 3. The curve for $M = 0.35$ closely follows the curve for $M = 0$ if the latter is supplemented by the $[L_h]_R$-axis between 1 and 0. For the larger values of M, the deviations from the incompressible case increase, and it is obvious that Fettis' extrapolation of Dietze's values is incorrect.

Thirdly, with regard to the identity $k_a = i\omega(m_a + k_b)$, our exact analytical expressions for the coefficients show that this relation holds only in incompressible flow. As Fettis' derivation of this "identity" for compressible flow is not yet available to us, no further comment can be given.

In conclusion, we cannot admit that any coincidence of errors in our calculations has been brought to light. We maintain our claim that the accuracy of our results amounts to a few units in the last digit supplied, a claim based on analytical checks for the limits of all errors committed.

References

[1] Fettis, H. E., *Comments on Aerodynamic Coefficients of an Oscillating Airfoil in Two-Dimensional Subsonic Flow*, Readers' Forum, Journal of the Aeronautical Sciences, Vol. 19, No. 5, pp. 353–354, May, 1952.

[2] Timman, R., van de Vooren, A. I., and Greidanus, J. H., *Aerodynamic Coefficients of an Oscillating Airfoil in Two-Dimensional Subsonic Flow*, Journal of the Aeronautical Sciences, Vol. 18, No. 12, pp. 797–802, December, 1951.

[3] Timman, R., *Approximate Theory of the Oscillating Wing in Compressible Subsonic Flow for High Frequencies*, Nat. Aero. Res. Inst. Report F.99, 1951.

[4] Miles, J. W., *On Virtual Mass and Transient Motion in Subsonic Compressible Flow*, Quart. Journ. Mech. and Appl. Math., Vol. 4, No. 4, pp. 388–400, December, 1951.

[5] Longhorn, A. L., *The Unsteady Subsonic Motion of a Sphere in a Compressible Inviscid Fluid*, Quart. Journ. Mech. and Appl. Math., Vol. 5, No. 1, pp. 64–81, March, 1952.

Gas-Turbine Power Plant for Aircraft

Ali Bülent Cambel

Assistant Professor of Mechanical Engineering, State University of Iowa, Iowa City

July 24, 1952

RECENT IMPROVEMENTS IN PROPELLER EFFICIENCIES once again bring to the foreground propeller-driven aircraft. At least theoretically, a power plant suggests itself which might be used to some advantage in such aircraft.

If one analyzes the performances of the various gas-turbine cycles as summarily shown in Figs. 1a and 1b, one notices that, for the same temperature limits, a regenerative cycle in which both the compression and the expansion take place isothermally has the highest thermal efficiency and that the efficiency of this plant is not affected by the pressure ratio. Further, one notices from Fig. 1b that the highest specific output parameter is achieved in a plant having isothermal compression and expansion. The analysis of this cycle indicates that, in the absence of losses, the need for the combustion chamber is obviated. Thus, the only external heat that must be supplied to the plant is that necessary to maintain isothermal expansion in the turbine.

Although the advantages of isothermal compression and expansion are evident, in practicality their achievement is difficult. One method that suggests itself is to bleed gas from the compressor and, after raising its temperature, introduce it into the turbine. Of course, the air entering the turbine will have to be carefully apportioned, but this should not pose undue difficulty. The bleeder gas may be heated suitably with an atomic reactor, which may also be used to preheat the throttle gases entering the turbine. A schematic layout of the power plant is shown in Fig. 2, in which the isothermal compression is accomplished by multistaging and intercooling. Because there is no need for combustion in the cycle, the use of air as the working medium is not necessary. A light gas, highly desirable because it would reduce the size of the plant, may therefore be used. In passing, it might be mentioned that, everything else remaining

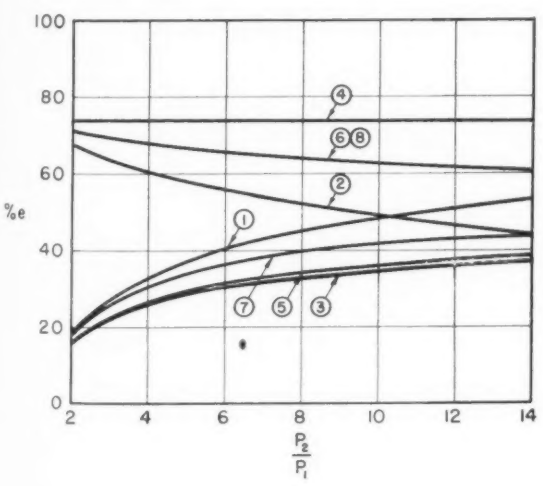

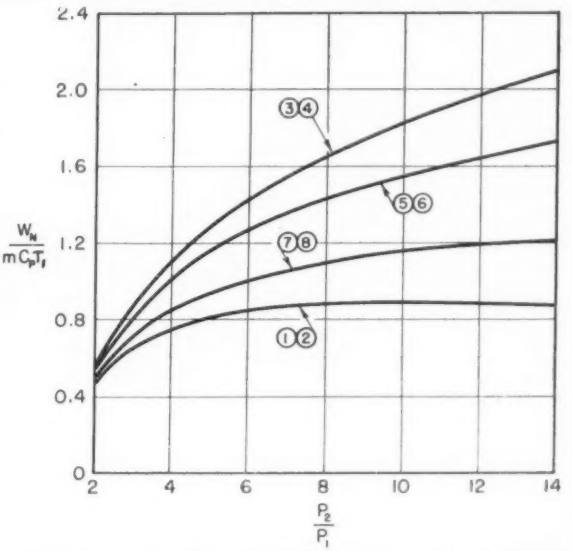

FIG. 1a (*left*). Efficiency curves of certain gas-turbine cycles. FIG. 1b (*right*). Specific output parameter curves of certain gas-turbine cycles. Combustor temperature, 1,500°F. No loss in available energy is considered. (1) adiabatic compression and adiabatic expansion; (3) isothermal compression and isothermal expansion; (5) adiabatic compression and isothermal expansion; (7) isothermal compression and adiabatic expansion; (2) adiabatic compression and adiabatic expansion with regeneration; (4) isothermal compression and isothermal expansion with regeneration; (6) adiabatic compression and isothermal expansion with regeneration; (8) isothermal compression and adiabatic expansion with regeneration.

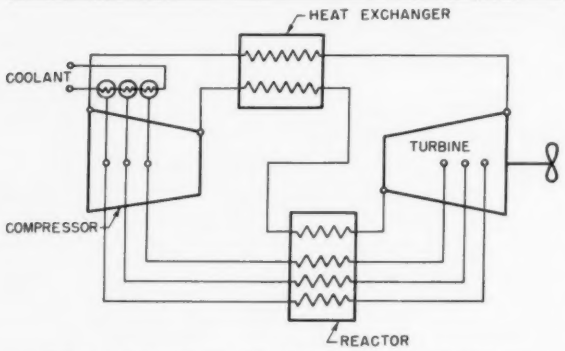

FIG. 2. Arrangement of reactor gas-turbine power plant.

the same, the characteristics of the gas do not affect the efficiency of the plant. Helium suggests itself as a reasonable possibility because it may be obtained conveniently and is safe. Besides being advantageous as far as the size of the plant is concerned, helium is also desirable because of its high thermal conductivity as compared to air. No complexity is expected with the design of the heat exchanger. In fact, it will be considerably smaller than the one that would have to be used with an open cycle. Probably the greatest difficulty will lie in the shielding arrangement. It is hoped that the geometry of the reactor shield will not offset the reduction in size of the plant which should be achieved by the thermodynamical choice of cycle and working medium. Because of the absence of combustion products, the life of the proposed plant may be longer. Finally, the plant will have fewer auxiliaries, which should make its control and maintenance more trouble-free and economical.

Proceedings

Third Anglo-American Aeronautical Conference

Now Available

Proceedings of the Joint Conference between The Royal Aeronautical Society and the Institute, held in Brighton September, 1951, are now ready for distribution in England. These volumes contain all of the full-length papers and discussions presented at the Conference. Only a limited supply is available for distribution.

Order Direct from

The Royal Aeronautical Society

4 Hamilton Place — London, W. 1, England

Send remittance with order:
£5.5.0 ($14.80), postage prepaid.

(10% U.S. Customs Duty
Payable upon Receipt.)